

**ADAPTED METHODOLOGY OF CHANGE DETECTION USING
REMOTELY SENSED DATA: REDUCING ERRORS DUE TO POINTING
DIRECTION SHIFTS OF A SATELLITE SENSOR**

DISSERTATION

Presented in Partial Fulfillment of the Requirement for

The Degree Doctor of Philosophy in the

Graduate School of The Kochi University of Technology

By

JEONG JONG HYEOK, B.E, M.E.

Kochi University of Technology

2005

Dissertation Committee:

A. Prof. Masataka TAKAGI

Prof. Fumiaki TAKEDA

Prof. Hiroshi SHIMA

Prof. Kazuo OUCHI

Prof. Nobumitsu FUJISAWA

Abstract

The remote sensing using satellites provides periodical homogeneous data which cover wide area, thus remotely sensed data have been used widely for land cover change detection. The change detection is one of the most important analyses for understanding the change phenomena of natural environments. Natural environments exist in continuous spaces. The continuous spaces are sampled by remote sensing sensors, and the sampled area can be changed by the pointing direction shift of remote sensing sensors. Currently change detections have been carried out under an assumption that the registered pixels of time series data on the same coordinates are covering the same locations. However the assumption is incorrect because the pointing direction shift of a satellite sensor in each observation is not considered.

For typical change detection using satellite images, an arithmetic comparison is carried out using the geometrically registered classification results of time series data. To improve accuracy of change detection, radiometric difference of time series data, the linear mixture analysis, registration accuracy and a comparison method were considered. Xiaojun et al. (2000) evaluated the performance relative radiometric normalization methods. Linear mixture analysis was developed to investigate landcover proportion in pixel. Settle and Drake (1993) found that all possible mixtures with non-negative proportions of the end members should be enclosed by a polyhedron. The accurate acquisition of control points is required for an accurate registration. Gruen (1985), Gruen and Baltsavias (1985) proposed the adaptive least squares correlation for obtaining highly accurate control points. The error in change detection by pointing direction shift can be reduced using an adapted comparison method. Gong et al. (1992) and Stow (1999) tried to reduce change detection errors due to misregistration. However the methods cannot reduce error due to pointing direction. An advanced resampling method should be developed to reduce the errors due to pointing direction shift of a satellite sensor. Image normalization, linear mixture analysis, registration and comparison method have been investigated independently. This study aimed to build an adapted methodology of change detection by combining the four elements. Especially, the advanced resampling method will perform highly accurate change detection.

The Visual Near Infra Red bands of ASTER (Advanced Spaceborne Thermal Emission and Reflection Radiometer) acquired in October 2001, January 2002, and March 2002 were used for a change detection using the proposed method. An IKONOS image which was geometrically corrected by three-dimensional Affine transformation was used as the reference data for establishing geometrical transformations and performing classification of the three ASTER scenes.

The linear stretch method was applied to the radiometric normalization of the ASTER images. The DN values of Maximum and minimum were used to make linear radiometrical transformations. The training pixels of the maximum and minimum were

taken from unchangeable pure bare soil areas and water areas respectively. The same locations of each ASTER image were selected to take the training pixels.

The land classification result by conventional method is not appropriate for the proposed resampling method because the classification result represent only major landcover in a pixel, there fore the classification result by the conventional method can not be resampled. In this study, the linear mixture analyses of the normalized ASTER images were carried out using same spectral unmixing equations. The proportion of bare soil, water, and vegetation were calculated.

Geometric transforms were required to plot pixel boundaries of the three ASTER images on a geometrically fixed grid. Accurate control points were necessary for obtaining transforms. Template images were taken from the IKONOS image, then the corresponding points on the three ASTER images were searched using the area based image matching method. Affine transforms were calculated using the control points. The accuracies of the Affine transforms showed less than three meters (0.2 pixel of the ASTER image) of root mean square error. The subpixel accuracy of the transforms could be obtained using the image templates from the IKONOS image.

A geometrically fixed grid was proposed to compare the same location of remotely sensed time series data. Pixel boundaries of the three ASTER images were plotted on the fixed grid. The cell values of the fixed grid were obtained using a resampling method using the proportional adjustment of pixels' existence ratio and landcover proportion in the grid cell. The proposed method was evaluated in a simulation. The proposed method and pixel by pixel comparison method were compared in the simulation. When a half of pixel shifted, the change detection error by pixel by pixel method was almost 50% higher than the proposed method. The proposed method made more accurate change detection than pixel by pixel comparison method.

A solution for reducing change detection errors due to pointing direction shift was proposed in this study. The adapted methodology will perform important role for producing an accurate change detection result.

ACKNOWLEDGEMENTS

I would like to express my sincere thanks to my supervisor A. prof. TAKAGI Masataka for giving me chance to continue doctoral course and inspiring me to reach the goal of the research. His family members must be appreciated for treating me with their warm heart and kindness.

I would also like to express my sincere thanks to professors of the landscape architecture department in Jin-Ju National University. They recommended for me to study at the Kochi University of Technology, and gave me valuable advices and encouragements.

Mrs. SEO Eun-Kyoung and Mr. HASIZUME have supported me from my master years; the memory of their kindness will not be erased until the end of my life.

I would like to thank my mother, father, younger brother, my wife and son for their encouragements and sacrifice.

Due to valuable advices from the committee and my colleagues, this thesis could be much improved.

Without scholarships form Jin-Ju National University, Kochi University of Technology, Rotary club and Monbushou (Japan Ministry of Education, Culture, Sports, Science and Technology), this thesis could not be existed.

TABLE OF CONTENTS

1. Introduction

1.1 General overview	1
1.2 Literature review and The research problems.....	2
1.3 Objectives	6
1.4 The thesis overview	6

2. Data description

2.1 Advanced Spaceborne Thermal Emission and Reflection Radiometer (ASTER)	8
2.1.1 Introduction	
2.1.2 ASTER Sensors	
2.1.3 ASTER Products	
2.1.4 HDF-EOS data	
2.1.5 ASTER Data used	
2.2 IKONOS	15
2.2.1 Introduction	
2.2.2 IKONOS-2 sensor and image specification	
2.2.3 IKONOS data product	
2.2.4 IKONOS data used	
2.3 Test area	17

3. Relative normalization of time series remotely sensed data

3.1 Linear contrast stretch	18
3.2 Histogram matching	19
3.3 Relative normalization of the ASTER images	19

4. Linear mixture analysis

4.1 Linear mixture analysis	29
-----------------------------------	----

4.2 Linear mixture analysis of the ASTER images	31
5. Establishing geometrical transforms using very high resolution satellite image	
5.1 Transforms	41
5.1.1 Herlmert Transformation	
5.1.2 Two-dimensional Affine transform	
5.1.3 Two-dimensional projective coordinate transform	
5.2 Affine Transform of the IKONOS	42
5.2.1 Establishing transforms using the geometrically corrected IKONOS image	
5.2.2 Digital Image matching to obtain highly accurate GCP	
5.2.3 Image matching between the IKONOS templates and ASTER images	
5.3 The results of the transformations.....	53
6. Change detection and classification	
6.1 A solution proposed for reducing change detection	56
6.1.1 Resampling linear mixture analysis results of the ASTER images using geometrically fixed grids	
6.1.2 Simulation using the classification result of an IKONOS image	
1) Change detection using pixel by pixel comparison method	
2) Change detection using the proposed method	
6.2 Case study using the ASTER images acquired in October 2001 and January 2002	62
6.2.1 Change detection using ASTER images acquired in October 2001 and January 2002 using the two change detection methods	
6.3 Landcover classification using the classification results of time series remotely sensed data	70

7. Conclusions and discussions

7.1 Resampling method using geometrically fixed grid was developed to reduce the errors in change detection due to the pointing direction shift of remotely sensed time series data.....	85
7.2 Resampling method using geometrically fixed grid was developed to reduce the errors in change detection due to the pointing direction shift of remotely sensed time series data.....	85
7.3 The adapted methodology of change detection was established.....	86
7.4 Future works.....	86

LIST OF FIGURES

1.1 Remote sensing processes.....	1
1.2 Change detection process and research problems considered in this study.....	2
1.3 It is difficult to find highly accurate control points of high resolution satellite image such like ASTER.....	3
1.4 Two pointing direction different remotely sensed data are overlaid on an IKONOS image. The comparison of incompletely overlaid pixels may cause change detection errors	4
1.5 (a) shows misregistration, (b) shows pointing direction shift.....	6
2.1 Data structure of Level-1A.....	10
2.2 Data structure of Level-1B.....	11
2.3 The October scene.....	12
2.4 The January scene.....	13
2.5 The March scene.....	14
2.6 The test area.....	17
3.1 Conceptual process of the linear contrast stretch.....	19
3.2 Histogram matching process, (a) the histogram of source image, (b) the histogram of reference image (c) histogram matching (d) the result of histogram matching (Richard, Jia, 1998).....	20
3.3 Building normalization equations for three seasonal images with the same outputs	21

3.4 The input of minimum and maximum values were taken from dark pure water and pure bare soil areas.....	21
3.5 The histogram of VNIR bands for the October scene	23
3.6 The histogram of VNIR bands for the January scene.....	24
3.7 The histogram of VNIR bands for the March scene.....	24
3.8 The normalization result of October scene's band1, (a) before normalization, (b) after normalization.....	25
3.9 The normalization result of January scene's band1, (a) before normalization, (b) after normalization.....	25
3.10 The normalization result of March scene's band1, (a) before normalization, (b) after normalization.....	25
3.11 The normalization result of October scene's band2, (a) before normalization, (b) after normalization.....	26
3.12 The normalization result of January scene's band2, (a) before normalization, (b) after normalization.....	26
3.13 The normalization result of March scene's band2, (a) before normalization, (b) after normalization	27
3.14 The normalization result of October scene's band3, (a) before normalization, (b) after normalization	27
3.15 The normalization result of January scene's band3, (a) before normalization, (b) after normalization	28
3.16 The normalization result of March scene's band3, (a) before normalization, (b) after normalization	28

4.1	The locations where the training data were collected.....	32
4.2	(a) The ASTER scene acquired in October 2001, (b) The scatter plot between band2 and band3.....	35
4.3	(a) The ASTER scene acquired in January 2002 , (b) The scatter plot between band2 and band3.....	36
4.4	(a) The ASTER scene acquired in March 2002, (b) The scatter plot between band2 and band3.....	37
4.5	The result of linear mixture analysis of October scene.....	38
4.6	The result of linear mixture analysis of the January scene.....	39
4.7	The result of linear mixture analysis of March scene.....	40
5.1	The direct transformation and inverse transformation.....	43
5.2	(a) The IKONOS image (b) The ASTER image acquired in October 2001.....	43
5.3	Area based template matching.....	44
5.4	Finding corresponding location of a template using correlation.....	45
5.5	GCP 1 for the registration of the October scene.....	46
5.6	GCP 2 for the registration of the October scene.....	46
5.7	GCP 3 for the registration of the October scene.....	47
5.8	GCP 4 for the registration of the October scene.....	47
5.9	GCP 5 for the registration of the October scene.....	48

5.10 GCP 6 for the registration of the October scene.....	48
5.11 GCP 1 for the registration of the January scene.....	49
5.12 GCP 2 for the registration of the January scene.....	49
5.13 GCP 3 for the registration of the January scene.....	50
5.14 GCP 4 for the registration of the January scene.....	50
5.15 GCP 1 for the registration of the March scene.....	51
5.16 GCP 2 for the registration of the March scene.....	51
5.17 GCP 3 for the registration of the March scene.....	52
5.18 GCP 4 for the registration of the March scene.....	52
5.19 GCP 5 for the registration of the March scene.....	53
5.20 The result of direct transform between the IKONOS and the October scene....	54
5.21 The result of direct transform between the IKONOS and the January scene....	55
5.22 The result of direct transform between the IKONOS and the March scene.....	55
6.1 A fixed grid overlaid on a classification result of an ASTER scene, existence ratio of each pixel included in the zoomed cell was calculated.....	57
6.2 The simulation flow.....	58
6.3 Classification of the test area for the simulation by visual interpretation.....	59
6.4 Simulated pointing direction shifted data.....	59
6.5 Example of Landcover attribute assignments process.....	60

6.6 Change detection by comparing zero meter shifted data and one meter to seven meter shifted data.....	60
6.7 Fixed grids for the pointing direction shifted data.....	61
6.8 Change detection by comparing zero meters shifted data and one meter to seven meters shifted data.....	61
6.9 Comparison between change detection errors generated by the fixed grid and by the pixel by pixel comparison.....	62
6.10 Rectified ASTER scene acquired in October 2001.....	64
6.11 Rectified ASTER scene acquired in January 2002.....	65
6.12 Change detection between ASTER scene acquired in October 2001(a) and the rectified ASTER scene acquired in January 2002 (b) using the pixel by pixel comparison: the boxed areas in the two images were compared.	67
6.13 Change detection between ASTER scene acquired in October 2001(a) and the ASTER scene acquired in January 2002(b) using the proposed method: the fixed grids in the two images were compared.	68
6.14 The histogram of degrees of change by the two change detection methods.....	69
6.15 (a) the change detection result by pixel by pixel comparison, (b) the change detection result by the proposed method, (c) the IKONOS image.....	69
6.16 Test area of the October scene for the change detection.....	72
6.17 Test area of the January scene for the change detection.....	73
6.18 Test area of the March scene for the change detection.....	74

6.19 Dark urban and water field in the October scene was separated from water class	75
6.20 Dark urban and water field in the January scene was separated from water class	76
6.21 Dark urban and water field in the March scene was separated from water class	77
6.22 Water field in the classification result of the October scene could be separated from dark urban.....	78
6.23 Water field in the classification result of the January scene could be separated from dark urban.....	79
6.24 Water field in the classification result of the March scene could be separated from dark urban.....	80
6.25 The final stage of the classification using 68 phenological rules.....	81

LIST OF TABLES

2.1 Characteristics of the Three ASTER Sensor Systems.....	9
2.2 The sun's aspect and azimuth angle of the ASTER images.....	15
2.3 The characteristics of the IKONOS Sensor Systems.....	15
2.4 IKONOS data products.....	16
3.1 The minimum inputs of each ASTER scene	22
3.2 The maximum inputs of each ASTER scene.....	22
3.3 The outputs of the minimum and maximum inputs for the ASTER images	22
3.4 The gains and offsets of the normalization equations for the October ASTER scene	22
3.5 The gains and offsets of the normalization equations for the January ASTER scene	23
3.6 The gains and offsets of the normalization equations for the March ASTER scene	23
4.1 Spectral signature of each endmember.....	32
4.2 Spectral unmixing tolerance (average, square metres).....	32
5.1 Maximum error of the three transforms.....	54
5.2 RMS error of the three transforms.....	54
6.1 The degrees of change by the two change detection methods.....	66

6.2 The result of linear mixture analysis classified into seven classes.....70

6.3 68 phenological rules for the final landcover classification.....82

Chapter 1

INTRODUCTION

1.1 General overview

Remote sensing is the science that acquires information about objects or phenomena without physical contact with them (Lillesand, 2002). A typical remote sensing process (Jensen, 1996) is shown in figure 1.1. Users such like a scientist, government and company state problems relate to objects or phenomena. Data acquisitions are performed according to their demands using passive or active sensors which are mounted on an airborne or spaceborne craft. The objects or phenomena exist in continuous spaces. The continuous spaces are sampled by a remote sensing sensor, and stored in a pixel-based data. the pixel based data are registered on a coordinate system using a resampling method for the convenience of data analyses, processing and interpretation. The data are processed and analyzed to obtain information. Finally the extracted information are distributed to the users.

Change detection is one of most important analyses for solving problems relate to change phenomena. Remotely sensed data is widely used for change detection because periodical consistent data which cover wide areas are available. When a change detection is performed using registered remotely sensed time series data, the remote sensor system and environmental system should be considered carefully (Jenson, 1996). Poor understanding of the various parameters on the change detection process can lead inaccurate change detection results (Dobson, 1995).

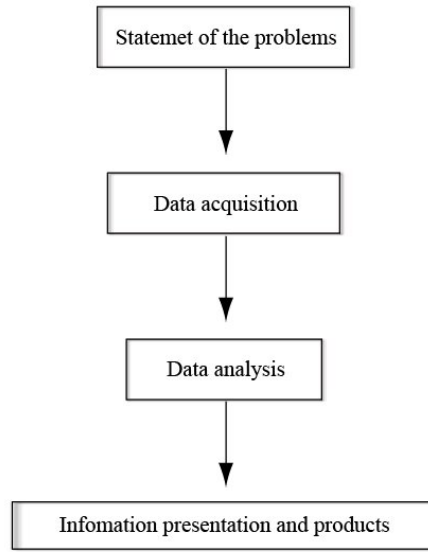


Figure 1.1: Remote sensing processes

1.2 Literature review and research problems

Figure 1.2 shows conventional change detection process and research problems considered in this study. In the process of data acquisition for change detection, time series data is required, and the radiometrical normalization of them should be carried out because the changes of atmospheric condition of the time series data can be greater than landcover changes. The geometrical transforms of the time series data are carried to be compared; the accuracy of change detection are much depend on the accuracy of the geometrical transforms. The affect of pointing direction shift of remotely sensed time series data on change detection is rarely investigated, the shift of pointing direction of the time series data may cause the errors in change detection because the pixels of timeseries data can cover slightly different areas. Therefore studies about radiometric image normalization, linear mixture analysis, image matching to build higly accurate transform and comparison methods were reviewed.

A large number of remotely sensed time series data may be used for change detection. The data can be influenced by many factors such as the sun angle and atmospheric condition. In order to detect the change of landcover without the influences, radiometric difference of the data should be reduced. Gong et al. (1992) proposed a method to reduce the change detection errors due to misregistration, however he did not perform the radiometrical normalization of the time series data in the study. Xiaojun et al. (2000) evaluated the performance of the five relative radiometric normalization methods: pseudo invariant features, radiometric control set, image regression, no-change set determined from scatter diagrams, and histogram matching. Linear regression showed best performance. E.A. McGovern et al. (2002) claimed that every radio-

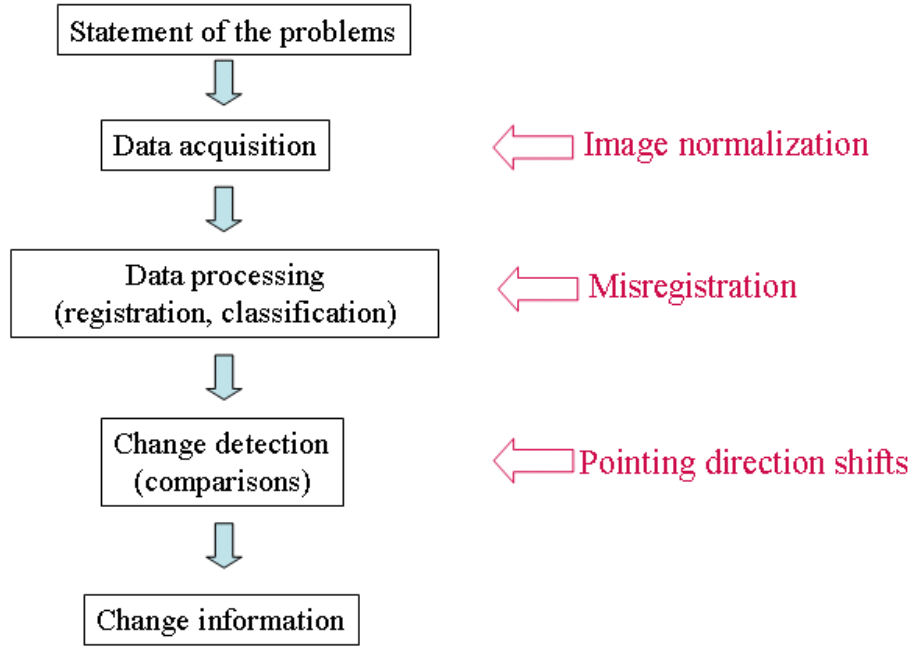


Figure 1.2: Change detection process and research problems considered in this study

metric normalization task must be considered separately and appropriate solutions devise, and single approach of image normalization can not be the universal application because solutions depend on location, application and the types of satellite images. The affects of radiometrical normalization to landcover classification and change detection are rarely investigated.

Linear mixture analysis is a decomposition method to investigate landcover proportion within a pixel. Settle and Drake (1993) found that all possible mixtures with non-negative proportions of the endmembers (pure information class) should be enclosed by a polyhedron. A polyhedron is shaped by connecting the positions of endmembers in a hyperspace. During decomposition process in the linear mixture analysis, negative fractions of landcovers are obtained. Gross and Schott (1998) described that negative fraction can be generated due to poor endmember selection, including an improper number of endmembers, or because of spectral ambiguity. Shimabukuro and Smith (1991) proposed least square mixing models to generate fraction images derived from remote sensing multispectral data. The least square method and the weighted least square method examined to derive the proportion of each endmember from spectral unmixing equations. The weighted least square method was superior to the least square method. Stefaine et al. (1997) considered the situation when pure endmember is not exiting in a hyperspectral image; they proposed "virtual endmember" to represent inexistent endmember.

For highly accurate change detection using time series remotely sensed data, registrations of them in subpixel level are required, however it is difficult to achieve the registration of images in subpixel level by using GCP obtained by visual interpretation. Figure 1.3 depicts the difficulty

in finding corresponding points between the IKONOS image and the ASTER image. Image matching is one of the most important techniques to find control points of two or more images in photogrammetry. Helava (1978) started the research about image correlation. Gruen (1985), Gruen and Baltsavias (1985) proposed the adaptive least squares correlation which based on the combination of area and edge based matching. The method can be applied to the matching problems of various image data. Gong et al. (1992), Townshend et al. (1992) and Stow (1999) might use control points obtained by visual interpretation, however that is not systematic and practical when many data are used for landcover change detection.

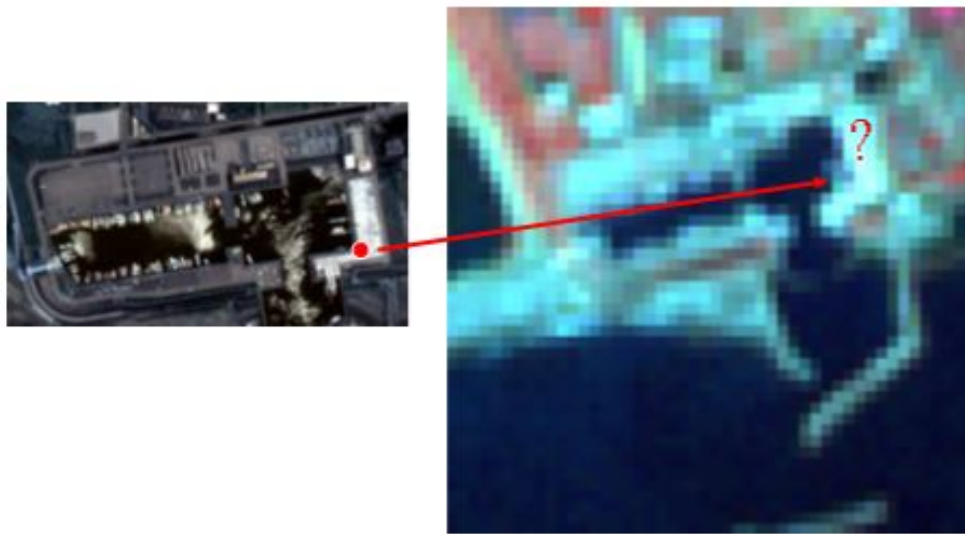


Figure 1.3: It is difficult to find highly accurate control points on a high resolution satellite image such like ASTER.

The geometrical transformations of remotely sensed time series data are performed for change detection. Geometrical distortions exist in the result of the registrations. Following researchers proposed methods to reduce the distortions; Gong et al. (1992) tried to reduce change detection errors due to misregistration; the band 3 of two Landsat TM satellite images were filtered using median and adapted gray-level filters, and then the filtered images subtracted from the other. The median filter ruined the change detection result. The adapted filtering was a reliable for reduction of registration noise. Townshend et al. (1992) used MODIS images with 250m and 500m spatial resolution. The two NDVI of the two images were generated, and then misregistrations of them were simulated by moving them in 45 degree on densely and sparsely vegetated area. The simulation result showed that misregistration can affect the ability of remotely sensed data to detect changes in land cover. In the result of the simulation, the effect of misregistration in 250m resolution data was higher than that of misregistration in 500m resolution data. More misregistration errors were generated on densely vegetated area than that on sparsely vegetated area. Stow (1999) proposed a miregistration compensation model for reducing misregisration effects on change detection results; two landsat TM3 bands were used.

The misregistration carried out by moving an image from -4.0 to 0.0 pixels in both x and y immersions. His model showed promising for enhancing land features and reducing noises by misregistration.

Although highly accurate registrations of remotely sensed time series data are performed using a resampling method, the resampled pixels of the data are not covering geometrically same areas; before resampling, the source data may cover slightly different areas due to pointing direction shift of a remote sensing sensor. When pixel by pixel comparisons in change detection are carried out using the registered data, the incompletely overlaid areas of time series data are compared. Figure 1.4 shows plotted pixel boundary of two seasonal data without geometrical resampling, pixels of the two scenes are covering slightly different area. This may cause one of change detection errors. The pointing direction shifts of remotely sensed time series data can lead incorrect change detections. Gong (1992), Townsahend (1992), and Stow (1999) considered the change detection errors due to 'misregistration'; another source of change detection error due to pointing direction shift of remotely sensed time series data was considered in this study. Figure 1.5 shows the differences between misregistration and pointing direction shift: misregistration can be occurred by the distortion of a geometrical transformation and resampling method which often expressed in Root Mean Square Errors (RMSE), while the pointing direction shifts are caused by the sampling area shift by a satellite sensor.

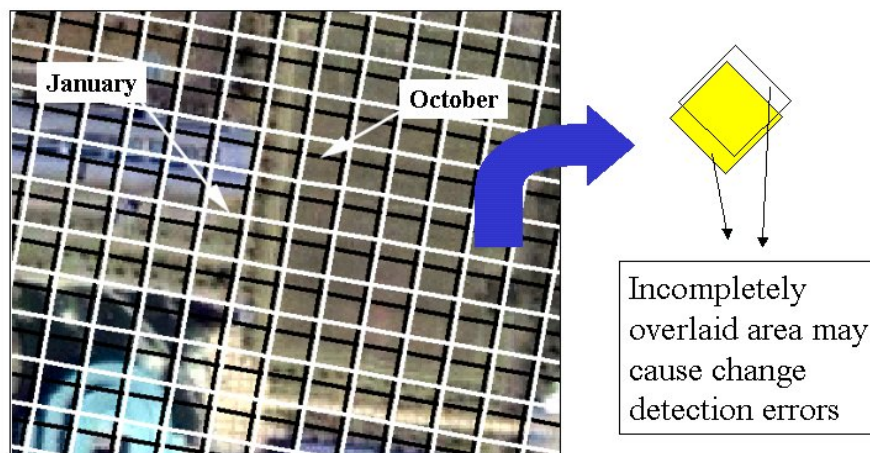


Figure 1.4: Two pointing direction different remotely sensed data are overlaid on an IKONOS image. The comparison of pixels covering slightly different areas may cause change detection errors.

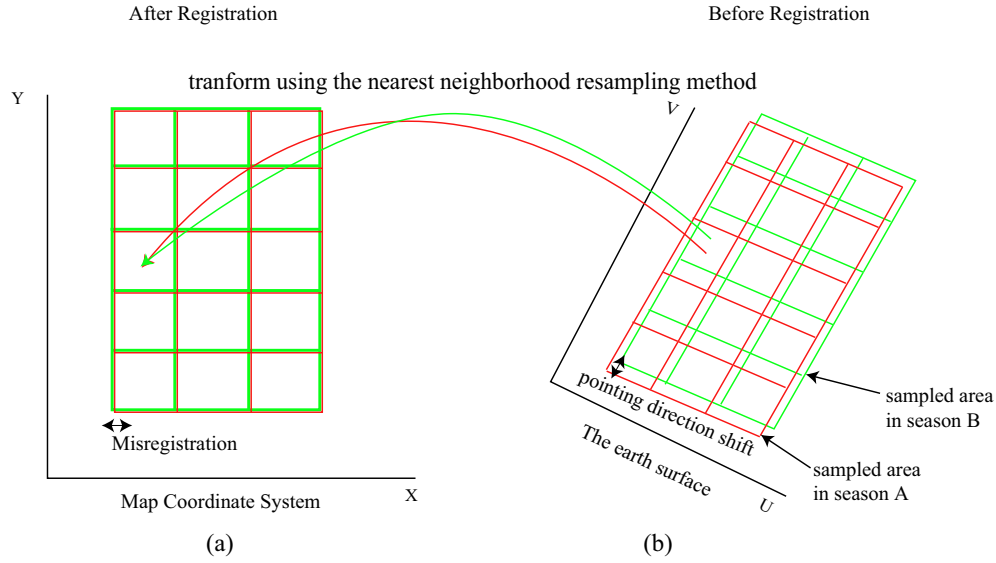


Figure 1.5: (a) shows misregistration, (b) shows pointing direction shift.

Gong (1992) and Stow (1999) used Image Algebra Change Detection method (Band Differencing), thus they considered only that the target area is changed or not; this study however considered the change of landcover proportions, and a method was proposed to reduce the pointing direction shift error when landcover proportions in pixels are compared.

1.3 Objectives

Based on the research problems, following objectives are established:

1. Developing a method for reducing the errors in change detection due to pointing direction shifts of remotely sensed time series data.
2. Building an adapted methodology of change detection by combining image normalization, linear mixture model, accurate transformation and the proposed method.

1.4 The thesis overview

Chapter 2 explains data used in this study. The Visual Near Infra Red bands (VNIR) of the ASTER acquired in October 2001, January 2002, and March 2002 were used for a change detection using the proposed method. An IKONOS image which was geometrically corrected by the three-dimensional Affine transformation was used for establishing geometrical transformations and performing classification of the ASTER images.

Chapter 3 describes the relative image normalization of remotely sensed time series data. The linear stretch method was applied to the ASTER images for their radiometric normalization. The DN values of maximum and minimum were used to make a radiometrical linear transformation. The training pixels of maximum and minimum were taken from unchangeable pure bare soil area and water areas. The same location of each ASTER image was selected to take the training pixels. Two representative image normalization methods were compared; linear contrast stretch method was used for reducing the influence of radiometric differences of the three ASTER images.

Chapter 4 describes linear mixture analysis. The land use classification result by conventional method was not appropriate for the proposed landcover resampling method because the landcover proportions are required to perform the proposed method. In this study, the linear mixture analyses of the normalized ASTER images were performed using the same spectral unmixing equations. The proportion of bare soil, water, and vegetation were calculated.

A method for building accurate image transformation using the IKONOS image are introduced in the chapter 5. Three transformations were established to convert the ASTER images' coordinate system into the IKONOS image's coordinate system. The control points for the transformations were obtained by using area based image matching method: template images were taken from the IKONOS image, then the corresponding points on the three ASTER images were searched. The transformation error of each ASTER image was less than three meters (0.2 pixel of the ASTER image).

Chapter 6 describes the proposed method for reducing the errors in change detection due to pointing direction shift of remotely sensed time series data. A geometrically fixed grid was proposed to compare the same locations of remotely sensed time series data. Pixel boundaries of the ASTER images were plotted on the geometrically fixed grid. The cell values of the grid were obtained using a resampling method by proportional adjustment of pixels' existence ratio and landcover proportion in the grid cells, then the resampled grid values of each scene are compared other scenes'. The proposed method was evaluated in a simulation; the pointing direction shifted data were simulated, then the change detection of them carried out using the proposed method and pixel by pixel comparison method. The proposed method result more accurate change detection. For change detection, linear mixture analyses of the three ASTER images were carried out. The landuse classification was carried out using the change detection results and the linear mixture results of the ASTER images. Bare soil area, forest, water, water field including water side area, agricultural field, and dark urban area could be classified.

Chapter 7 describes conclusions and discussions of this study.

Chapter 2

DATA DESCRIPTION

Two kinds of satellite images were used in this study to develop a methodology of accurate change detection: three ASTER images and an IKONOS image. The cost of ASTER data is quite cheaper than IKONOS data, and the ASTER data can be easily obtained through the web interface provided by EARS DAC and NASA. Although the IKONOS data are expensive, they provide spatially detail information.

2.1 Advanced Spaceborne Thermal Emission and Reflection Radiometer (ASTER)

2.1.1 Introduction

The ASTER was developed through a cooperative project between NASA and Japan's Ministry of Economy Trade and Industry (METI). In December 1999, ASTER was launched on board NASA's Terra spacecraft which is a series of multi-instrument spacecraft forming Earth Observation System (EOS). Besides ASTER, the Moderate-resolution Imaging Spectrometere (MODIS), Multi-angle Imaging Spectro-Radiometer (MISR), Clouds and the Earth's Radiant Energy System (CERES), and Measurements of Pollution in the Troposphere (MOPITT) were installed in the Terra spacecraft. The orbit system of Terra is sun-synchronous with equatorial crossing at 10:30 am local time, and revisit time is every 96 days. All ASTER products are provided in Hierarchical Data Format (HDF-EOS).

2.1.2 ASTER sensors

The ASTER consists of three sensors (Table 2.1): the Visible and Near-infrared (VNIR) which has three bands with 15m spatial resolution including backward telescope for stereo, the Shortwave Infrared (SWIR) which has six bands with 30m spatial resolution, and the Thermal Infrared (TIR) which has five bands with 90m spatial resolution, each system

was developed by a different Japanese company.

2.1.3 ASTER products

The ASTER sensors produce two levels of data: Level-1A (L1A) and Level-1B (L1B). L1A data are reconstructed and unprocessed instrument data from Level-0 (raw) data, and it contains raw data and coefficients for geometric correction and radiometric correction. The coefficients are not applied in the L1A data. L1B data are L1A data with the radiometric and geometric coefficients applied; and cubic-convolution resampling was performed in the geometric correction.

Table 2.1: Characteristics of the three ASTER sensor systems (copyright on NASA JPL)

Subsystem	Band No	Spectral Range (μm)	Spatial Resolution	Quantization Levels
VNIR (3 Nadir, 1 Backward)	1	0.52-0.60	15m	8 bit
	2	0.63-0.69		
	3N	0.78-0.86		
	3B	0.78-0.86		
SWIR	4	1.60-1.70	30m	8 bit
	5	2.14-2.18		
	6	2.18-2.22		
	7	2.23-2.28		
	8	2.29-2.36		
	9	2.36-2.43		
TIR	10	8.12-8.47	90m	12 bit
	11	8.47-8.82		
	12	8.92-9.27		
	13	10.25-10.95		
	14	10.95-11.65		

2.1.4 HDF-EOS data

HDF was invented by National Center for Supercomputing Application (NCSA). HDF was adapted by NASA as a standard data format for storing data from the Earth Observation System, and was named HDF-EOS, thus all ASTER data are provided in HDF-EOS. Figure 2.1 and 2.2 show the data structure of level-1A and level-1B. The data structure of HDF-EOS is similar to a computer directory file system, both raw type data and parameter data are included in a HDF-EOS file.

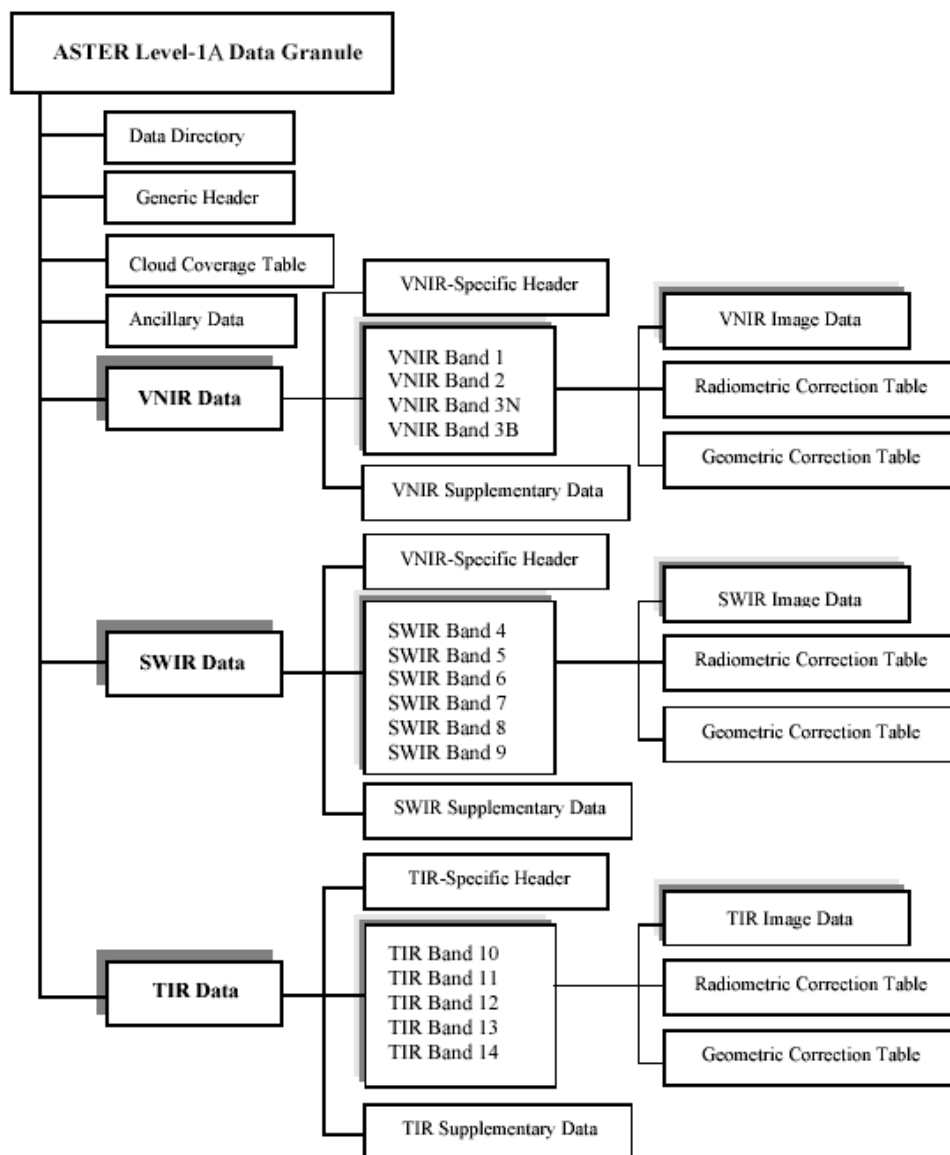


Figure 2.1: Data structure of Level-1A (copyrights on NASA JPL)

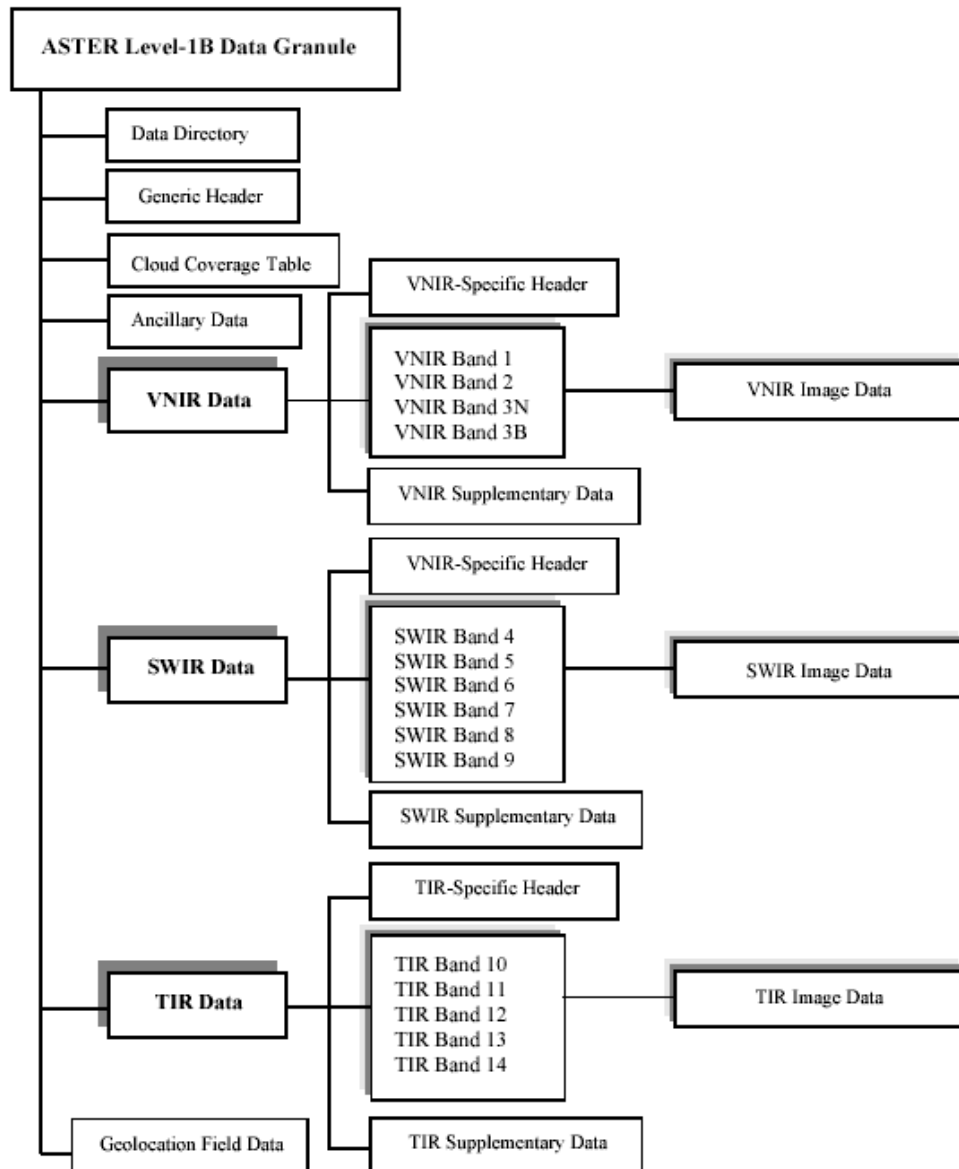


Figure 2.2: Data structure of Level-1B (copyrights on NASA JPL)

2.1.5 ASTER Data used

In this study, VNIR scenes of ASTER acquired in October 2001, January 2002, and March 2002 were used. Figure 2.3, 2.4 and 2.5 show the false composite (R: band3, G: band2, B: band1) of the ASTER images, the vegetation areas show red color due to the false composite. The coordinate system of the ASTER scenes is UTM53, and their datum is WGS84. The sun aspect angle and azimuth angle of the three ASTER scenes are shown in table 2.2.



Figure 2.3: The October scene

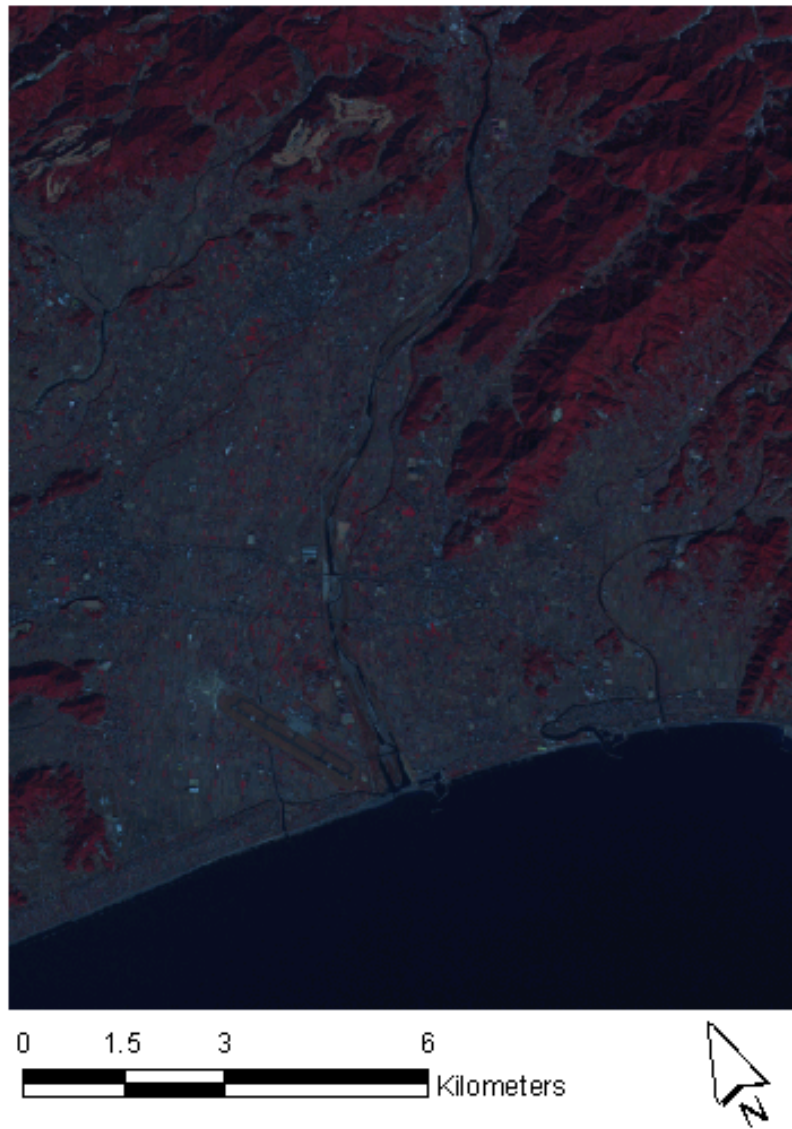


Figure 2.4: The January scene

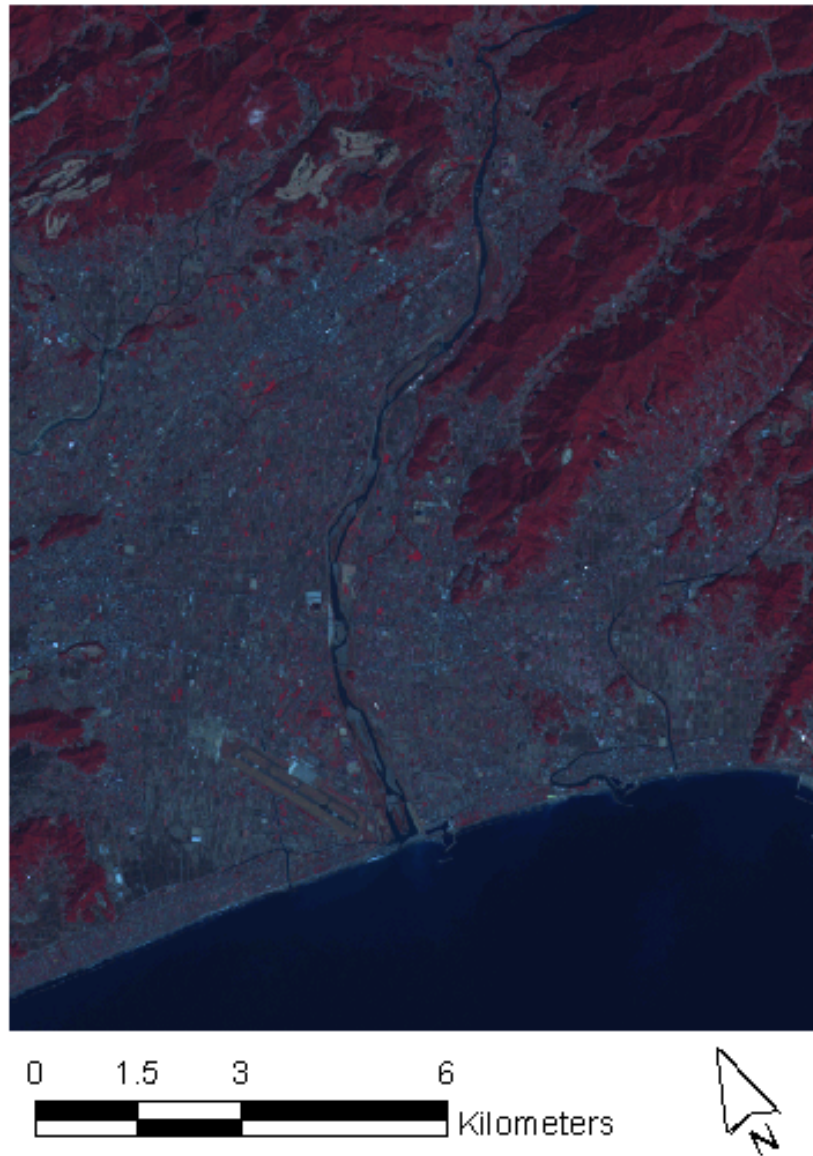


Figure 2.5: The March scene

Table 2.2: The sun's aspect and azimuth angle of the ASTER images

Date of acquisition	Aspect angle of the sun (degree)	Azimuth angle of the sun (degree)
10.31.2001	163.22	40.55
1.03.2002	160.25	30.53
3.08.2002	149.14	46.56

2.2 IKONOS

2.2.1 Introduction

IKONOS is the first commercial satellite which can produce 1m resolution satellite images. The IKONOS was launched in September 1999, its orbit system is sun-synchronous.

2.2.2 IKONOS-2 sensor and image specification

Table 2.3 shows the characteristics of the IKONOS sensor system. IKONOS sensor system produces panchromatic data with 1m resolution and hyperspectral data with 1m and 4m resolution. The one meter resolution hyperspectral data are produced by combining the panchromatic band and hyperspectral band using pan-sharpening process.

Table 2.3: The characteristics of the IKONOS Sensor Systems (copyrights on Space imaging).

System	Band	Spectral range	Spatial Resolution	Quantization Levels
Black-and-White	Panchromatic	0.45-0.90	1-meter	11bits
Multispectral	Band 1 (blue)	0.45-0.52	1meter or 4-meter color	11bits
	Band 2 (green)	0.51-0.60		
	Band 3 (red)	0.63-0.70		
	Band 4 (near infrared)	0.76-0.85		

2.2.3 IKONOS data product

Table 2.4 shows the products of the IKONOS image classified by positional accuracy. A GEO product of an IKONOS image was used in this study.

Table 2.4: IKONOS data products (copyrights on Space imaging).

Product	Positional accuracy		Ortho corrected	Stereo option
	CE90	RMS		
GEO	15.0m	N/A	No	No
Standard Ortho	50.0m	25m	Yes	no
Reference	24.5m	11.8m	Yes	yes
Pro	10.2m	4.8m	Yes	no
Precision	4.1m	1.9m	Yes	yes
Precision Plus	2.0m	0.9m	Yes	no

2.2.4 IKONOS data used

A pan-sharpened 1m resolution IKONOS data with 4 spectral bands was used in this study. The geometric correction of the IKONOS data was carried out using three dimensional Affine transformation (KADOTA, 2002), because the swath width (11.3 km) is narrow enough to be applied the Affine transformation. This data was acquired in Jun 2000. The sun's azimuth angle was 114.7 degrees, and elevation angle was 69.3 degrees.

1) Geo-metric correction of IKONOS image using three dimensional affine transformation

This data was registered by KADOTA (2002) who was a master student of the Kochi University of Technology, and was submitted as a result of her master research. This IKONOS image was geometrically corrected using the three dimensional Affine transformation. Equation 2.1 shows the three-dimensional affine transformation. Eight ground control points were used to calculate parameter of the equation. The RMS errors of the geo-metric correction were less than 1m (KADOTA, 2002).

$$\begin{aligned} u &= a_1x + a_2y + a_3z + a_4 \\ v &= b_1x + b_2y + b_3z + b_4 \end{aligned} \tag{2.1}$$

where u and v is image coordinate system; x,y,z is map coordinate system.

2.3 Test area

Nankoku and Tosayamada town in Shikoku island, Japan were selected as the test area. Figure 2.6 shows the IKONOS data used and the test area.

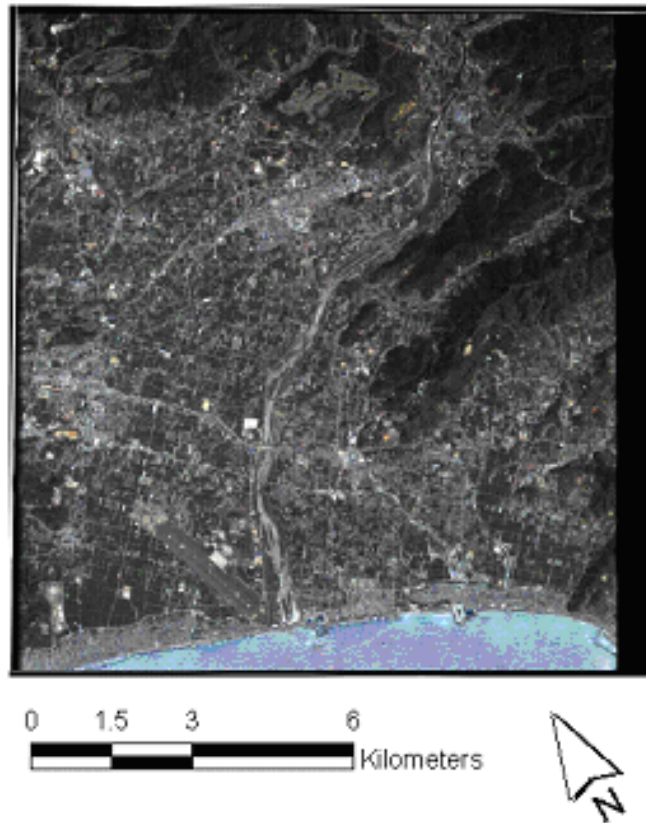


Figure 2.6: The test area

Chapter 3

RELATIVE NORMALIZATION OF REMOTELY SENSED TIME SERIES DATA

Spectral data obtained by satellite sensors can be affected by some factors such as illuminations of objects on earth surface and atmospheric condition (Teillet, 1986). The main target of relative normalization of multi-temporal data is reducing radiometric differences. If the radiometric differences of time series data can be reduced, the data can be processed under the same conditions. In this study two approaches were considered: linear contrast stretch and histogram contrast matching. The linear contrast stretch was adapted for the normalization of the ASTER images.

3.1 Linear contrast stretch

Linear contrast stretch is used to improve the visibility of images using a linear transformation. Figure 3.1 shows the conceptual process of the linear stretch: the minimum and maximum values in a target image are selected, and then the linear transformation that represents the relationship between the input (minimum and maximum) and corresponding output can be established. Finally the source image can be converted using the transformation.

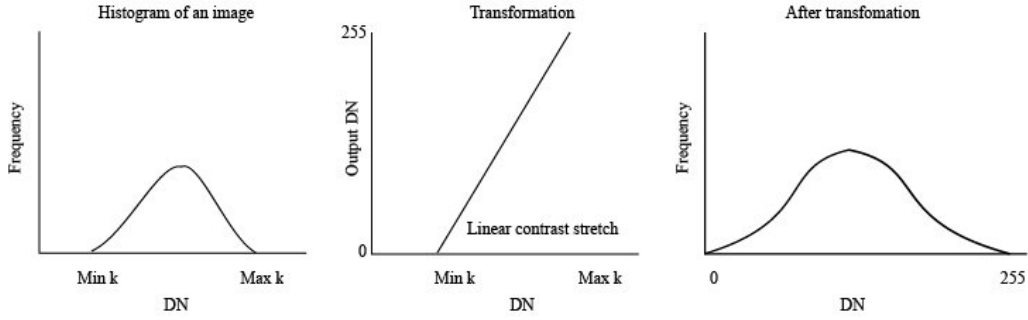


Figure 3.1: Conceptual process of the linear contrast stretch

3.2 Histogram matching

The cumulated histograms of a source image and a reference image are compared to make their contrast as much close as each other, thus this method has been used when a pair of continuous images are connected to form a mosaic image. Figure 3.2 depicts an example of histogram matching process: the cumulated histogram of a source image and reference image are prepared. Each level of digital number (DN) in the cumulated histogram of the source image matches the corresponding number of pixel in the cumulated histogram of the reference image; in case, corresponding DN is not in the available range, the nearest DN can be taken; the DN 6 in the cumulated histogram of the source image match the DN values between 1 and 2, in that case the nearest value DN 2 can be taken as the corresponding value. Figure 3.2-c shows the result of the histogram matching: DN 5, 6, 7, 8, 9 and 10 in the source image change to 1, 2, 3, 4 and 5 respectively.

3.3 Relative normalization of the ASTER images

The Linear contrast stretch method was used for the normalization of the ASTER images. There is a reason for using the method: the radiometric normalization in this study aimed to reduce the radiometric difference of time series data according to landcover types, an operator can make a transformation using manually decided inputs and outputs, however the output of normalization cannot be set manually in the histogram matching because the output values are decided by the cumulated histogram of a reference image as shown in the figure 3.2-c.

The equations for the normalization of each ASTER image could be obtained by using the same output values, which were decided by the author, figure 3.3 shows an example: the linear transformations of the three seasonal images can be obtained using the same

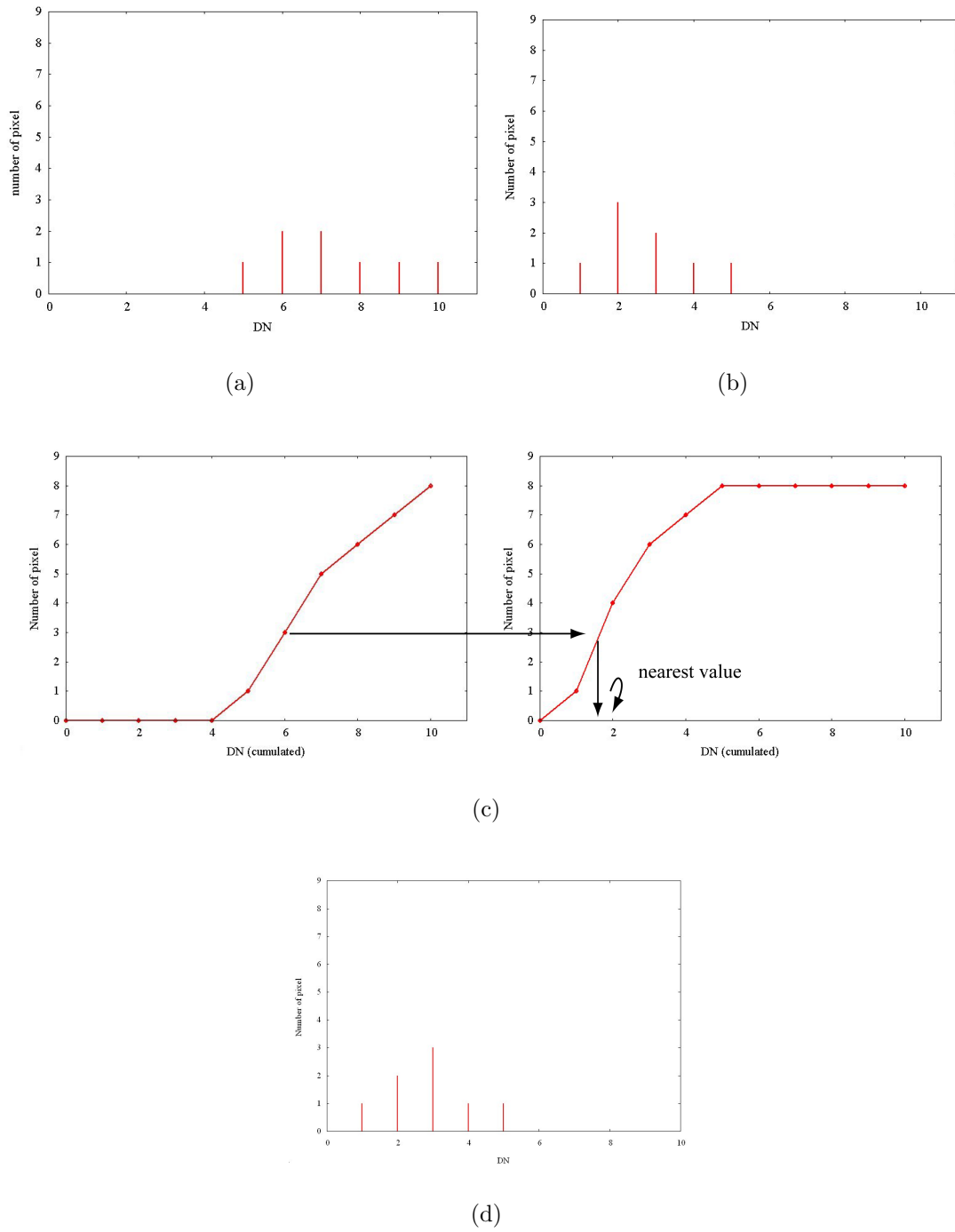


Figure 3.2: Histogram matching process, (a) The histogram of source image, (b) The histogram of reference image, (c) Histogram matching, (d) The result of histogram matching (Richard, Jia, 1998)

outputs.

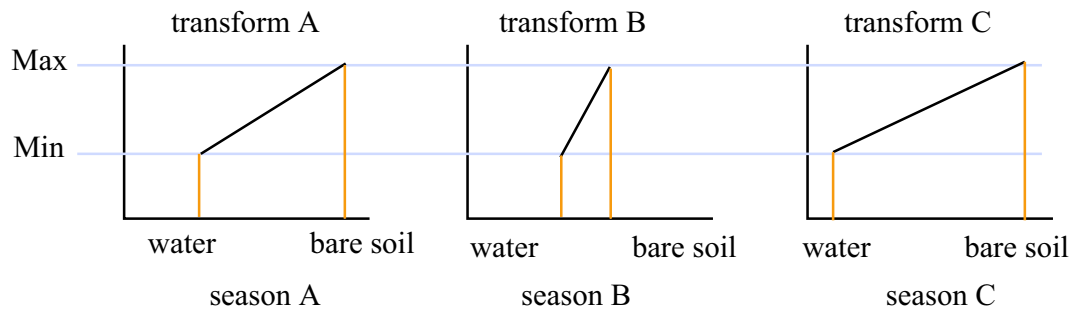


Figure 3.3: Building normalization equations for three seasonal images with the same outputs

For the radiometrical normalization of the ASTER images, the DN's of minimums and maximums were taken from the each band of the ASTER images. The ten pixels of minimums and maximums for each band of each scene were taken from unchangeable dark pure sea and bright bare soil area respectively (figure 3.4). The averages of them were used for the input minimum and maximum. Table 3.1 and 3.2 show each ASTER scene's minimum and maximum inputs.

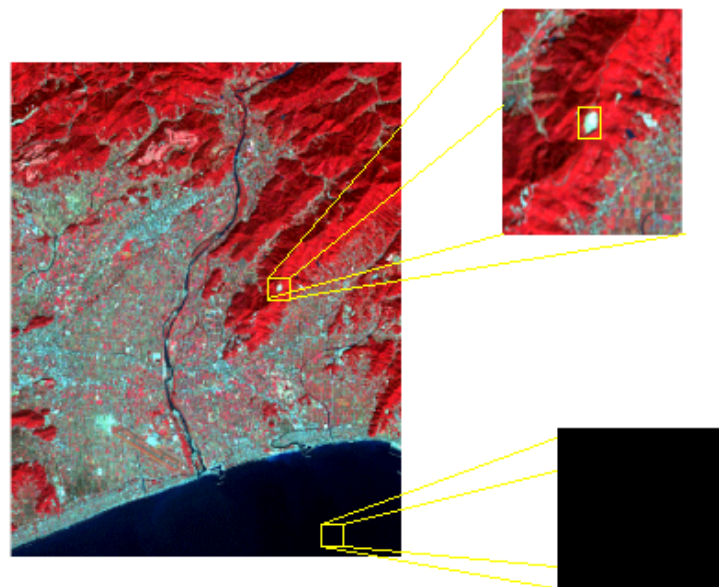


Figure 3.4: The input of minimum and maximum values were taken from dark pure water and pure bare soil areas

Table 3.1: The minimum inputs of each ASTER scene

Band	October	January	March
Band1	42	32	43
Band2	17	14	18
Band3	11	10	12

Table 3.2: The maximum inputs of each ASTER scene

Band	October	January	March
Band1	117	97	136
Band2	106	86	125
Band3	83	71	92

Table 3.3 shows the outputs of the minimum and maximum inputs which were set by the author, secondary offset value 91 was added to avoid minus values.

Table 3.3: The outputs of the minimum and maximum inputs for the ASTER images

Band	Minimum	Maximum
Band1	31	118
Band2	13	107
Band3	9	84

Table 3.4, 3.5 and 3.6 show the gains and offsets of the normalization equations.

Table 3.4: The gains and offsets of the normalization equations for the October ASTER scene

Band	Gain	Offset
Band1	1.16	-17.72
Band2	1.06	-4.96
Band3	1.04	-2.46

Table 3.5: The gains and offsets of the normalization equations for the January ASTER scene

Band	Gain	Offset
Band1	1.34	-11.83
Band2	1.31	-5.28
Band3	1.23	-3.30

Table 3.6: The gains and offsets of the normalization equations for the March ASTER scene

Band	Gain	Offset
Band1	0.94	-9.22
Band2	0.88	-2.81
Band3	0.94	-2.25

Figure 3.5, 3.6, and 3.7 show the histogram of VNIR bands for the ASTER images. Especially the brightness of the January scene is lower than other scenes because the scene's sun angle is lower than other scenes'.

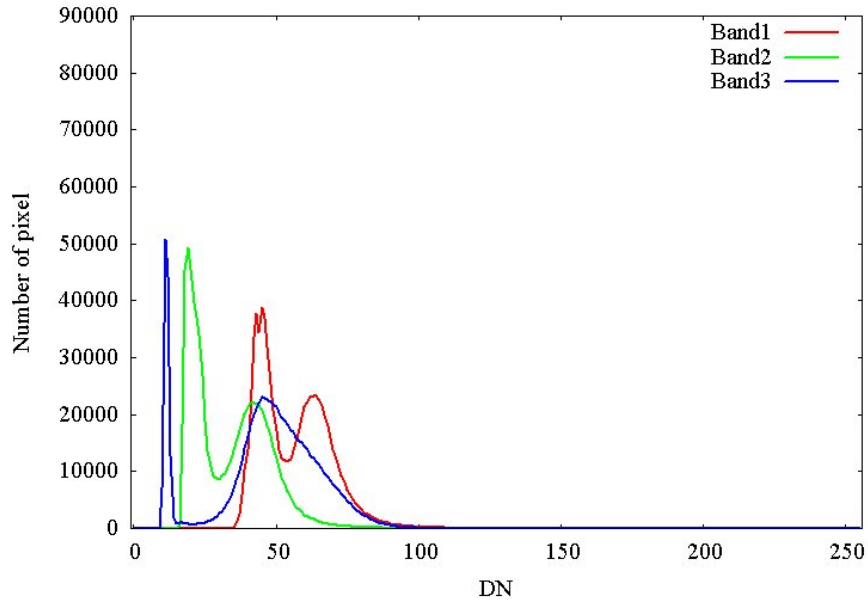


Figure 3.5: The histogram of VNIR bands for the October scene

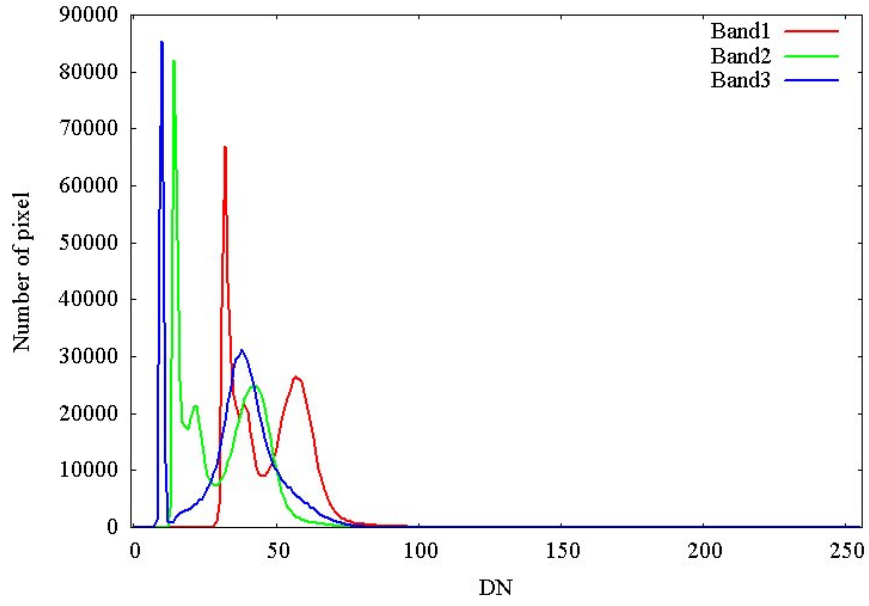


Figure 3.6: The histogram of VNIR bands for the January scene

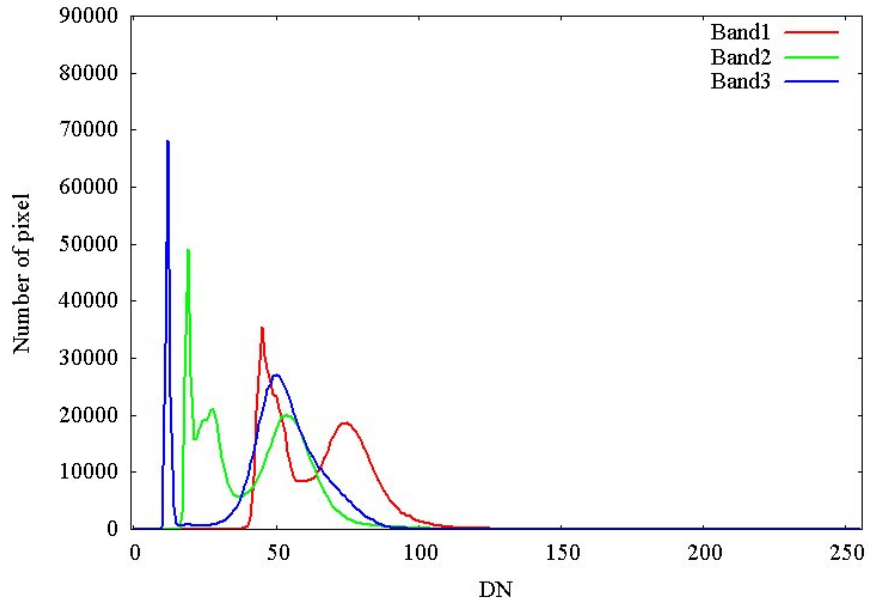


Figure 3.7: The histogram of VNIR bands for the March scene

Following figures show the normalization results of each band of the three scenes, the widths and positions of DN distributions of the three scenes could be controlled. Figure 3.8, 3.9 and 3.10 show the histogram of normalization results of band1 for the ASTER images.

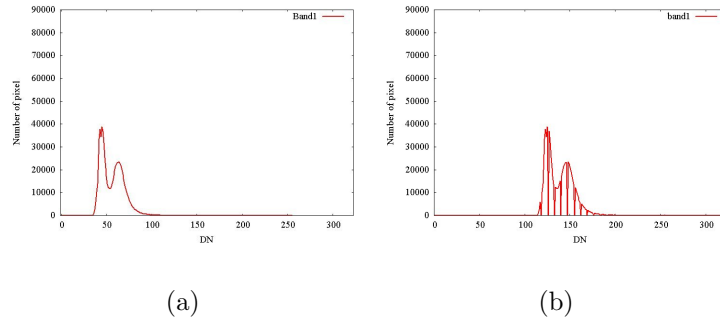


Figure 3.8: The normalization result of October scene's band1, (a) before normalization, (b) after normalization

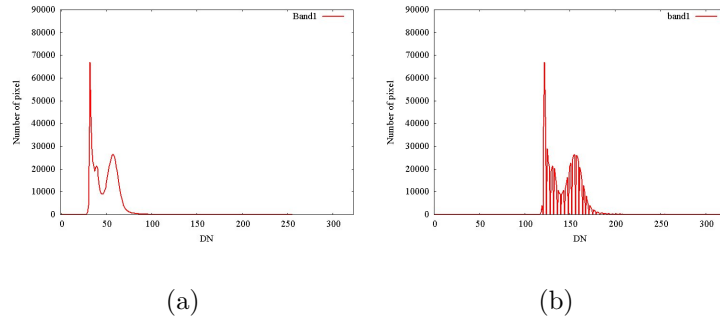


Figure 3.9: The normalization result of January scene's band1, (a) before normalization, (b) after normalization

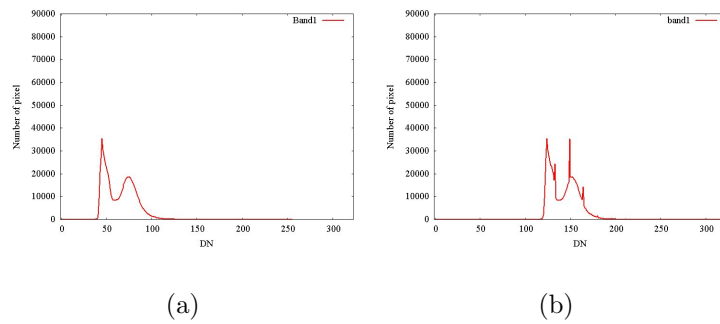


Figure 3.10: The normalization result of March scene's band1, (a) before normalization, (b) after normalization

Figure 3.11, 3.12, and 3.13 show the histogram of normalization result of band2 for the ASTER images

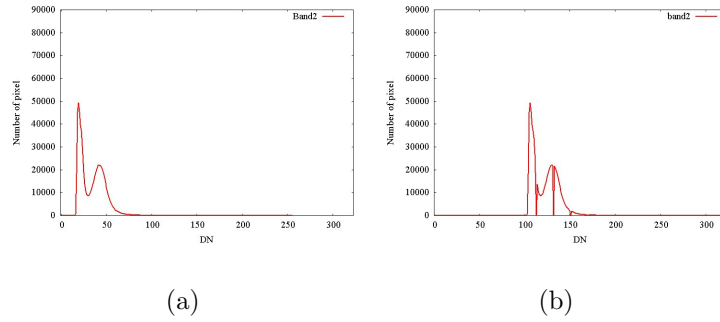


Figure 3.11: The normalization result of October scene's band2, (a) before normalization, (b) after normalization

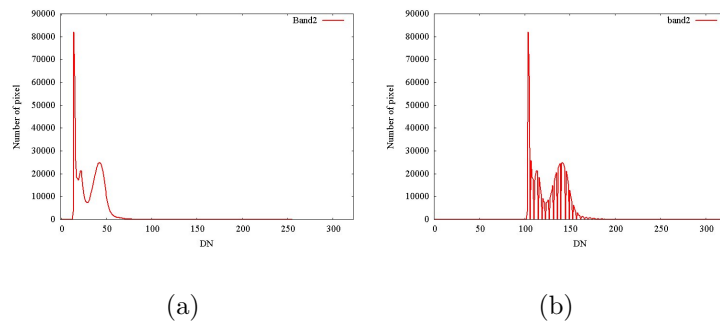


Figure 3.12: The normalization result of January scene's band2, (a) before normalization, (b) after normalization

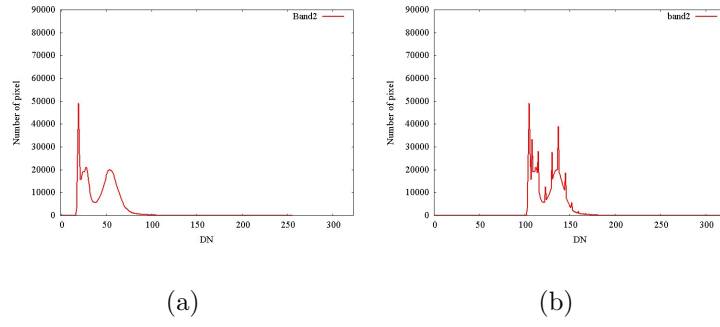


Figure 3.13: The normalization result of March scene's band2, (a) before normalization, (b) after normalization

Figure 3.14, 3.15, and 3.16 show the histogram of normalization result of band3 for the ASTER images.

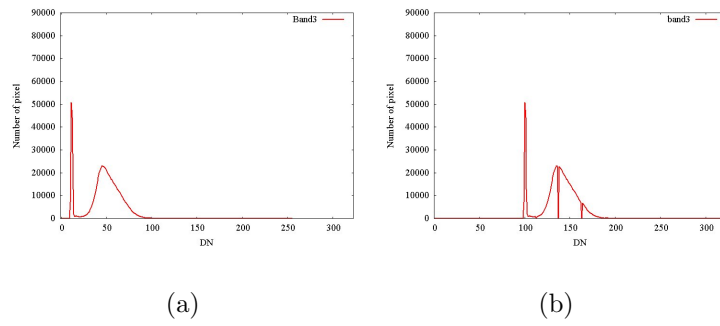


Figure 3.14: The normalization result of October scene's band3, (a) before normalization, (b) after normalization

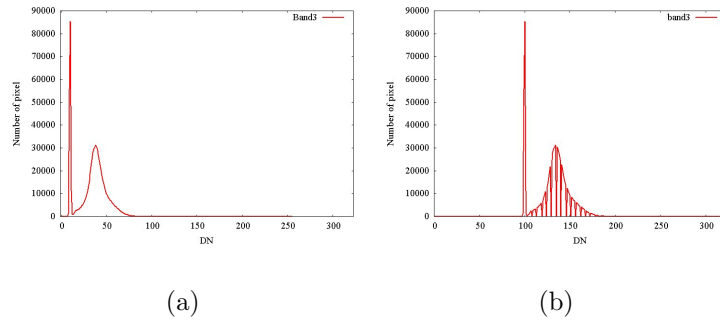


Figure 3.15: The normalization result of January scene's band3, (a) before normalization, (b) after normalization

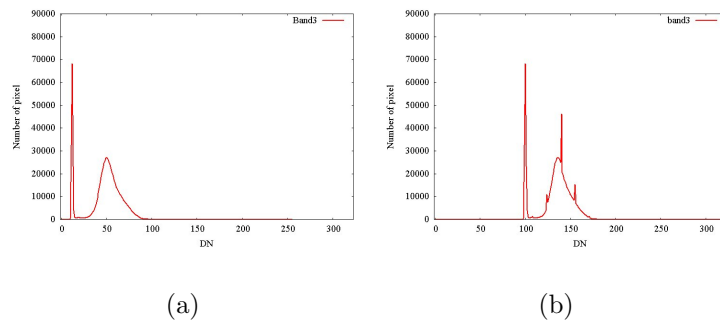


Figure 3.16: The normalization result of March scene's band3, (a) before normalization, (b) after normalization

Chapter 4

LINEAR MIXTURE ANALYSIS

The proportions of land covers in a pixel are used in the proposed method to reduce the change detection errors, thus conventional classification methods, which represent only one major class in a pixel, are not fit to this study. The linear mixture analyses of the ASTER images were carried out to investigate landcover proportions.

4.1 Linear mixture analysis

Linear mixture analysis is a commonly used method to decompose mixture proportions of pure landcovers in a pixel. This method is different from statistical classification approach because it is based on the physical mixture model of various spectral reflectances.

The linear mixture analysis is based on several assumptions: limited numbers of pure land-cover elements are existed in a pixel, and the sum of the proportion of the all endmembers which are pure information classes in a pixel, should be equal to one (Equation 4.1), and the proportion of each endmember f must be exist between zero and one.

$$\sum_{i=1}^N = f_1 + f_2 + \dots + \dots + f_N \quad (4.1)$$

where f_1 f_N is the proportion of each endmemebbers in a pixel, N is the total number of endmembers. Additionally, the observed spectra DN_i in the band i consists of some unknown errors (e) and the numbers (fDN) which were generated by multiplying the fraction of each endmember (f) and each DNs that would be observed in each band (Equation 4.2).

$$DN_i = f_1 DN_{i,1} + f_2 DN_{i,2} + \dots + \dots + f_n DN_{i,N} + e_i \quad (4.2)$$

The proportions of endmembers f become unknown in the linear mixture analysis. Spectral unmixing equations are required to obtain f . To establish spectral unmixing equations, the spectral signatures of endmembers (C) which are the coefficients of a spectral unmixing equations,

are estimated using training data (equation 4.3). In this process, proportions of endmembers f in the equation 4.2 become the existence proportions of landcovers (R) in a pixel (known) because the existence proportions of landcovers are obtained from the training data, the DN_i which are obtained from training data also become known, DN_i, N in the equation 4.2 become the C_i, N which are the spectral signatures of endmembers. The coefficients (C) can be obtained using least square method: equation 4.4 shows the matrix form of the equation 4.3, residuals minimized solution (C) can be obtained from equation 4.5 and equation 4.6.

$$DN_i = R_1 C_{i,1} + R_2 C_{i,2} + \dots + \dots + R_N C_{i,N} + e_i \quad (4.3)$$

where, DN are observed digital numbers (known), C are spectral signatures of endmembers (unknown), R are the existence proportions of landcovers in a pixel (known), e are unknown errors, i is pixel order, and N is band.

$$DN_n = \sum_{i=1}^M R_i C_{i,n} + e_n \quad (4.4)$$

$$\rho = \sum_{n=1}^k (DN_n - \sum_{i=1}^M R_i C_{i,n})^2 = \sum_{n=1}^k e_n^2 \quad (4.5)$$

where ρ is the sum of the squares of the residuals.

$$\frac{\partial \rho}{\partial C_1} = \frac{\partial \rho}{\partial C_2} = \dots = \frac{\partial \rho}{\partial C_k} = 0 \quad (4.6)$$

The number of necessary equations is decided according to the number of endmembers because the unknown is the proportion of each endmember in the spectral unmixing equations. Equation 4.7 shows the typical form of linear spectral unmixing equation. Spectral unmixing can be carried out using the DN of each band and the spectral signature of each endmember C . In this process, the R in the equation 4.4 becomes f those are unknown. Equation 4.8 shows the matrix form of the Equation 4.7. Least square solution can be obtained by using the pseudo inverse (Equation 4.9). The calculated proportion of each endmember must be existed between zero and one.

$$DN_n = \sum_{i=1}^M f_i C_{i,n} + e_n \quad (4.7)$$

where DN are observed digital numbers (known), C are spectral signature of endmembers (known), f are the existence proportion of endmembers in a pixel (unknown), e are unknown errors, i is pixel order, and n is band.

$$DN = fC + e \quad (4.8)$$

$$f = (C^T C)^{-1} C^T DN \quad 0 \leq f \leq 1 \quad (4.9)$$

4.2 Linear mixture analysis of the ASTER images

Water, vegetation and bare soil were selected as endmembers for the linear mixture analyses of the ASTER images, and thus it was assumed that pixels consisted of the three pure information classes. Three bands were required to calculate the proportion of the three endmembers, thus three VNIR bands of the ASTER images (15 meter resolution) were used for the spectral unmixing.

Equation 4.10 shows the linear mixture form in this study, DN and R taken from the training data were known in the equation. The sum of the existence ratios of the endmembers should be one (equation 4.11).

$$DN_i = (C_{wi}R_w + C_{vi}R_v + C_{bi}R_b) \quad (4.10)$$

where R are ratios of landcovers (known), C are spectral signatures of endmembers (unknown), DN are digital numbers (known), i is band, w is water, v is vegetation, and b is bare soil including urban.

$$R_w + R_v + R_b = 1 \quad (4.11)$$

To establish the linear mixture form for each endmember, the spectral signature was calculated using the thirty pixels of training data (ten per each endmember), and the training data were obtained from unchangeable area (Figure 4.1). The ratio of land covers and DNs were input to the equation 4.10, then the spectral signature of endmembers C could be obtained using least square method.

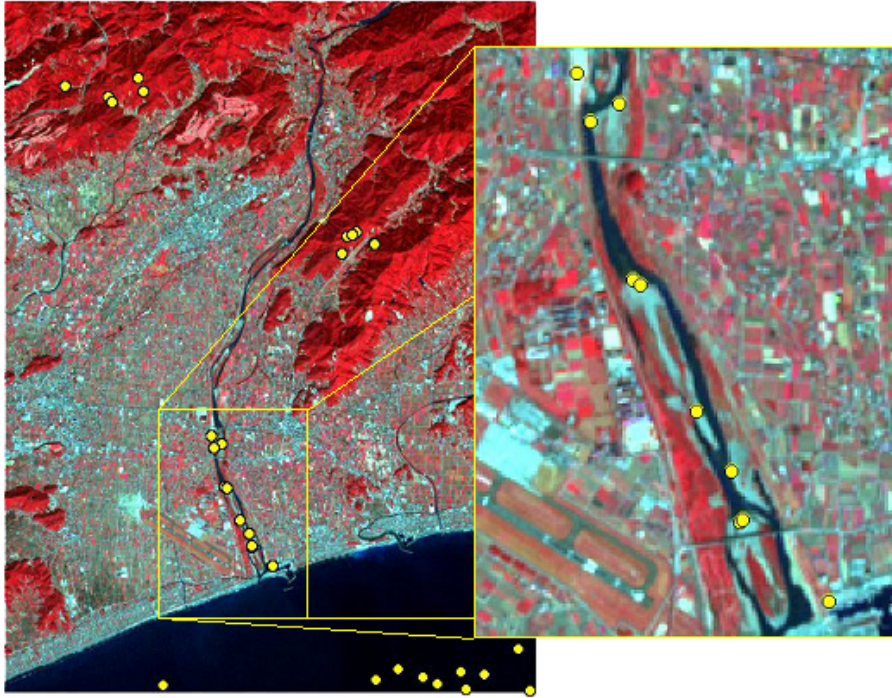


Figure 4.1: The locations where the training data were collected

Table 4.1 shows the result of spectral signature of each endmember. Table 4.2 shows the tolerance of the spectral unmixing calculated using equation 4.10.

Table 4.1: Spectral signature of each endmember

	C_w (Water)	C_v (Vegetation)	C_s (Soil)
Band 1	0.5451	0.5695	0.8031
Band 2	0.4655	0.4912	0.7004
Band 3	0.4440	0.7380	0.6058

Table 4.2: Spectral unmixing tolerances (average, square meters)

	October, 2001	January, 2002	March, 2002
Tolerance	16.33	23.00	24.78

$$\frac{\sum_{i=1}^{10} |E_{water,i} - C_{water,i}| + \sum_{i=1}^{10} |E_{vegetation,i} - C_{vegetation,i}| + \sum_{i=1}^{10} |E_{soil,i} - C_{soil,i}|}{30} \quad (4.12)$$

where E is expected the proportion of endmember, C is calculated the proportion of endmember.

The spectral unmixing could be performed with the calculated spectral signatures of the endmembers (Equation 4.11) out using the three linear mixture equations. The proportion of each endmember became unknown in the spectral unmixing. The DNs from the ASTER images and spectral signatures of endmembers were input to the linear mixture equation, then the decomposition of mixed pixel could be carried out.

Theoretically least square solution can be obtained by using the pseudo inverse; however the solutions are usually unstable due to the error term (Equation 4.6), thus an iterative method was used to obtain stable solutions of the spectral unmixing equations.

$$DN_i = (C_{w,i}f_w + C_{v,i}f_v + C_{b,i}f_b) \quad (4.13)$$

where f are the proportions of endmembers (unknown), C are spectral signatures of endmembers (known), DN are digital numbers (known), i is band, w is water, v is vegetation, and b is bare soil including urban.

Algorithm 1 shows the iterative method. The three unmixing equations were set up, then the DNs from an image were input. The estimated proportion of each endmember was input to the equation until the estimated proportion of each endmember became one. The differences (e: the error term) between input DNs and calculated DNs ($C_{w,i}f_w + C_{v,i}f_v + C_{b,i}f_b$) were calculated; when the error term reached the most minimum, the input proportions of endmembers became the solution of the spectral unmixing. Although this method is computationally expensive, stable solutions could be resulted.

```

e1, e2, e3 = 0
solfw, solfv, solfb = 0
min = 1

Begin
  for fw = 0, fw = fw + 0.1, until f equal 1
  for fv = 0, fv = fv + 0.1, until f equal 1
  for fb = 0, fb = fb + 0.1, until f equal 1

    if (fw + fv + fb) equal 1
      e1 = DN1 - (Cw,1fw + Cv,1fv + Cb,1fb)
      e2 = DN2 - (Cw,2fw + Cv,2fv + Cb,2fb)
      e3 = DN3 - (Cw,3fw + Cv,3fv + Cb,3fb)
    end if

    if (e1+e2+e3) ≤ min
      solfw = fw, solfv = fv, solfb = fb
      min = (e1 + e2 + e3)
    end if

  endfor
endfor
endfor
end

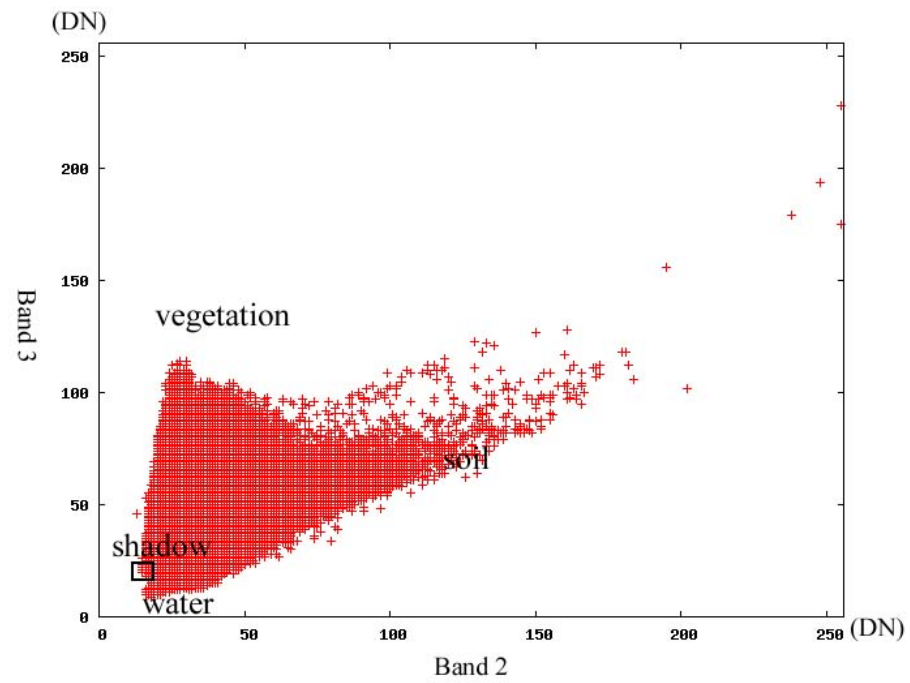
```

Algorithm 1. An iterative method for obtaining the stable solutions from the spectral unmixing equations

From figure 4.2 to 4.4 show the three normalized ASTER images and the scatter plot of their band2 and band3, the squared area represents shadow area, the shadow areas of the three images are close to water. From figure 4.5 to 4.7 show the linear mixture analysis results of three ASTER images. Shadowed vegetation areas of the three ASTER images contain water class because the spectral characteristic of shadow area was close to water class.

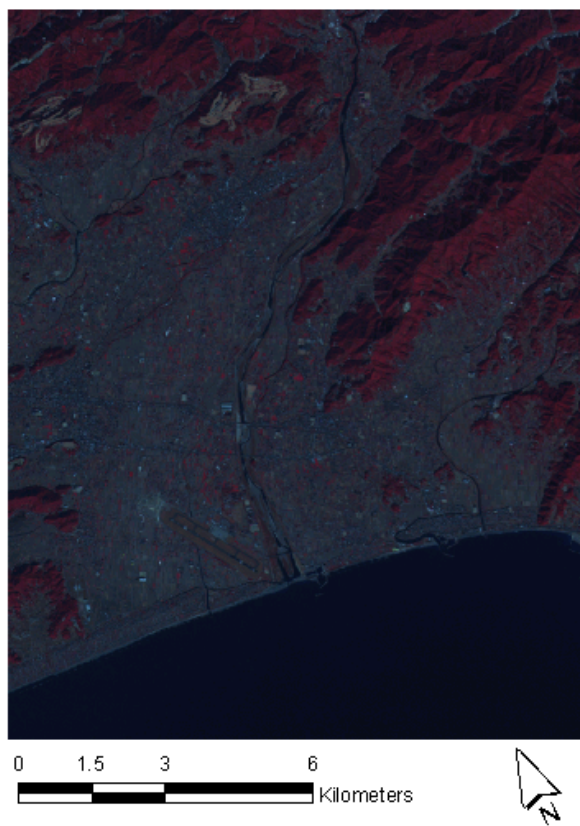


(a)

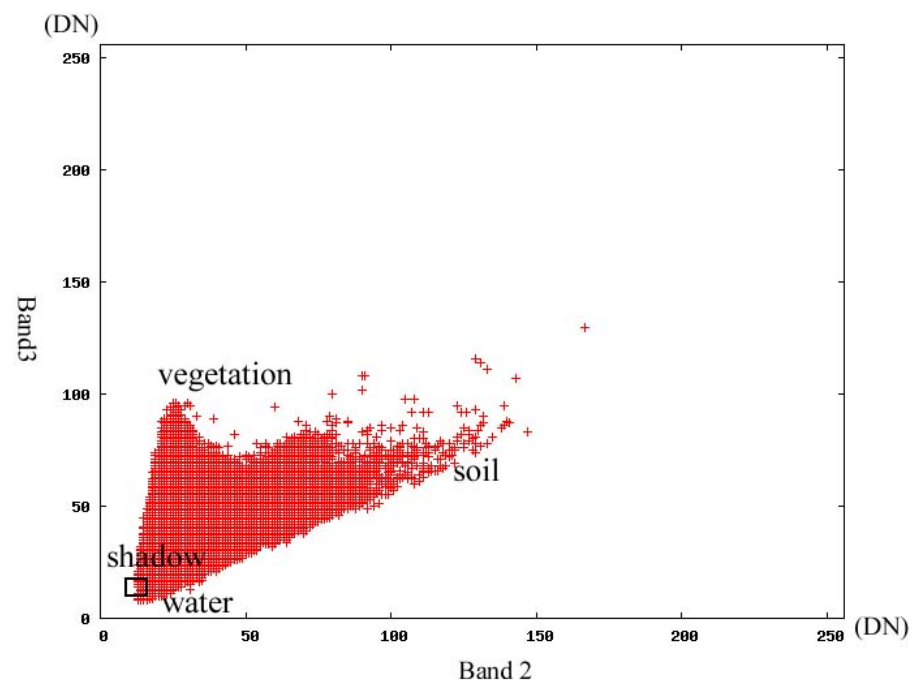


(b)

Figure 4.2: (a) The ASTER scene acquired in October 2001, (b) The scatter plot between band2 and band3

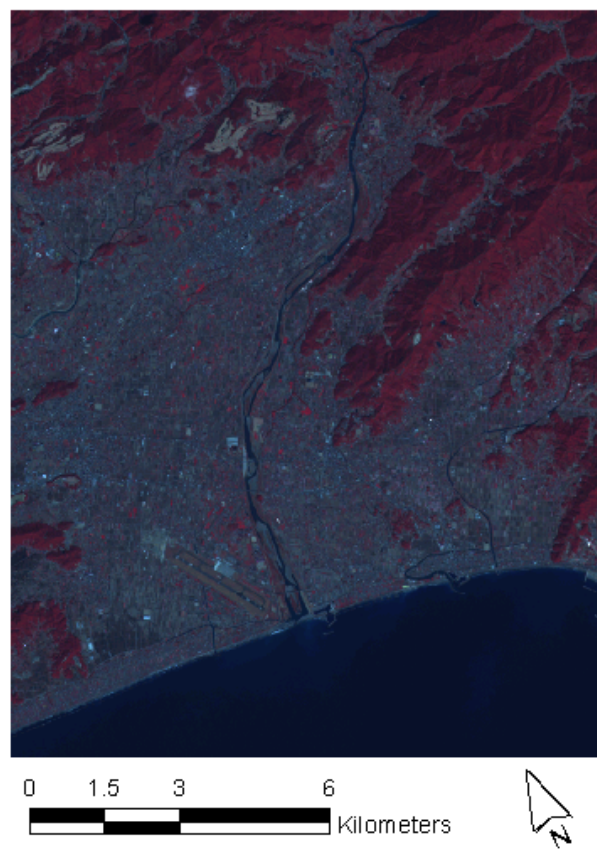


(a)

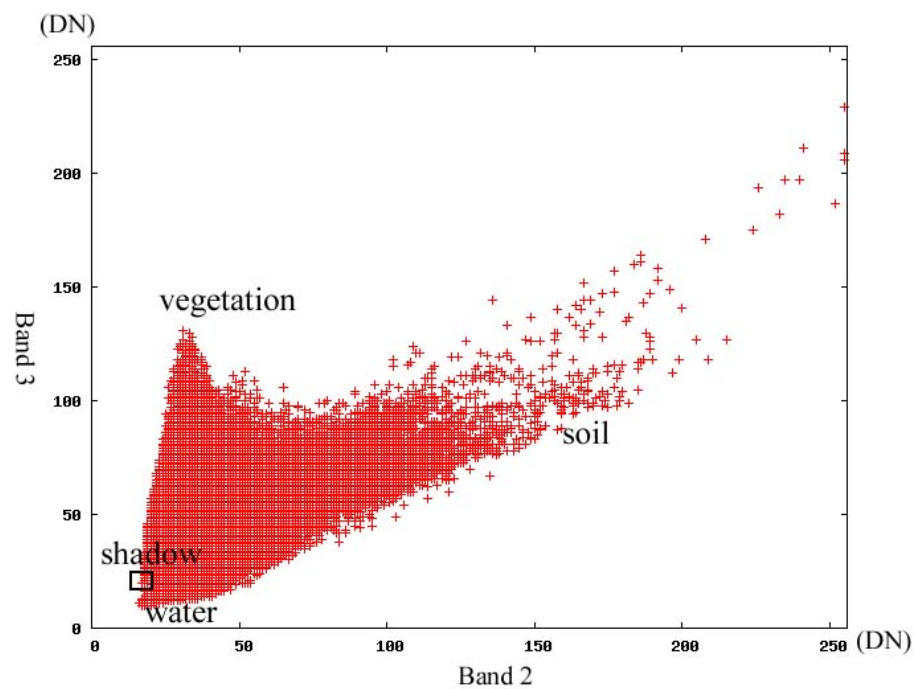


(b)

Figure 4.3: (a) The ASTER scene acquired in January 2002 , (b) The scatter plot between band2 and band3



(a)



(b)

Figure 4.4: (a) The ASTER scene acquired in March 2002, (b) The scatter plot between band2 and band3

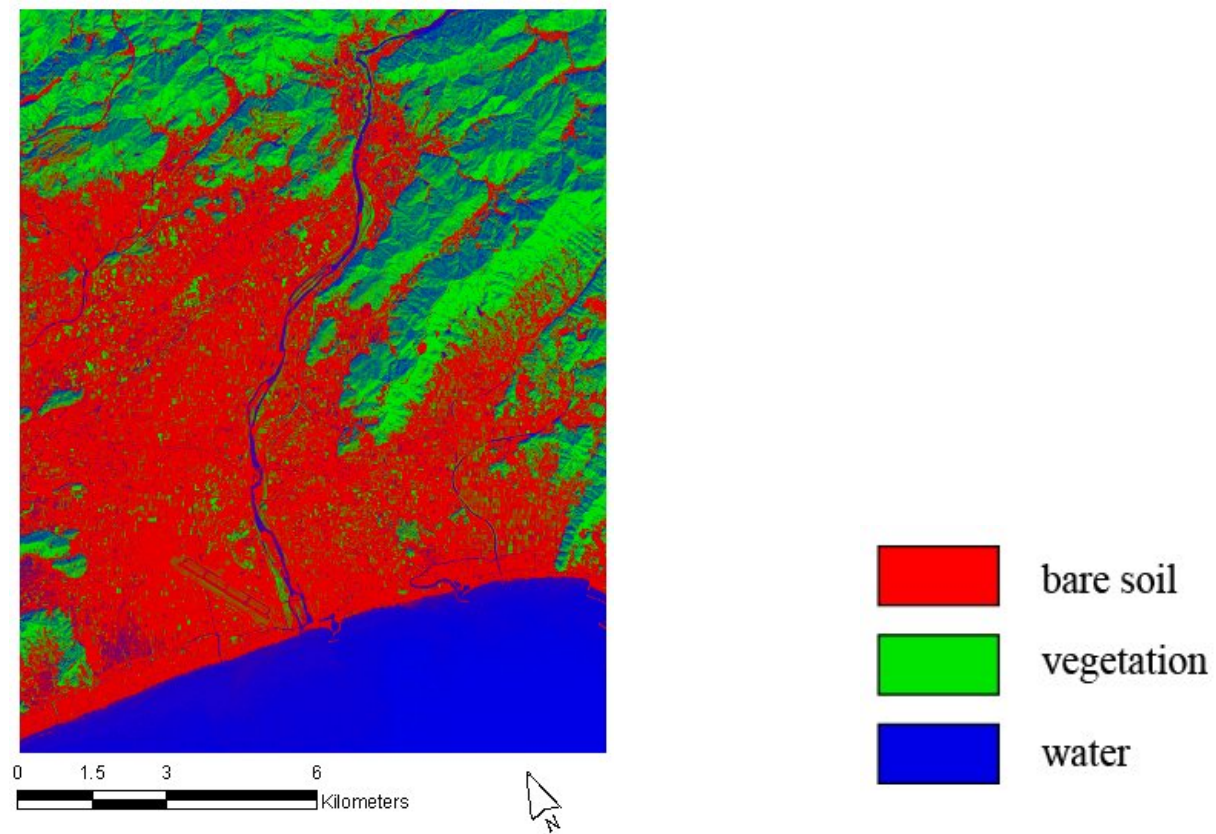


Figure 4.5: The result of linear mixture analysis of October scene

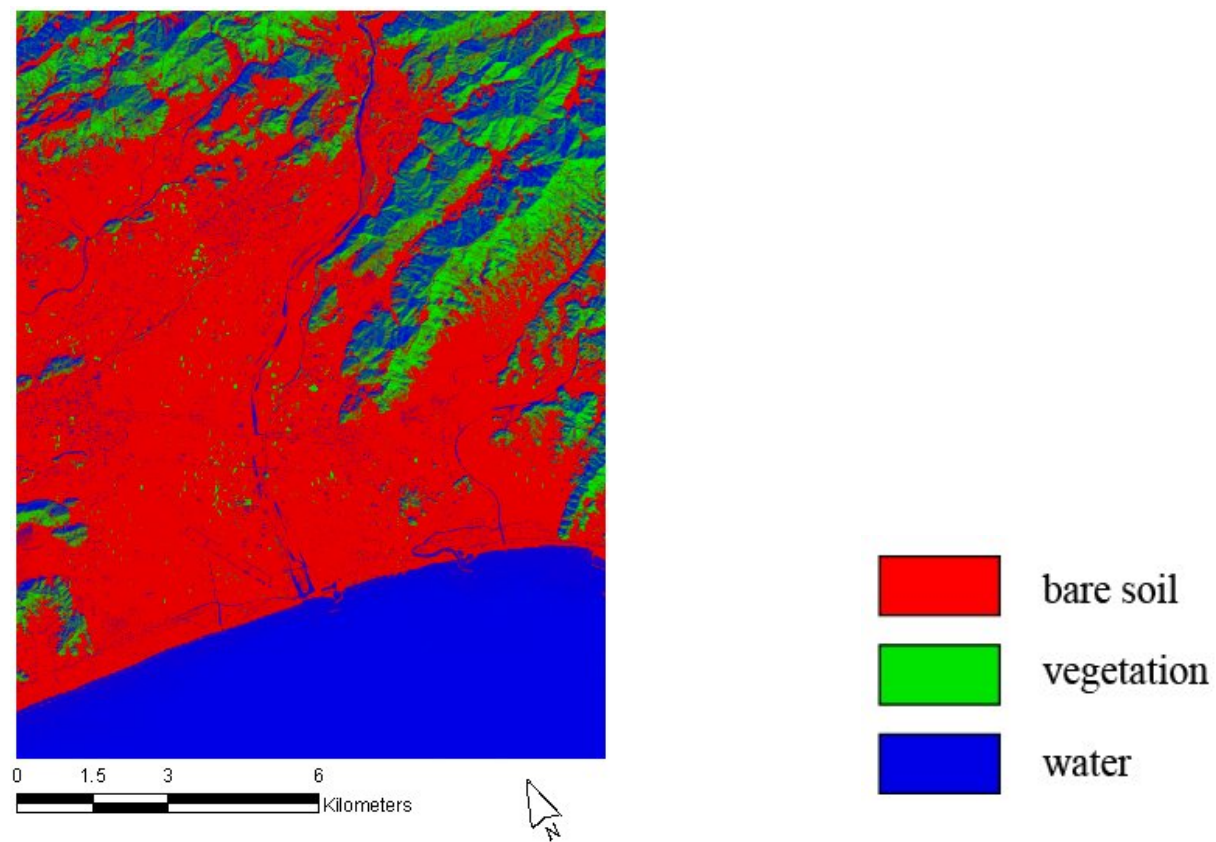


Figure 4.6: The result of linear mixture analysis of January scene

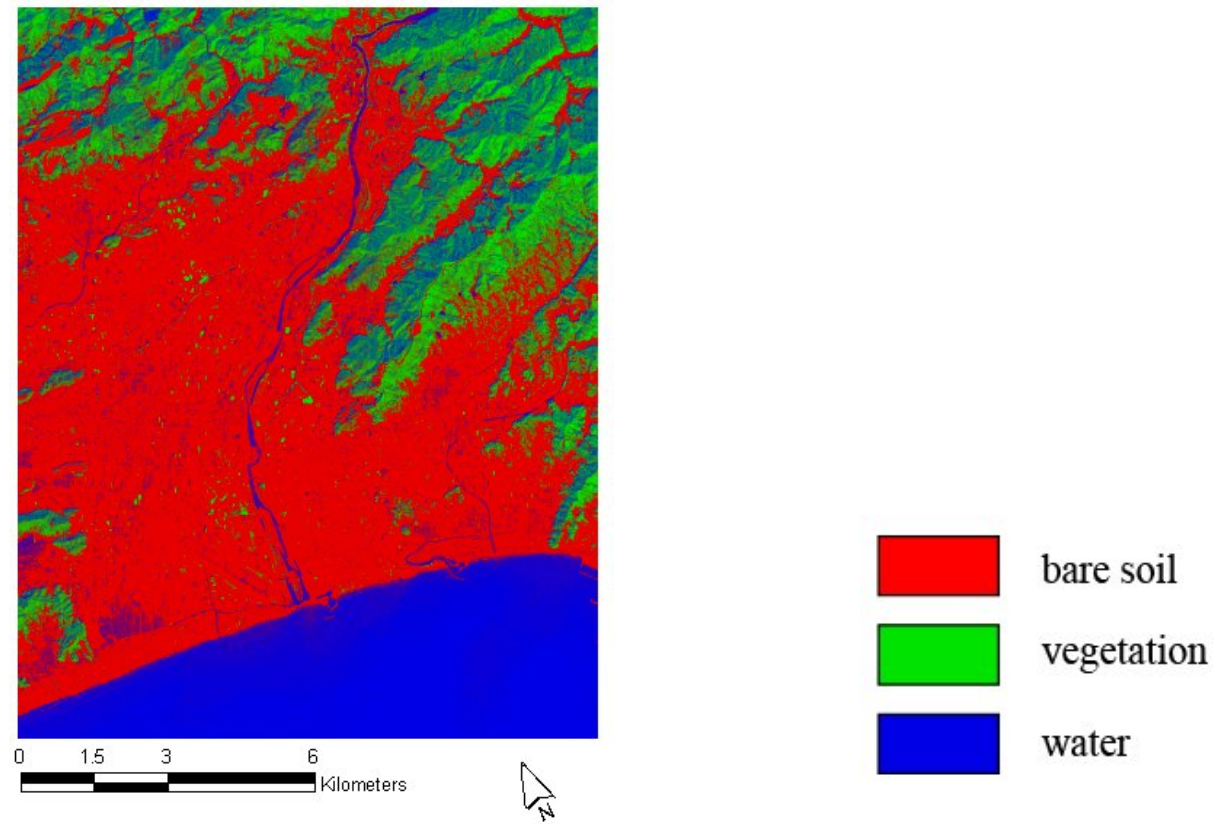


Figure 4.7: The result of linear mixture analysis of March scene

Chapter 5

ESTABLISHING GEOMETRICAL TRANSFORMS USING VERY HIGH RESOLUTION SATELLITE IMAGE

Geometrical transformations were required to perform the change detections using the ASTER images. Control points are required to establish a transformation. The accuracy of a transformation depends on the accuracy of control points. To obtain highly accurate control points, image matchings between the IKONOS image (very-high resolution data) and ASTER images (high resolution data) were carried out. In this study, the accuracy levels of the transformation were aimed to result less than 1/4 pixel in transformation error for effective change detection (Illsland, 2002).

5.1 Transformations

Transformations are carried out to convert a coordinate system into another coordinate system, to reduce geometrical distortion of a scanned map, and to register a satellite image.

5.1.1 Herlmert Transformation

Herlmert Transformation is used to correct the distortions of scale and rotation (Equation 5.1). To perform the transformation, at least two known points are necessary.

$$\begin{bmatrix} u \\ v \end{bmatrix} = \begin{bmatrix} a & b \\ -b & a \end{bmatrix} \begin{bmatrix} x \\ y \end{bmatrix} + \begin{bmatrix} x_0 \\ y_0 \end{bmatrix} \quad (5.1)$$

where equation parameters are a and b , map coordinates are x and y , the origin points of x and y are x_0 and y_0 , corresponding coordinates of x and y in an image are u and v , scale is $\sqrt{a^2 + b^2}$

,and rotation angle is $\tan\theta = b/a$.

5.1.2 Two-dimensional Affine transformation

Affine transformation is a two more parameter added Herlmert transformation, can correct distortions of scale, rotation and nonorthogonality (skew) (Equation 5.2). To perform the two-dimensional Affine transformation, at least three known points are necessary.

$$\begin{bmatrix} u \\ v \end{bmatrix} = \begin{bmatrix} a & b \\ c & d \end{bmatrix} \begin{bmatrix} x \\ y \end{bmatrix} + \begin{bmatrix} x_0 \\ y_0 \end{bmatrix} \quad (5.2)$$

where equation parameters are a,b,c and d.

5.1.3 Two-dimensional projective coordinate transformation

Two-dimensional projective coordinate transformation is used for the rectification of tilted images such as aerial photographs (Equation5.3). At least five known points are required to perform the transformation.

$$u = \frac{a_1x + b_1y + c_1}{a_3x + b_3y + 1} \quad v = \frac{a_2x + b_2y + c_2}{a_3x + b_3y + 1} \quad (5.3)$$

where equation parameters are a_1, a_2, a_3, b_1, b_2 and b_3 ; corresponding coordinates of x and y in an image are u and v .

5.2 Affine Transformation of the IKONOS

To build the geometrical transformations between the IKONOS image and the ASTER images, Affine transformation was used because the swath width of the IKONOS satellite is narrow (11km) enough to be applied the Affine transformation. Geometrical correction of the IKONOS and the ASTER images were already carried out, thus the adjustments of scale, rotation and skew were necessary.

5.2.1 Establishing transformations using the geometrically corrected IKONOS image

The Affine transformation of the IKONOS image was carried out two times (figure 5.1), because the image matching could not be carried out directly due to the coarse geometric correction of the ASTER images (figure 5.2). The first transformation was performed to align the ASTER images and the IKONOS image geometrically parallel, five control points obtained by visual

interpretation for each transformation were used for the first transformations. The detailed adjustments of the first transformations were performed using control points obtained by the area based image matching method. In this study, the IKONOS image was transformed to the three ASTER images, then the direct transformation which convert IKONOS coordinate system into the ASTER's, and the inverse transformation which convert the ASTER coordinate system into IKONOS coordinate system could be established.

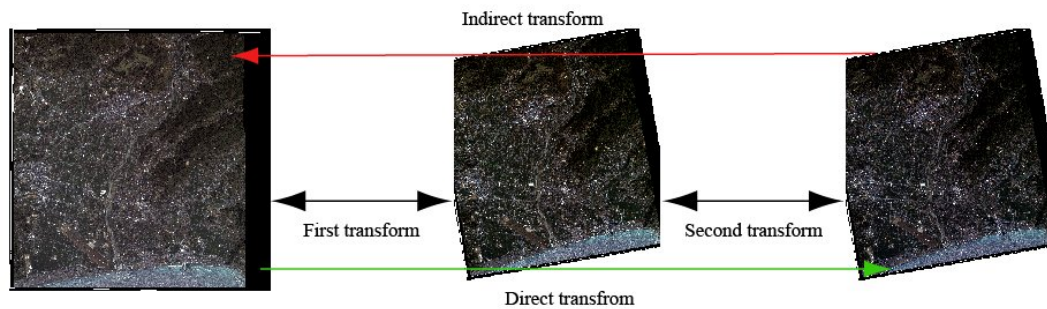


Figure 5.1: The direct transformation and inverse transformation

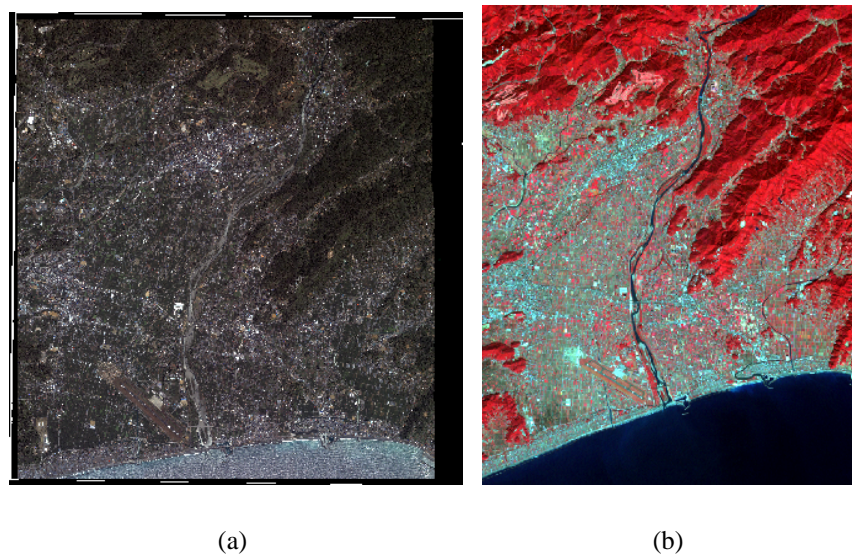


Figure 5.2: (a) The IKONOS image (b) the ASTER image acquired in October 2001

5.2.2 Digital image matching to obtain highly accurate GCP

As explained in the earlier section, control points are required to establish a transformation, thus finding control points is one of important processes. In this study, image matching method

was used to obtain accurate control points. Image matching is a computer based method for searching corresponding points between two images.

Digital image matching techniques can be divided into three categories: area-based, feature-based, and hybrid methods (Paul R. Wolf, 2000). Area-based matching known as cross correlation is a commonly used matching method in digital photogrammetry, the array of a template image is compared with the sub array of a target image in area-based image matching, while characteristics of extracted features are compared in feature-based image matching. Hybrid method is a combination of the area-based matching and the feature-based matching.

The feature based and hybrid methods cannot be used due to the resolution difference between the ASTER (15m) and IKONOS (1m), thus the area-based matching method was used in this study. For image matching, the source image and target image should be put on an epipolar line which is a geometrical constraint to set searching area and direction (Figure 5.3).

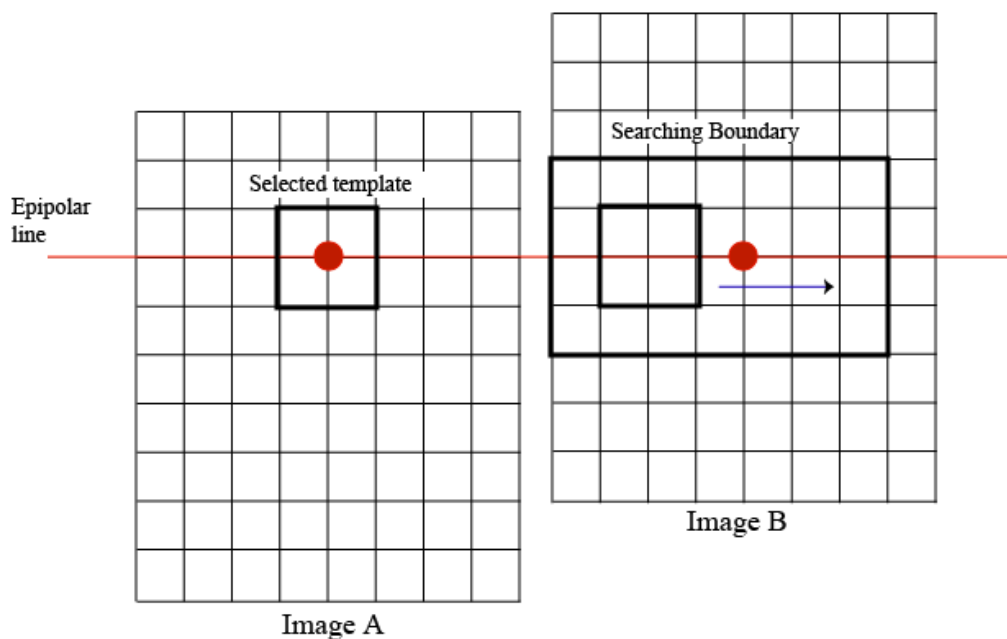


Figure 5.3: Area based template matching

The correlations between template images and searching templates were evaluated to measure the degree of the two images' similarity, then the corresponding locations of the templates could be found when the correlation reaches maximum pick (Figure 5.4).

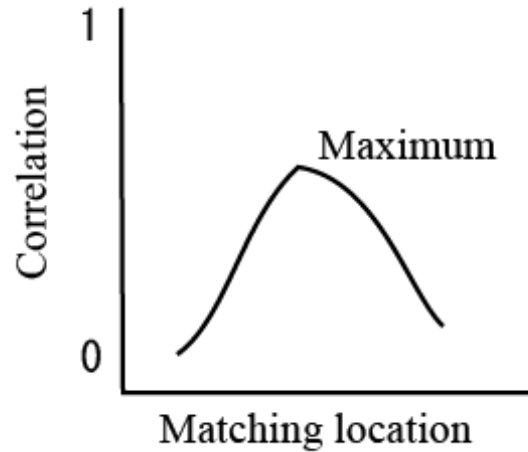


Figure 5.4: Finding corresponding location of a template using correlation

The correlation between a template image and a target image can be calculated using equation 5.4.

$$C = \frac{\sum_{i=1}^m \sum_{j=1}^n [(A_{ij} - \bar{A})(B_{ij} - \bar{B})]}{\sqrt{\sum_{i=1}^m \sum_{j=1}^n (A_{ij} - \bar{A})^2 \sum_{i=1}^m \sum_{j=1}^n (B_{ij} - \bar{B})^2}} \quad (5.4)$$

where C is the correlation of the two images, i is column, and j is row.

5.2.3 Image matchings between the IKONOS templates and ASTER images

Accurate GCP points were required to perform more detailed registration, thus image matchings between the two images were carried out. The spectral range of IKONOS' band2 is close to ASTER's band1, and the spectral range of IKONOS' band3 is close to ASTER's band2, thus the correlations between the template images from IKONOS' band2 and the ASTER's band1 image on one hand, and between the template images from IKONOS' band3 and ASTER's band2 images on the other hand were carried out. Five GCPs for the October scene, four GCPs for the January scene, and five GCPs for March scene could be obtained.

From figure 5.5 to 5.10 show the searching areas on the ASTER acquired in October 2001 (false composite, r: band3, g: band2, b: band1), template images from the IKONOS image

(false composite, r: band4, g: band3, b: band2), and the results of image matchings.

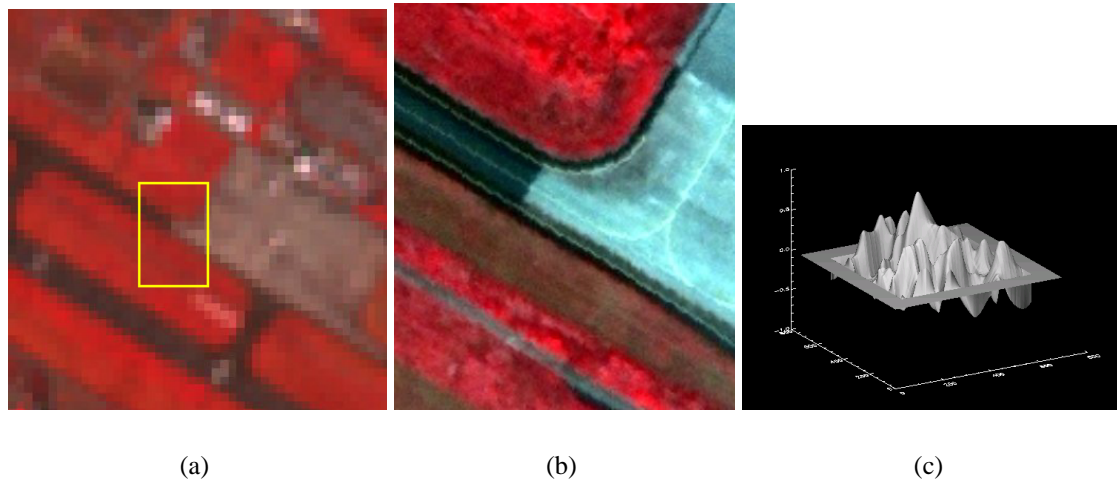


Figure 5.5: GCP 1 for the October scene, (a) searching area on the ASTER acquired in October 2001, (b) a template on the IKONOS, (c) correlation image, correlation: 0.92 (band 2), 0.90 (band 3)

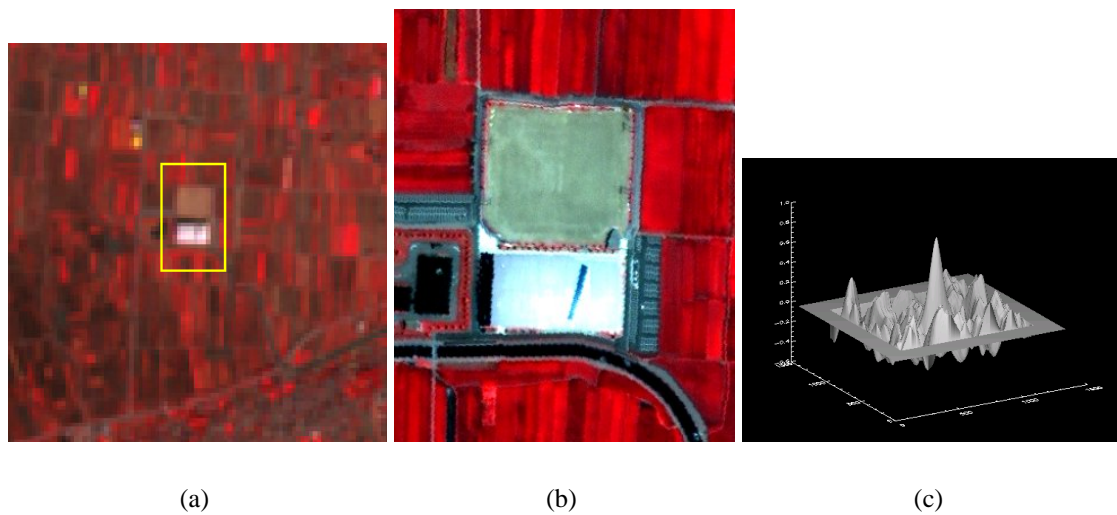


Figure 5.6: GCP 2 for the October scene, (a) searching area on the ASTER acquired in October 2001, (b) a template on the IKONOS, (c) correlation image, correlation: 0.85 (band2), 0.79 (band3)

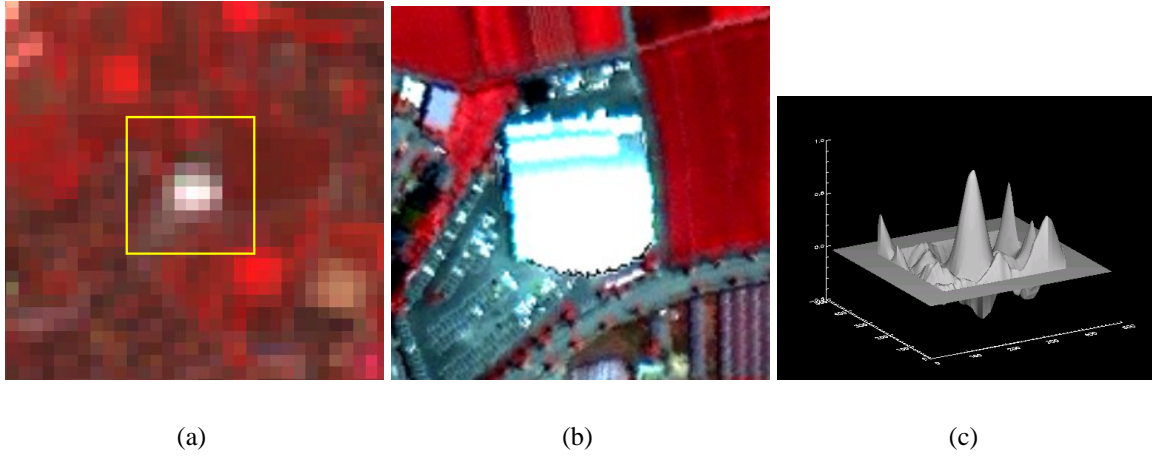


Figure 5.7: GCP 3 for the October scene, (a) searching area on the ASTER acquired in October 2001, (b) a template on the IKONOS, (c) correlation image, correlation: 0.86 (band2), 0.86 (band3)

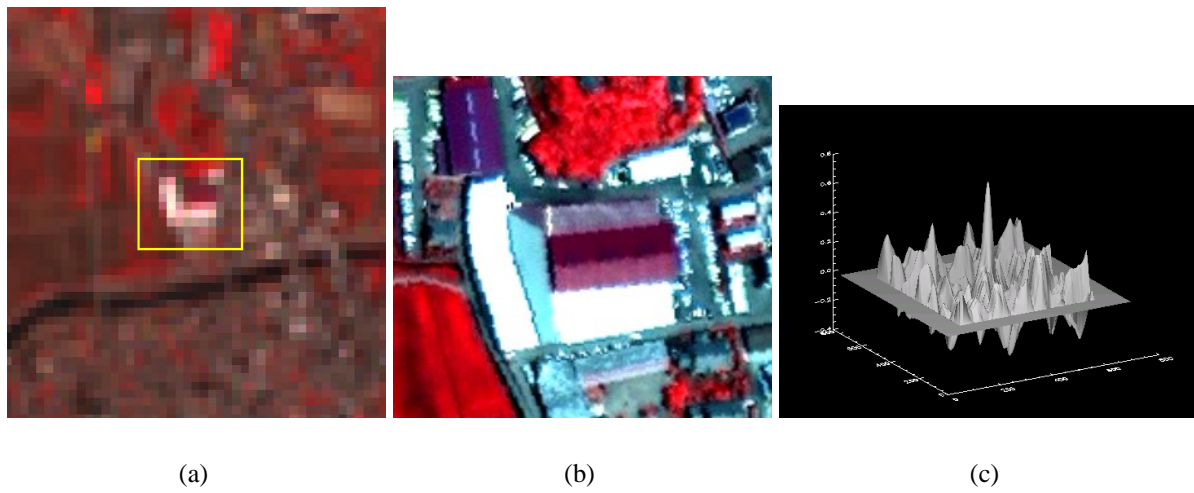


Figure 5.8: GCP 4 for the October scene, (a) searching area on the ASTER acquired in October 2001, (b) a template on the IKONOS, (c) correlation image, correlation: 0.75 (band 2), 0.74 (band 3)

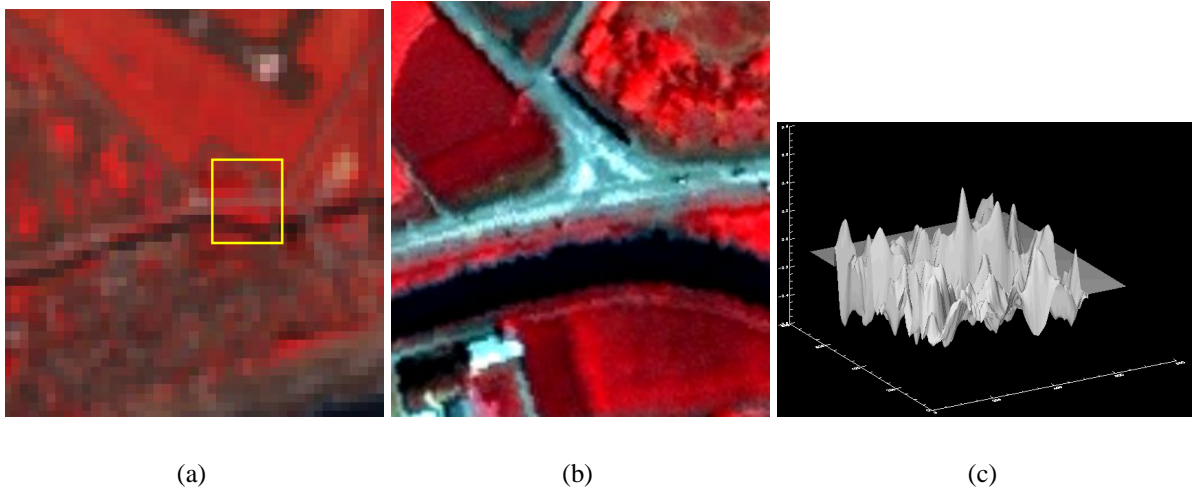


Figure 5.9: GCP 5 for the October scene, (a) searching area on the ASTER acquired in October 2001, (b) a template on the IKONOS, (c) correlation image, correlation: 0.67 (band2), 0.65 (band3)

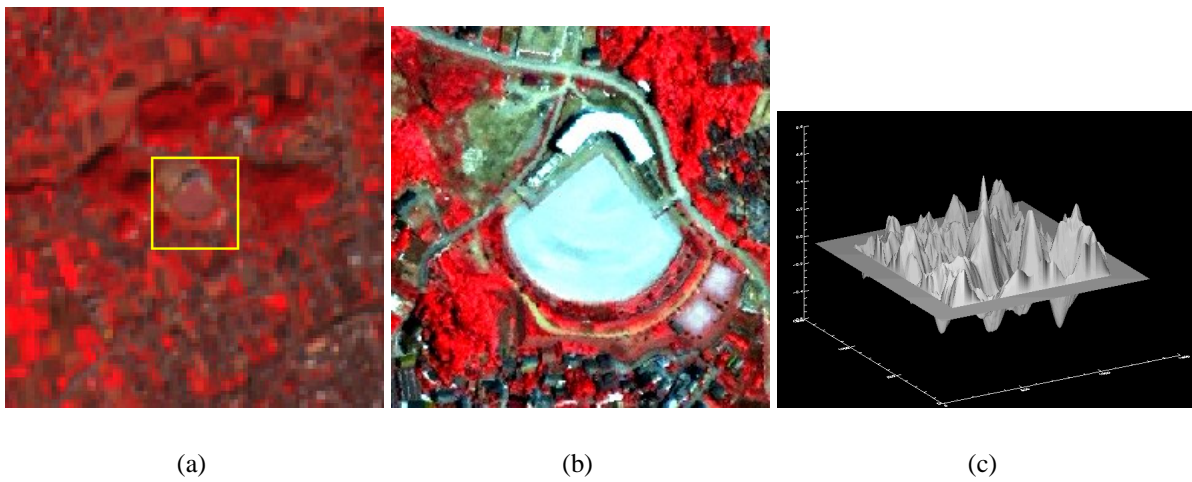


Figure 5.10: GCP 5 for the October scene, (a) searching area on the ASTER acquired in October 2001, (b) a template on the IKONOS, (c) correlation image, correlation: 0.90 (band2), 0.83 (band3)

From figure 5.11 to 5.14 show the searching areas on the ASTER acquired in January 2002, template images from the IKONOS image, and the results of image matchings.

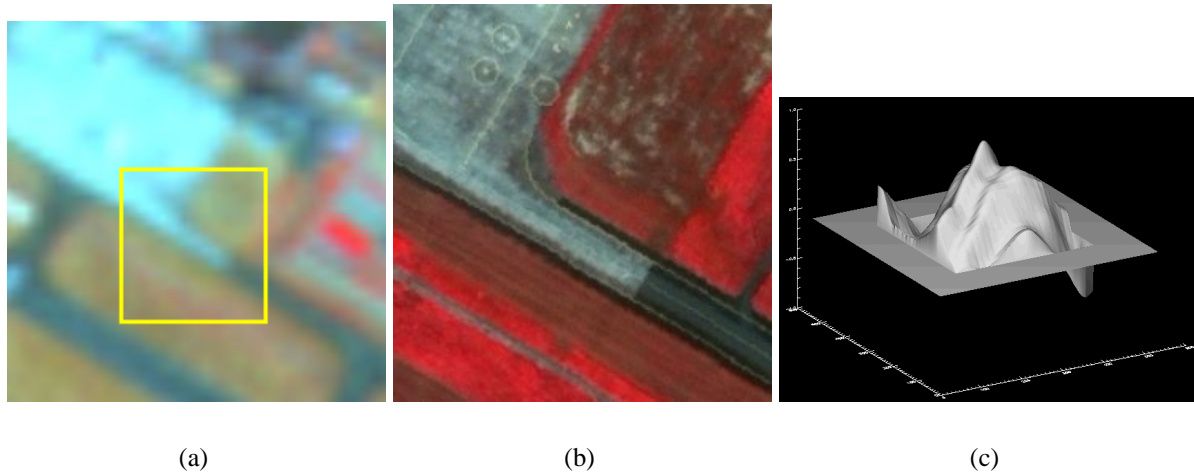


Figure 5.11: GCP 1 for the January scene, (a) searching area on the ASTER acquired in January 2002, (b) a template on the IKONOS, (c) correlation image, correlation: 0.90 (band2), 0.83 (band3)

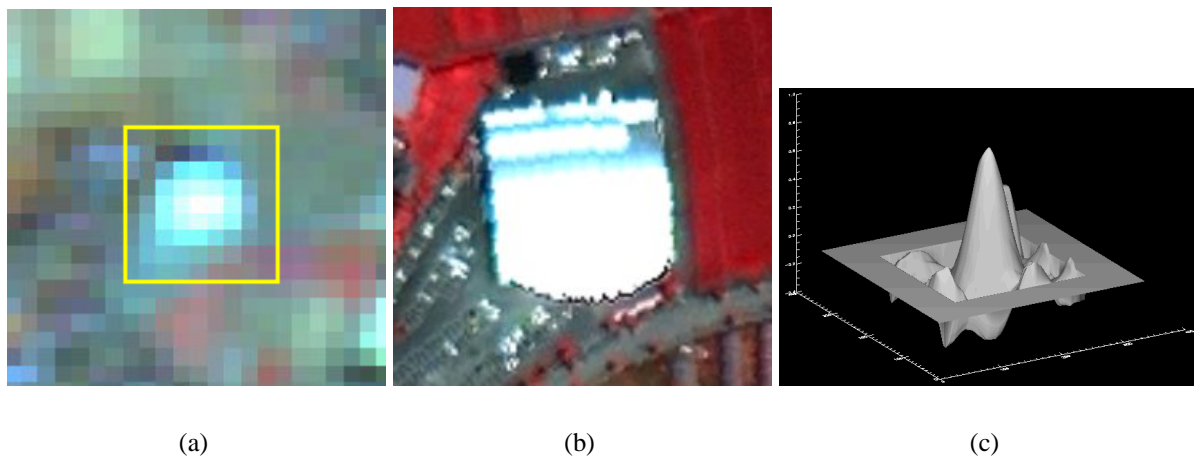


Figure 5.12: GCP 2 for the January scene, (a) searching area on the ASTER acquired in January 2002, (b) a template on the IKONOS, (c) correlation image, correlation: 0.84 (band2), 0.82 (band3)

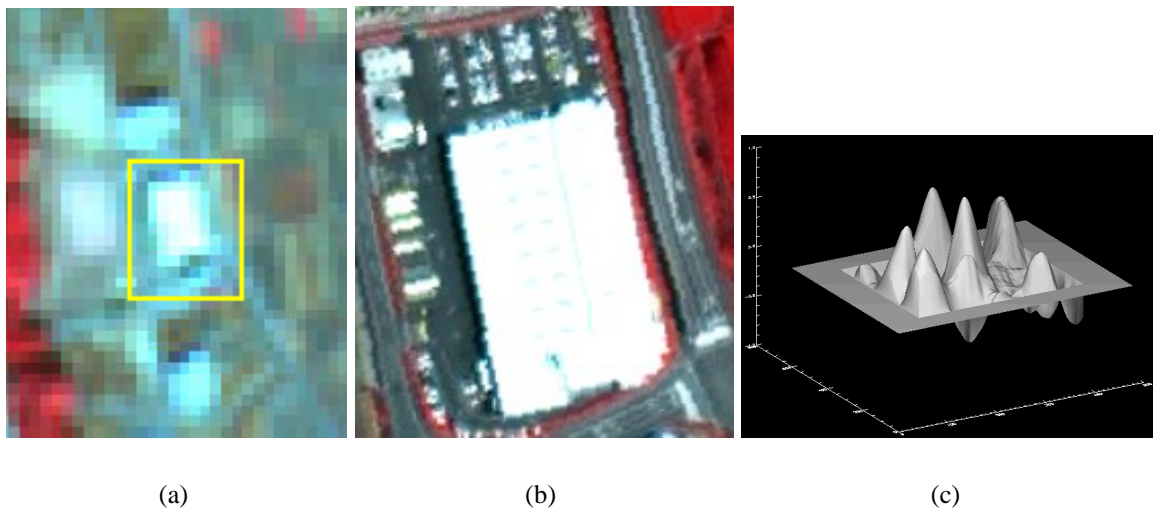


Figure 5.13: GCP 3 for the January scene,(a) searching area on the ASTER acquired in January 2002, (b) a template on the IKONOS, (c) correlation image, correlation: 0.83 (band2), 0.81 (band3)

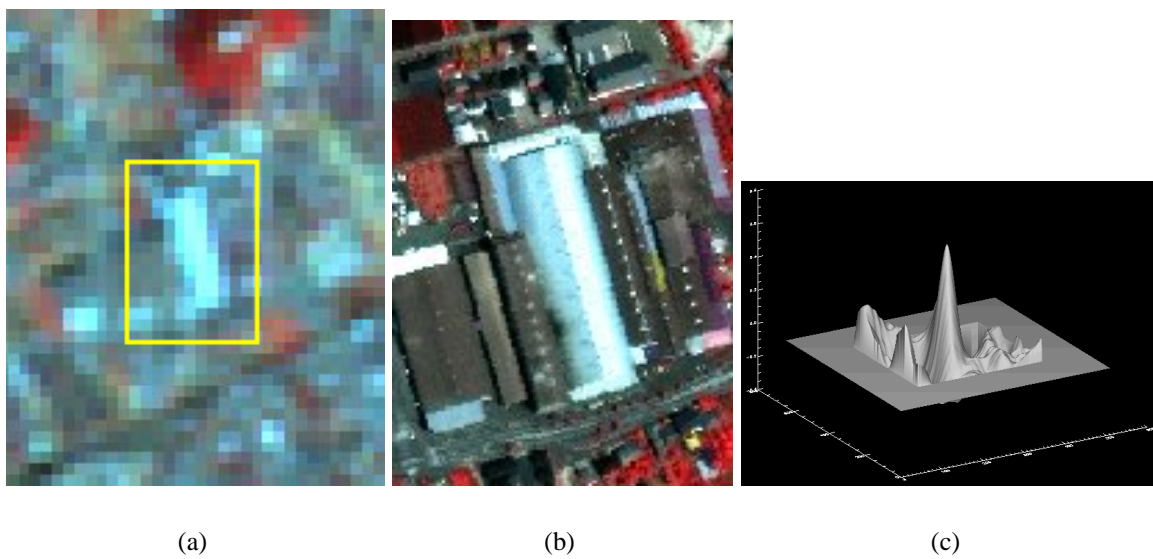


Figure 5.14: GCP 4 for the January scene,(a) searching area on the ASTER acquired in January 2002, (b) a template on the IKONOS, (c) correlation image, correlation: 0.67 (band1), 0.61 (band2)

From figure 5.15 to 5.19 show the searching areas on the ASTER acquired in March 2002, template images from the IKONOS image, and the results of image matchings.

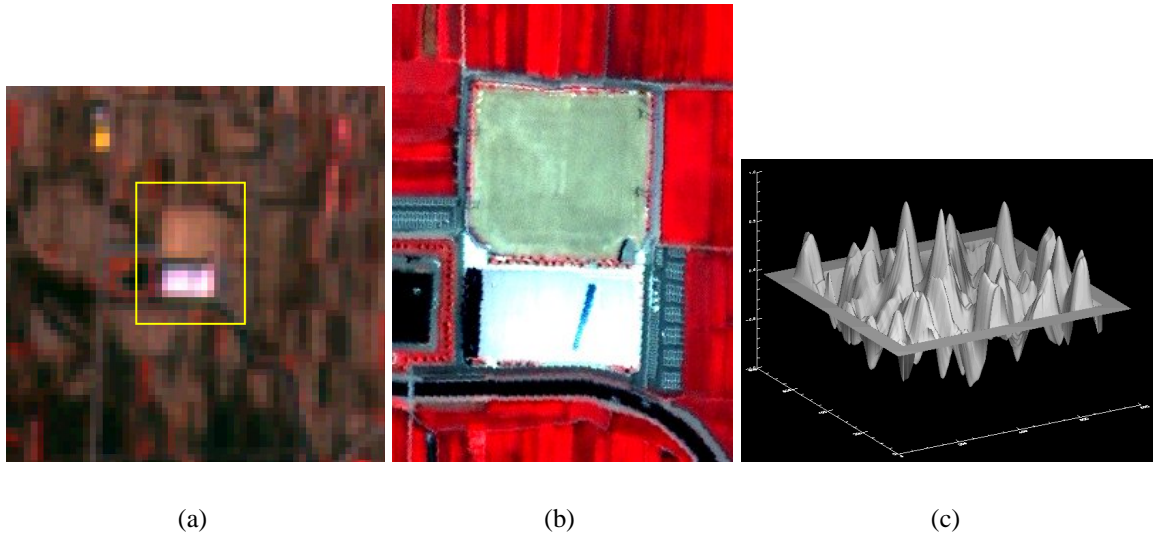


Figure 5.15: GCP 1 for the March scene,(a) searching area on the ASTER acquired in March 2002, (b) a template on the IKONOS, (c) correlation image, correlation: 0.82 (band1), 0.76 (band2)

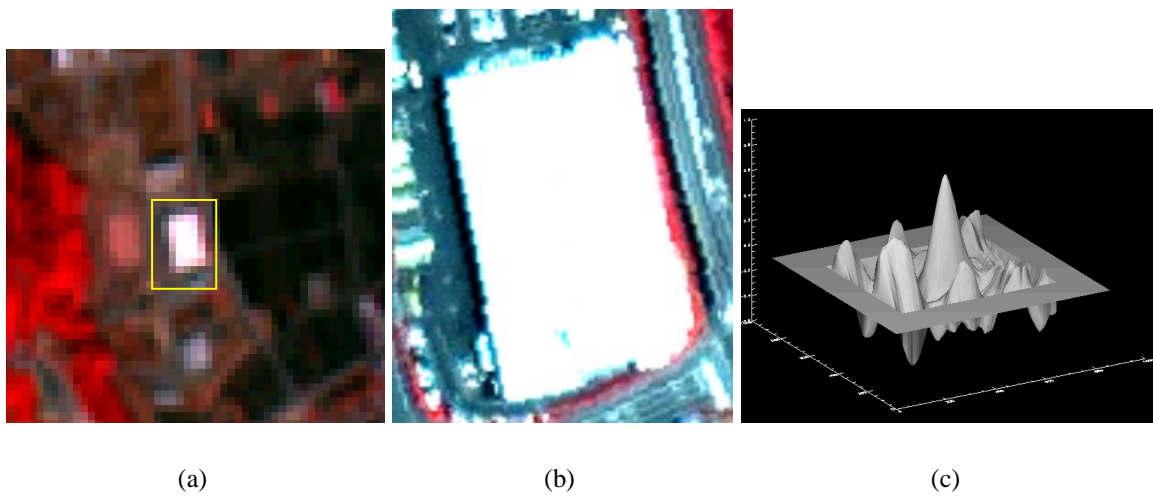


Figure 5.16: GCP 2 for the March scene,(a) searching area on the ASTER acquired in March 2002, (b) a template on the IKONOS, (c) correlation image, correlation: 0.84 (band2), 0.82(band3)

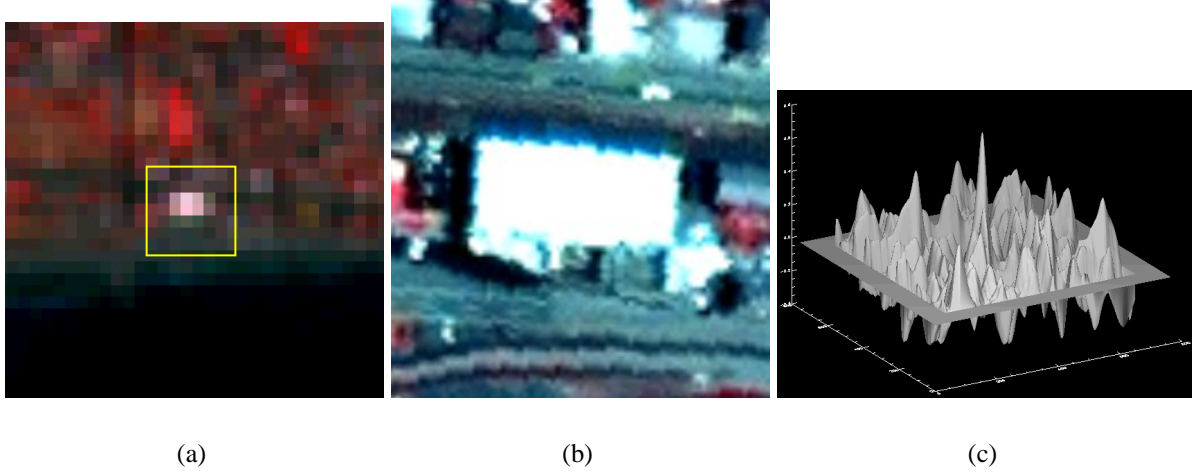


Figure 5.17: GCP 3 for the March scene,(a) searching area on the ASTER acquired in March 2002, (b) a template on the IKONOS, (c) correlation image, correlation: 0.74 (band2), 0.72 (band3)

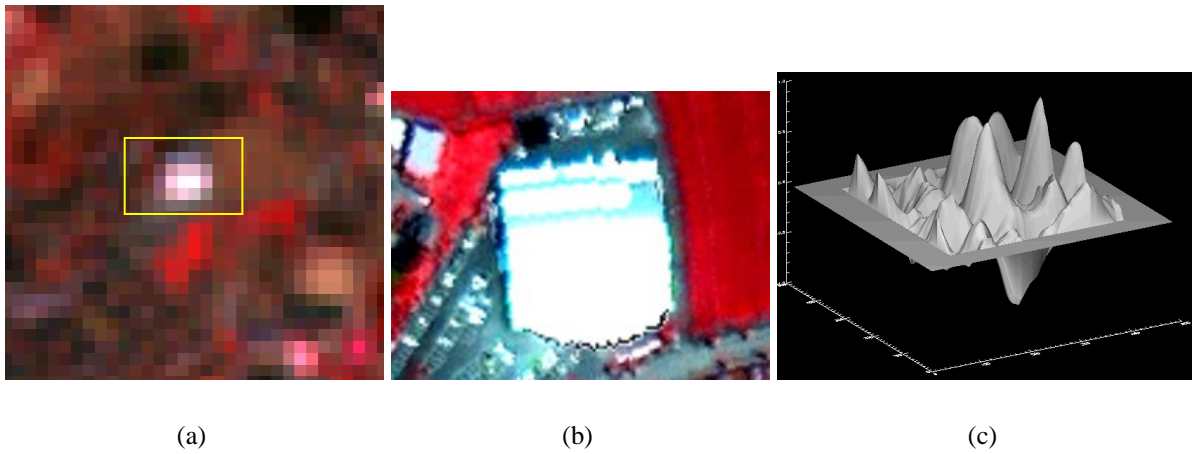


Figure 5.18: GCP 4 for the March scene,(a) searching area on the ASTER acquired in March 2002, (b) a template on the IKONOS, (c) correlation image, correlation: 0.85 (band2), 0.85 (band3)

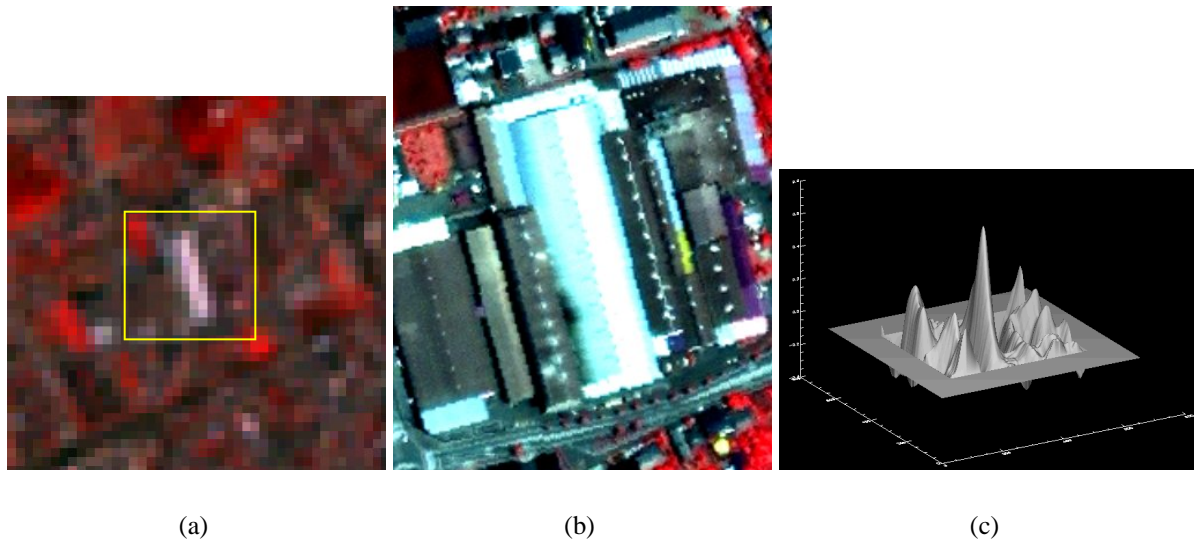


Figure 5.19: GCP 5 for the March scene,(a) searching area on the ASTER acquired in March 2002, (b) a template on the IKONOS, (c) correlation image, correlation: 0.72 (band2), 0.68(band 3)

5.3 The results of the transformations

The maximum correlation of each image matching was significant enough to be recognized as the matching point. Most of correlations showed over 0.7 which results reliable accuracy of transformations (Konencny, 2003). Man-made objects are used for the template matching because they are not much influenced by seasonal change. The image correlations could be changed according to the seasonal landcover change around the man-made objects. The GCPs obtained from image matching were used for the second transformations of the IKONOS image. The direct transformations between the original IKONOS image and each ASTER image geometrically could be obtained using the first and second transformations. Table 5.1 shows the maximum errors of the three geometrical transforms. Table 5.2 shows the root mean square errors (RMSE) of the three transformations. The RMSE of each transformation was less than the ? pixel of the ASTER image (15m) and the result shows that enough accuracy was achieved for the change detection. From Figure 5.20 to 5.22 show the results of the three direct transformations.

Table 5.1: Maximum errors of the three transformations (unit: meter)

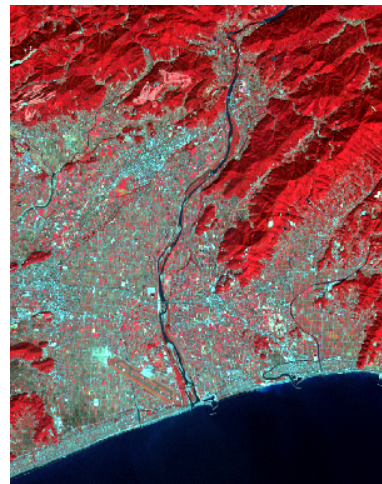
	Max error X	Max error Y
October 2001	1.43	2.07
January 2002	2.34	0.95
March 2002	2.64	0.96

Table 5.2: RMS error of the three transformations (unit: meter)

	RMS error X	RMS error Y
October 2001	0.93	1.42
January 2002	1.56	0.60
March 2002	1.72	0.59



(a)



(b)

Figure 5.20: The result of direct transformation between the IKONOS and the October scene:(a) the IKONOS image, (b) the ASTER image acquired in October 2001.



(a)



(b)

Figure 5.21: The result of direct transformation between the IKONOS and the January scene:(a) the IKONOS image, (b) the ASTER image acquired in October 2001.



(a)



(b)

Figure 5.22: The result of direct transformation between the IKONOS and the March scene:(a) the IKONOS image, (b) the ASTER image acquired in March 2001.

Chapter 6

CHANGE DETECTION AND CLASSIFICATION

6.1 solution proposed for reducing the errors in change detection

As described in the chapter one, a change detection result by pixel by pixel comparison method can contain the errors in change detection due to the pointing direction shift of time series data. In this chapter, a solution for reducing the error was described, and the evaluation of the proposed method was carried out. The land use classification using the result of mixture analyses and change detection of the ASTER images was performed.

6.1.1 Resampling linear mixture analysis results of the ASTER images using geometrically fixed grids

The errors in change detection due to pointing direction shift are generated when incompletely overlaid areas of time series data are compared. If exactly the same area of time series data can be compared, the error in change detection due to pointing direction shift can be reduced.

In this study, a common space which is geometrically fixed grid was proposed to compare the same area of time series data. The linear mixture analysis results of the ASTER scenes were resampled into the fixed grid for each data using the equation 6.1: the grid cell value could be calculated by multiplying the value of each pixel (from pixel 1 to N) included in a fixed grid cell and the existence ratio of each of them (R). Change detections were performed by comparing the fixed grids of the ASTER scenes.

$$fixed\ grid\ value = \sum_{i=1}^n R_j \cdot pixel\ value_j \quad (6.1)$$

where i is pixel order.

For example, the existence ratio of each pixel included in the zoomed grid cell shown in figure 6.1 (E: 23%, F: 67%, H: 2%, I: 8%) can be calculated, then the cell value can be obtained by multiplying each pixel's value and its existence ratio in the cell (Equation 6.2).

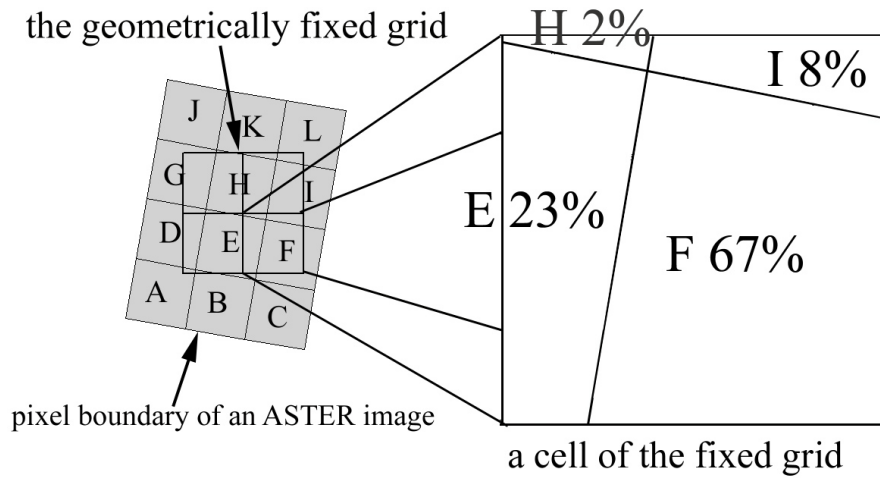


Figure 6.1: A fixed grid overlaid on a classification result of an ASTER scene, existence ratio of each pixel included in the zoomed cell was calculated.

$$\begin{array}{l}
 \text{The value of pixel E} \times \text{The existence ratio of pixel E} \\
 \text{The value of pixel F} \times \text{The existence ratio of pixel F} \\
 \text{The value of pixel I} \times \text{The existence ratio of pixel I} \\
 + \text{The value of pixel H} \times \text{The existence ratio of pixel H} \\
 \hline
 \text{Fixed grid value}
 \end{array} \quad (6.2)$$

6.1.2 Simulation using the classification result of the IKONOS image

It was impossible to examine whether the proposed method is more reliable than the pixel by pixel comparison because exact the ground truths of each time series data were unknown. Therefore a simulation was carried out using a high resolution landcover data which was derived from the IKONOS image.

In this simulation, the change detection of the simulated data carried out by using the proposed method and pixel by the pixel comparison method, then the results of the two change detections were evaluated. Figure 6.2 shows the simulation flow. The simulation was performed on the assumptions that the pointing direction shifted data are acquired in the same period, and changes in the simulation were accepted as change detection errors due to pointing direction shift because the change should not occurred in the change detection of data acquired in the same period.

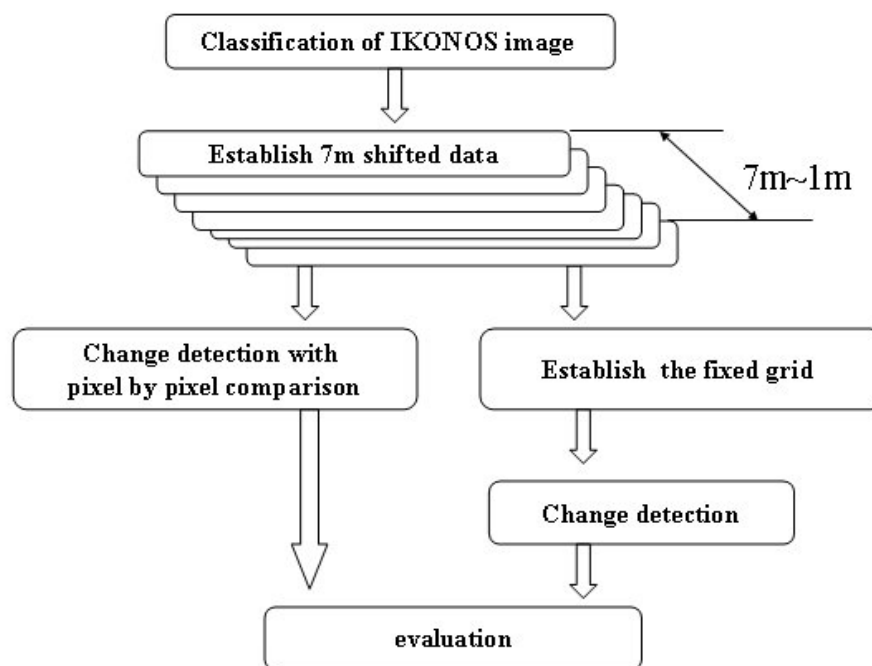


Figure 6.2: The simulation flow

1) Change detection using pixel by pixel comparison method

A test area near riverside where consisted of simple landcover was selected. Firstly, the classification of the test area in the IKONOS image was carried out by visual interpretation (Figure 6.3).

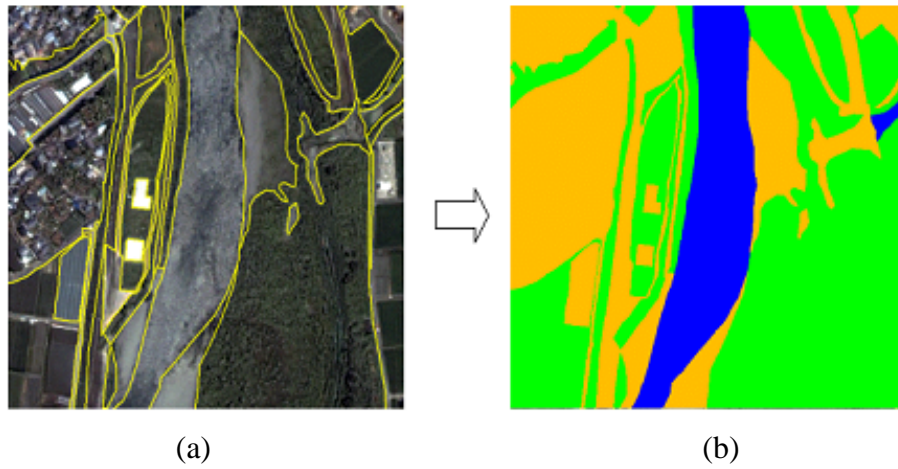


Figure 6.3: Classification of the test area for the simulation by visual interpretation, (a): The test area in the IKONOS image, (b): The classification result (green: vegetation, blue: river, orange: bare soil)

To simulate the pointing direction shifted data, the pixel boundary of an ASTER image was plotted on the classification result using the inverse transformation of the ASTER scene acquired in October. The shift from zero to half of a pixel of the ASTER image (7m) was simulated, thus from zero to seven meters pointing direction shifted data were established (Figure 6.4).

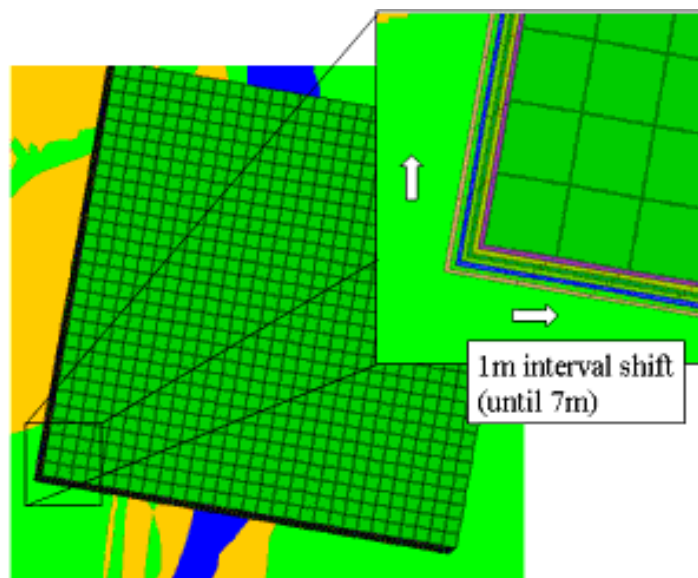


Figure 6.4: Simulated pointing direction shifted data

Land cover attributes were assigned to each cell of the simulated pixel boundary of each pointing direction shifted data. Figure 6.5 shows an example of land cover attribute assignments.

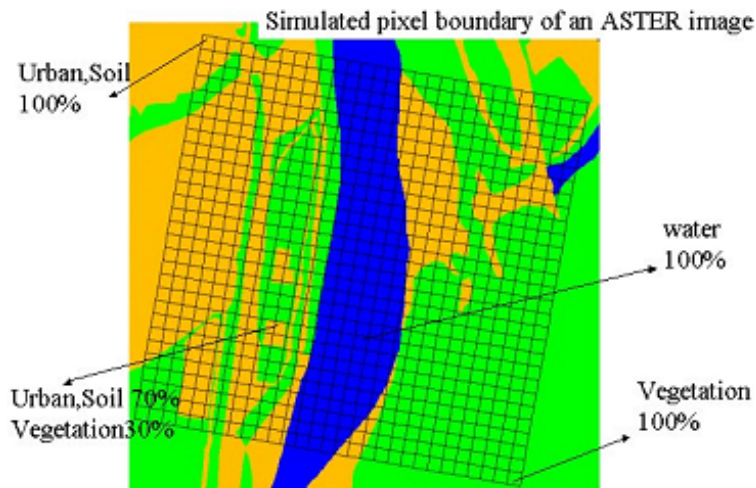


Figure 6.5: Example of Landcover attribute assignments process

The change detections of the simulated data were carried out by using pixel by pixel comparison method. In the change detection, the attribute of zero meter shifted data was compared with one to seven meters shifted data (Figure 6.6).

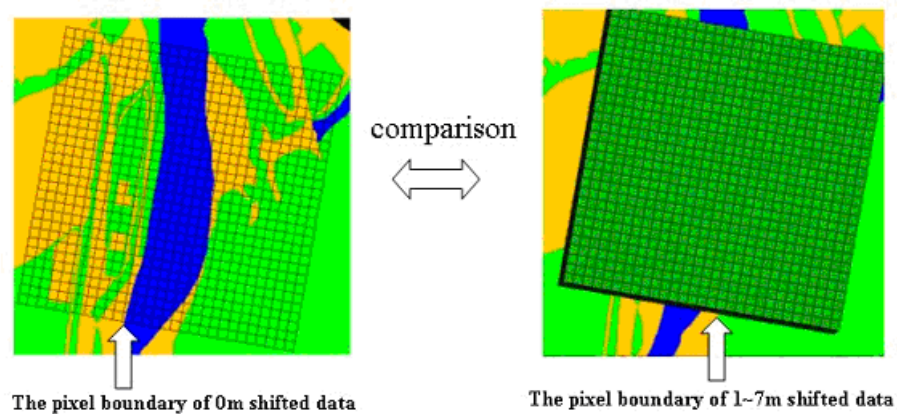


Figure 6.6: Change detection by comparing zero meters shifted data and one meter to seven meters shifted data

2) Change detection using the proposed method

For the change detections using the fixed grids, the fixed grids of zero to seven meters of pointing direction shifted data were generated (Figure 6.7), and the corresponding landcover attributes were assigned to each fixed grid. The change detections were performed by comparing the fixed grid of zero meter pointing direction shifted data with the fixed grids of one to seven meter pointing direction shifted data (Figure 6.8).

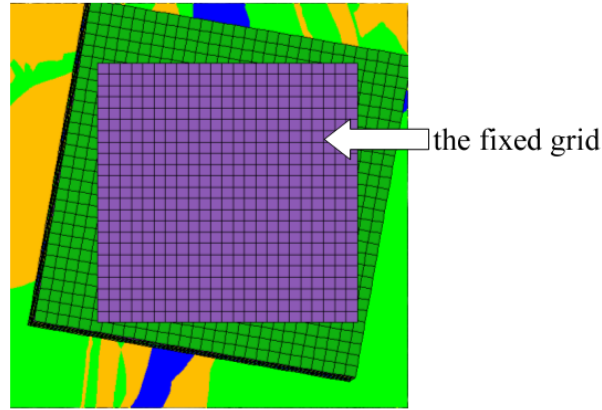


Figure 6.7: Fixed grids for the pointing direction shifted data.

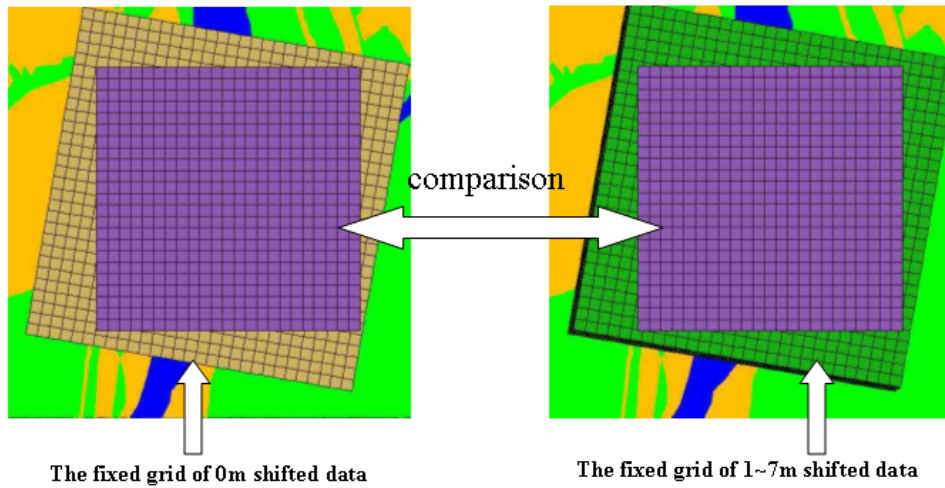


Figure 6.8: Change detection by comparing the fixed grid of zero meter pointing direction shifted data with one meter to seven meters shifted data

Equation 6.3 shows how the average of the change detection error was estimated: the landcover differences between 0m shifted data and a pointing direction shifted data was calculated,

then the sum of the absolute value of their difference was obtained, finally the average of change detection error could be calculated by dividing the sum of landcover differences with the total number of pixel (M).

$$\text{the average of change detection error} = \frac{\sum_{j=1}^m \sum_{i=1}^n |0m \text{ shifted data}_{ij} - Nm \text{ shifted data}_{ij}|}{M} \quad (6.3)$$

where i is pixel order, j, k are landcover types, and M is the total number of pixels

Figure 6.9 shows the result of the change detection. In the result, the average change detection errors by proposed method showed maximum 50% less than the average errors by pixel-by-pixel when the half of an ASTER pixel shifted.

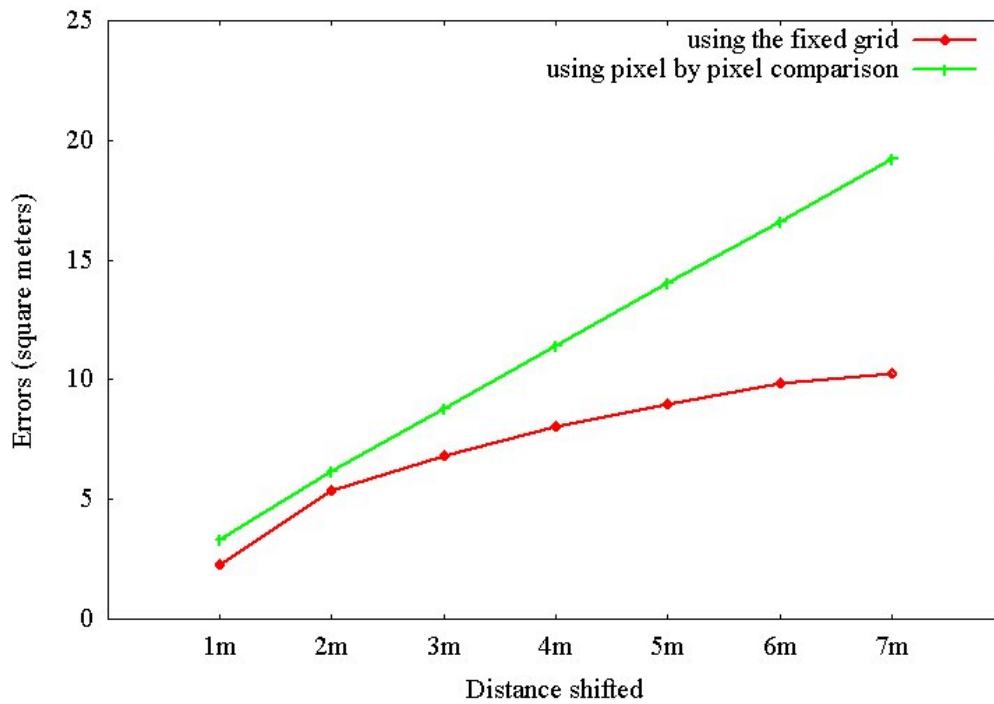


Figure 6.9: Comparison between change detection errors generated by the fixed grid and by the pixel by pixel comparison

6.2 Case study using the ASTER images acquired in October 2001 and January 2002

Change detection between the ASTER scene acquired in October 2001 and January 2002 was carried out using pixel by pixel comparison method and the proposed method. The pointing

direction shift between the two ASTER images is approximately 1m in Easting, 7m in Northing.

6.2.1 Change detection using ASTER images acquired in October 2001 and January 2002 using the two change detection methods

For the change detections, the linear mixture analysis results of the two ASTER images were transformed to the IKONOS coordinate system using the inverse transformation. Figure 6.10 and figure 6.11 show the transformation results of the two classified ASTER images. To keep the original pixel values of the images, the nearest neighborhood resampling method was used in the transformations. Resampling with 15m resolution was carried out for the pixel by pixel comparison method.

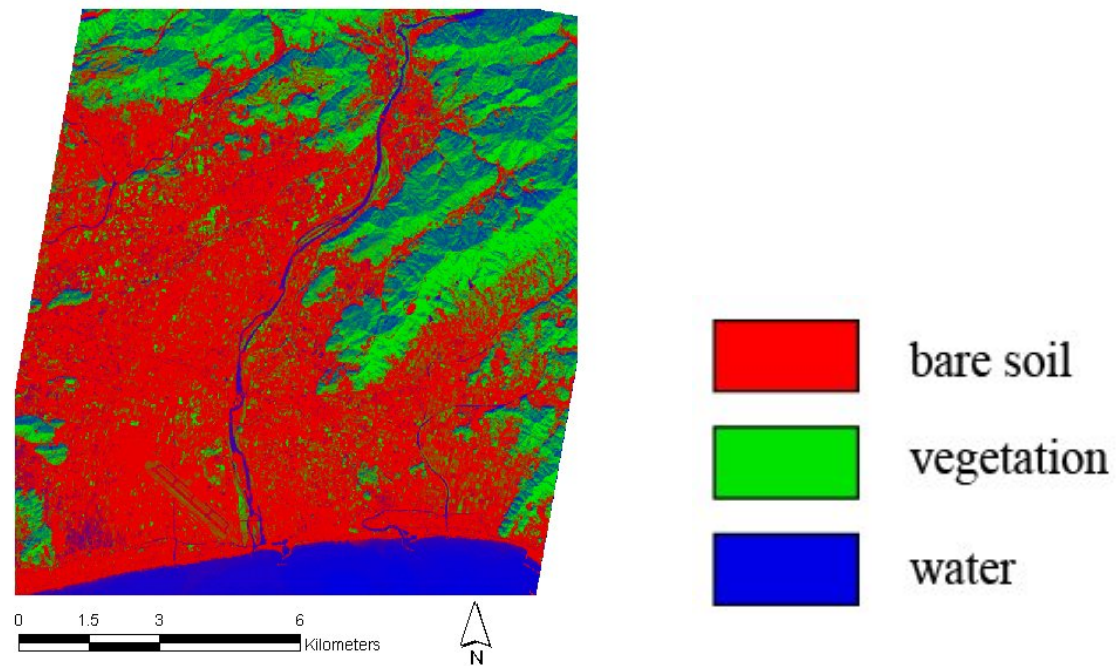


Figure 6.10: Rectified ASTER scene acquired in October 2001.

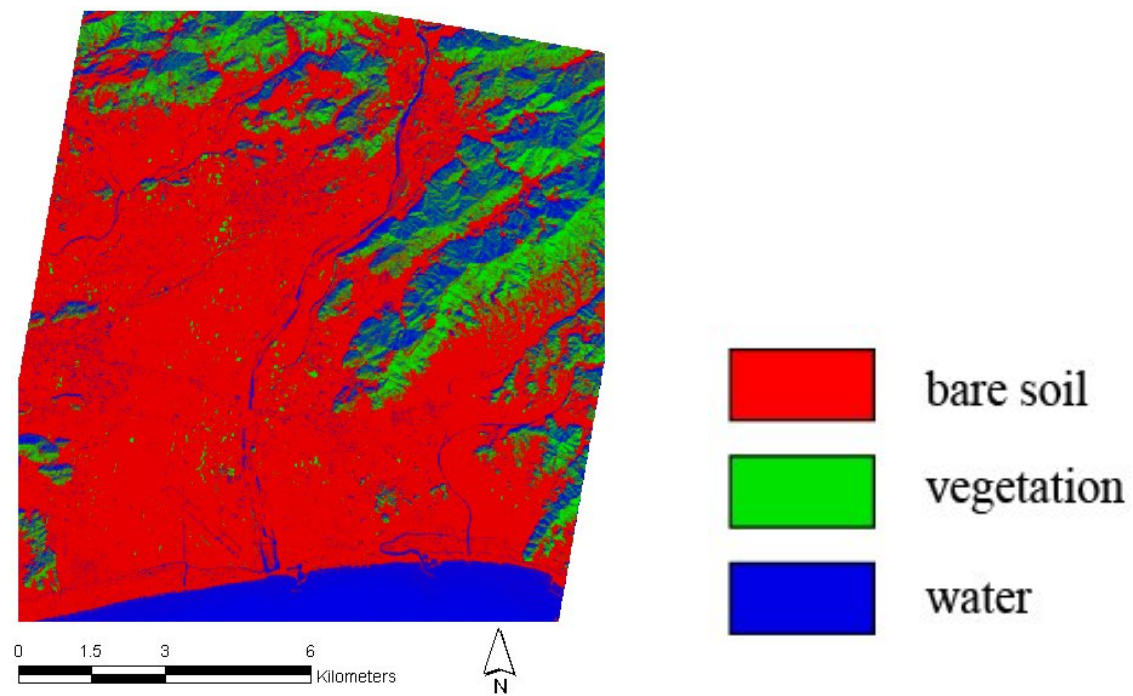


Figure 6.11: Rectified ASTER scene acquired in January 2002.

The change detections using the pixel by pixel comparison method was performed. Figure 6.12 shows the two ASTER images transformed with 15m interval resampling, the insides of the two boundaries were compared.

In the simulation, the pixel boundary of the ASTER image was plotted for the change detection using the proposed method, however it was impossible to plot the pixel boundary of ASTER image on pixel based data, thus detailed resampling with 1m resolution was carried out in the transformation, then the transformed result were resampled into 15m resolution fixed grids, the grids of the ASTER images were compared (figure 6.13).

As a result of change detection, the degree of change was calculated using the equation 6.4. The degree of change shows the quantity of land cover change per a pixel.

the degree of change

$$= \frac{\sum_{j=0}^{row} \sum_{i=0}^{column} \left(\frac{\sum_{k=1}^M |endmember\ k's\ existence\ proportion\ difference|}{number\ of\ endmember} \right)}{total\ number\ of\ pixels} \quad (6.4)$$

where M is number of endmember.

Table 6.1 shows the degree of change by the two change detection methods, the degree of change resulted by the fixed grid was lower than that by pixel by pixel comparison method, this result showed that the pixel by pixel comparison method can contain the change detection errors due to pointing direction shift of the time series data. Figure 6.14 shows the histogram of degrees of change by the two change detection methods, the figure shows that pixel by pixel comparison result more change detection as the degree of change growing.

Table 6.1: The degrees of change by the two change detection methods

	The degree of change per a pixel
Pixel by pixel	24.03
the fixed grid	23.16

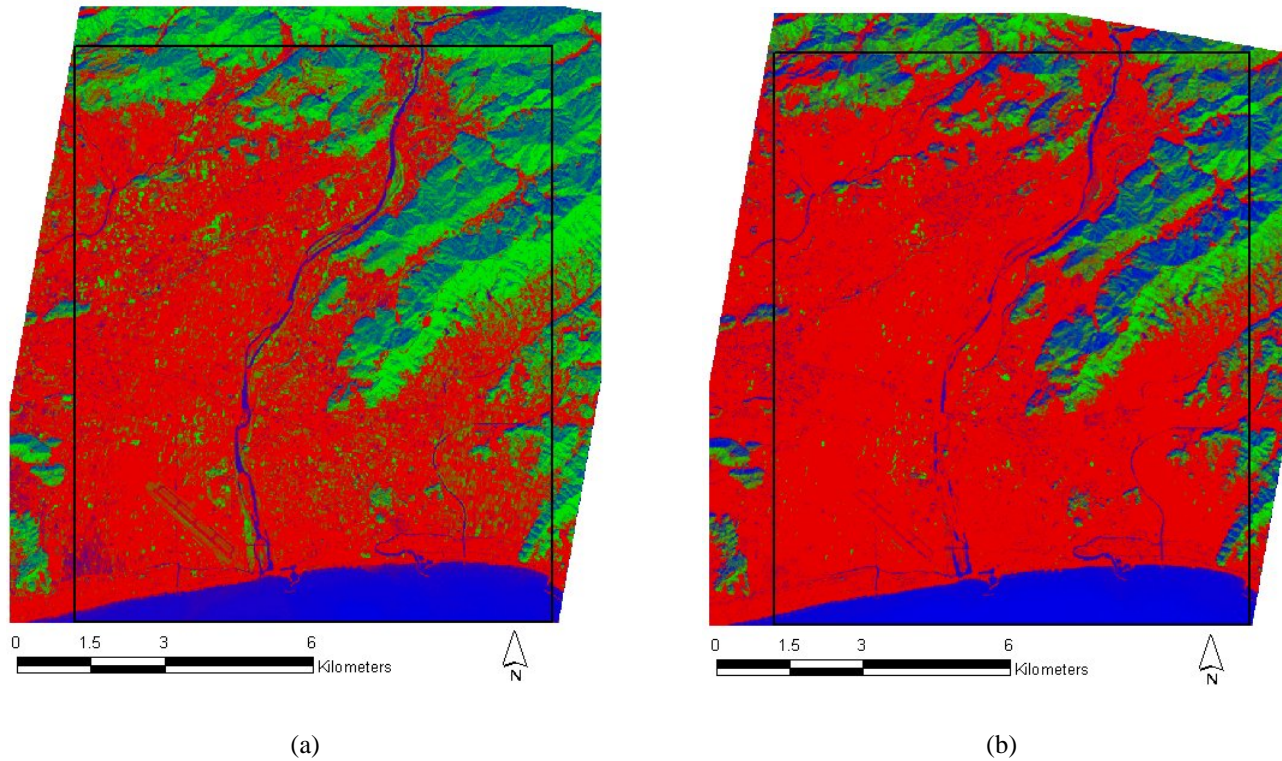
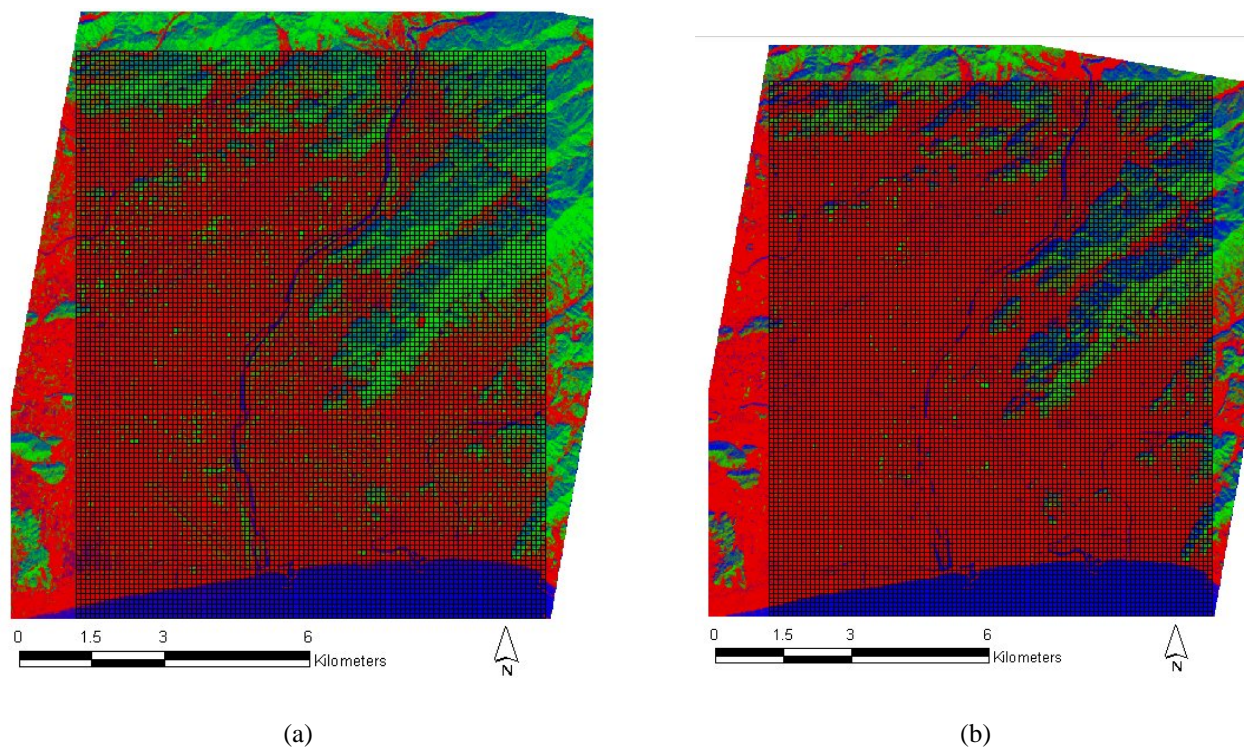


Figure 6.12: Change detection between ASTER scene acquired in October 2001(a) and the rectified ASTER scene acquired in January 2002 (b) using the pixel by pixel comparison: the boxed areas in the two images were compared.



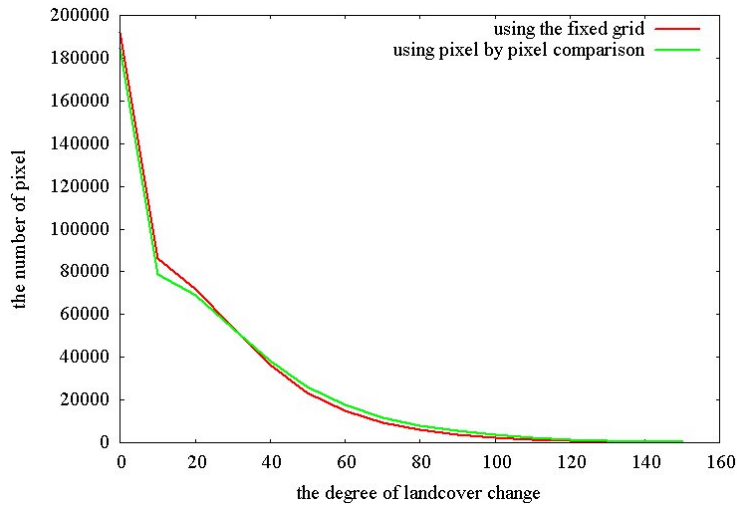


Figure 6.14: The histogram of degrees of change by the two change detection methods

Figure 6.15 shows the change detection results by the two change detection methods and the IKONOS image. The bright area shows landcover change occurred area, while the dark area shows no or less change area. The change detection results by the pixel by pixel comparison methods resulted unstable change detection, and the boundary between asphalt area and grass field shows the evidence that the pixel by pixel comparison is much influenced by the pointing direction shift of time series remotely sensed data. Contrary of the pixel by pixel comparison method, the proposed method resulted more meaningful and reliable change detection. The figure 6.15 shows the significant advantage of the proposed method.

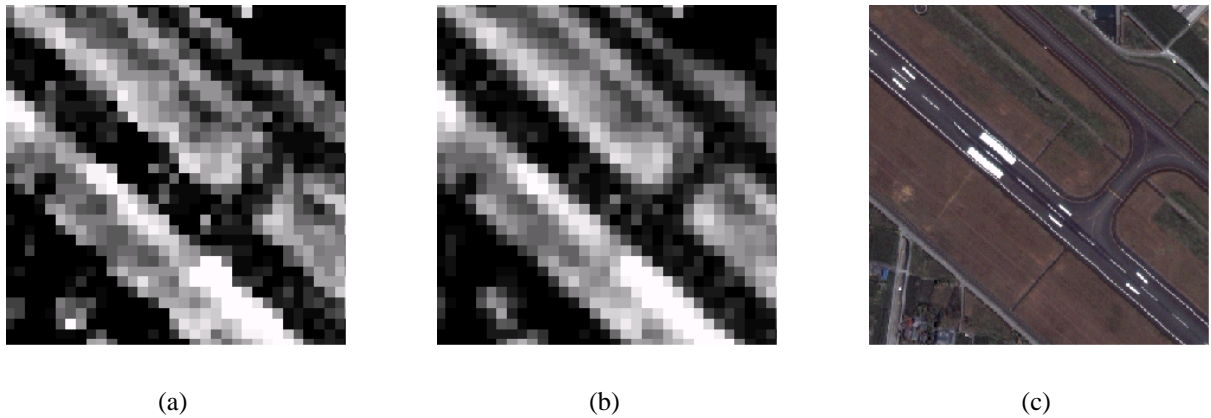


Figure 6.15: (a) the change detection result by pixel by pixel comparison, (b) the change detection result by the proposed method, (c) the IKONOS image.

6.3 Landcover classification using the classification results of time series remotely sensed data

The three ASTER data were normalized, then the linear mixture analyses of the ASTER scenes were carried out, then the linear mixture analysis results of the three ASTER images were transformed into the IKONOS coordinate system using the inverse transformations with 1m interval nearest neighborhood resampling the fixed grids of them were compared each other to perform change detections. The changes of landcovers were quantified by subtracting the classification result of a remotely sensed imagery of one date from that of another date (Equation 6.5). For landcover classification, the results of the linear mixture analyses and change detections of the ASTER images were used.

$$D_{ijk} = CV(season1)_{ijk} - CV(season2)_{ijk} \quad (6.5)$$

where D_{ijk} is the amount of land cover change, CV_{ijk} is the amount of landcover, i is line number, j is column number, k is the type of landcover.

The result of a linear mixture analysis can be detailed with the compositions of endmembers (water, vegetation, bare soil). Seven classes were generated using the three landcover types in the results of linear mixture analyses of the ASTER images. Table 6.2 shows the classes in the first classification. From the figure 6.16 to 6.18 show the classification results using the three linear mixture analysis results.

Table 6.2: The result of linear mixture analysis classified into seven classes

	Water	Vegetation	Soil
Class 1 [water+vegetation+soil]	Exist	Exist	Exist
Class 2 [water+vegetation]	Exist	Exist	None
Class 3 [water+soil]	Exist	None	Exist
Class 4 [vegetation+soil]	None	Exist	Exist
Class 5 [water]	Exist	None	None
Class 6 [vegetation]	None	Exist	None
Class 7 [soil]	None	None	Exist

In the classification results with seven classes; dark urban area (dark man-made objects such like asphalt), water field (including river and sea side), river, and shallow sea were classified into class3. The dark urban area and water field were separated from the river and shallow sea using Euclid distance of them from the waster and soil class. Twenty training data of water and that of soil were used to calculate the average of them. The Euclid distances between class3 and

soil, and class3 and water were calculated using the equation 6.6.

$$d_i = \sqrt{\sum_{l=1}^k (x_{i,l} - \mu_l)^2} \quad (6.6)$$

where d is Euclid distance, x is classification result of each landcover type, μ is the average of training data of each landcover type, l is landcover type, and i is each pixel.

If the Euclid distance of a pixel in class3 was close to soil, the pixel was classified into [dark bare soil + water field] class. If Euclid distance of a pixel was close to water, the pixel was classified into water (river, shallow water) class. From figure 6.19 to 6.21 show the results of the separation of dark urban and water field from water class.

Next, the dark urban was separated from [dark urban + water field] class. A phenological rule was applied to the separation: The changes of water proportion among the three scenes were examined, if the water proportion in [urban + water] class is decreasing from October to March, the class classified into the water field, otherwise the class was classified into dark urban. From figure 6.22 to 6.24 show the result of the separation in the three ASTER scenes. The water field clearly separated from dark urban with the rule. Nine classes were generated; [water+vegetation+soil], soil, vegetation, water, [water+vegetation], water (river, shallow water), [vegetation+soil], dark urban and water field.

The nine classes were classified into bare soil, forest, water, water field including waterside, agricultural field, and dark urban could be classified using 68 phenological rules shown in the table 6.5. In the table 6.3, V_G indicates vegetation group, the vegetation group is consisted of [water+vegetation+soil], [water+vegetation], and [vegetation+soil]. Urban_G indicates urban group which is consisted of soil and dark urban. Figure 6.25 shows the final result of the classification using the 68 phenological rules.

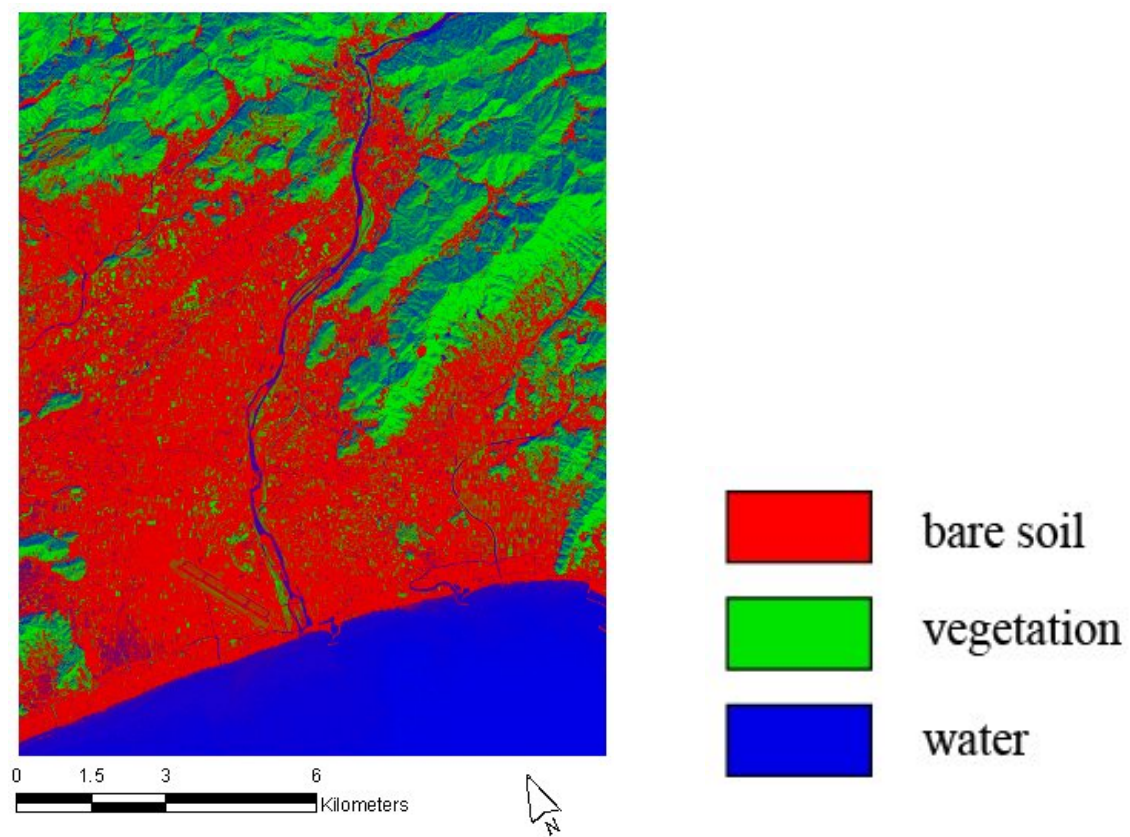


Figure 6.16: Test area of the October scene for the change detection

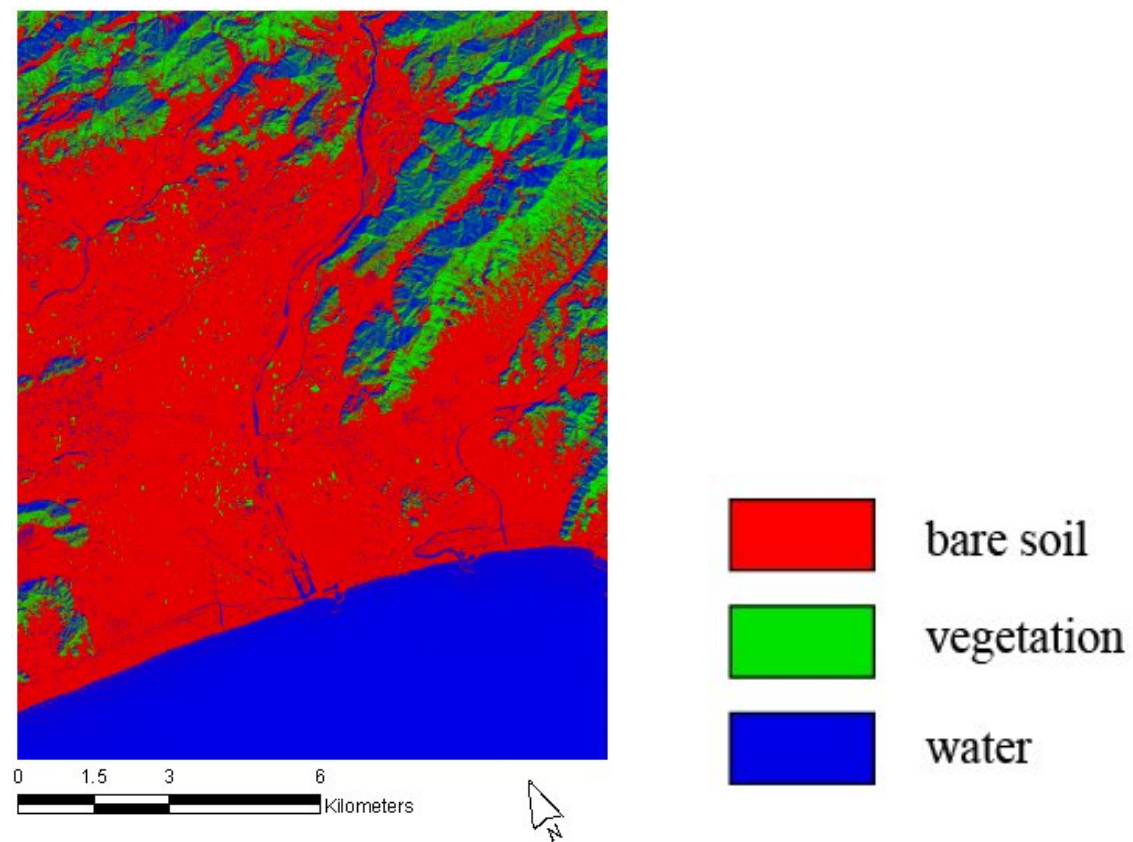


Figure 6.17: Test area of the January scene for the change detection

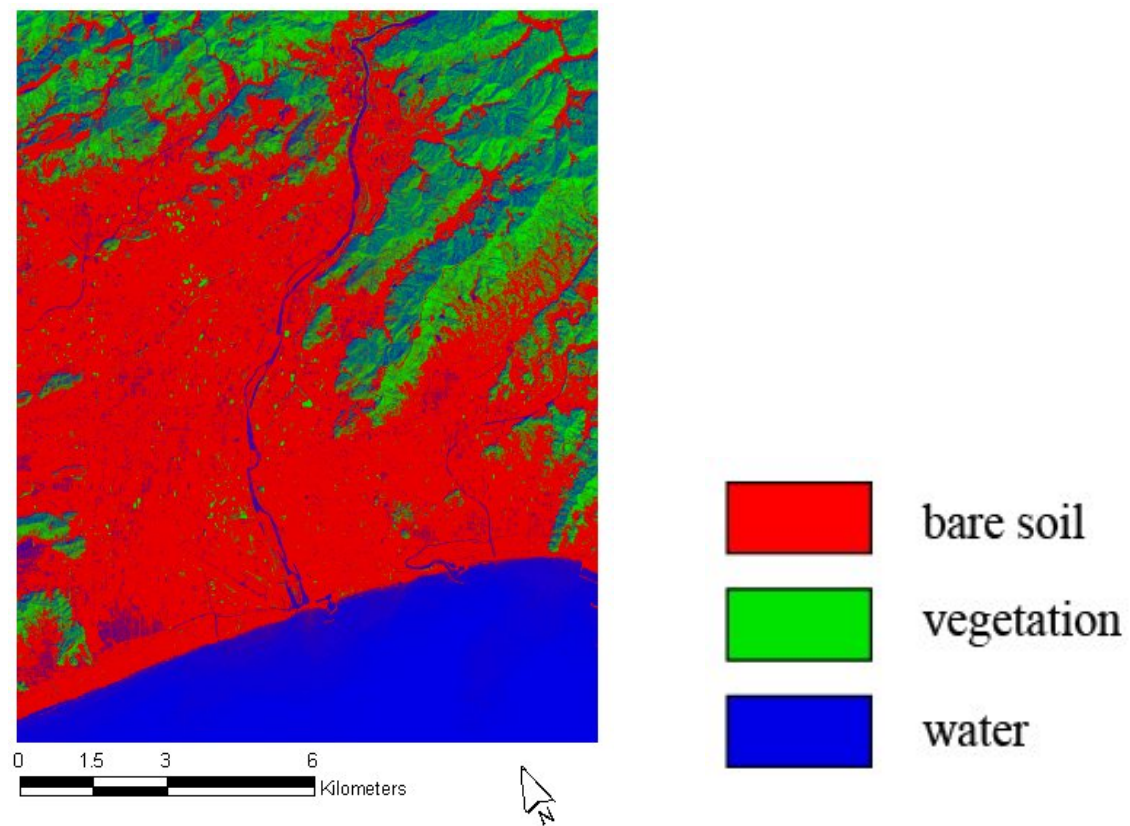


Figure 6.18: Test area of the March scene for the change detection

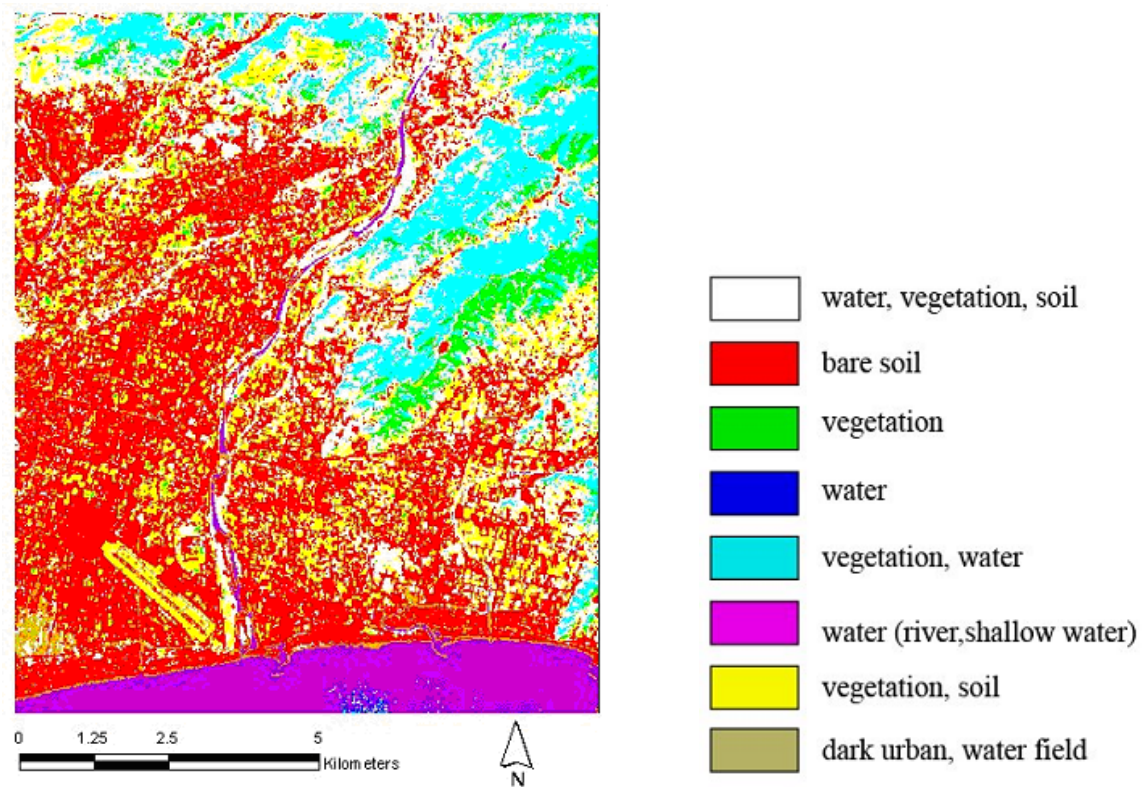


Figure 6.19: Dark urban and water field in the October scene was separated from water class.

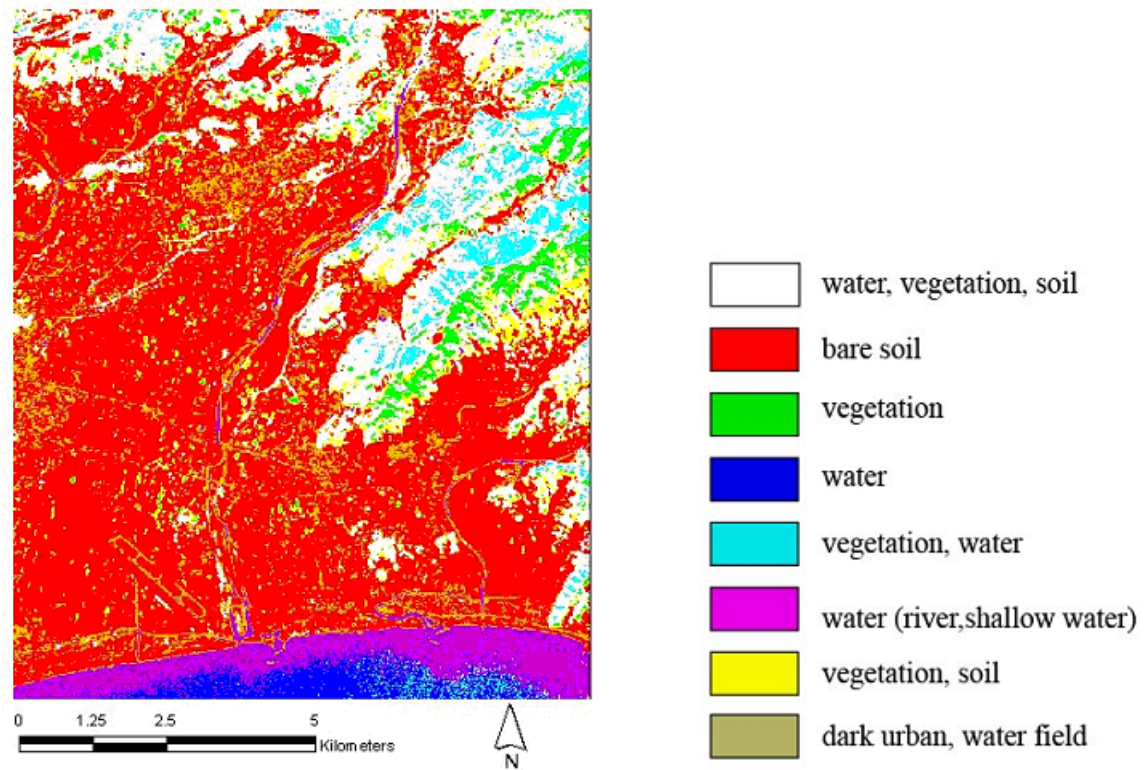


Figure 6.20: Dark urban and water field in the January scene was separated from water class.

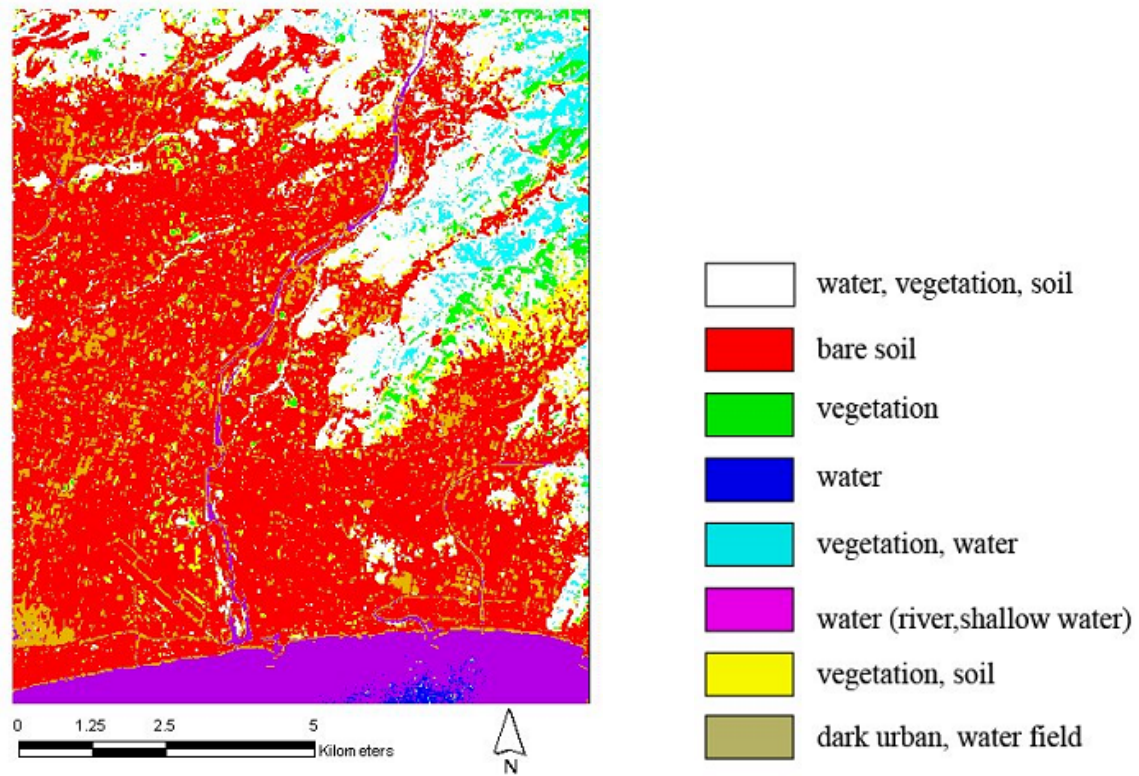


Figure 6.21: Dark urban and water field in the March scene was separated from water class.

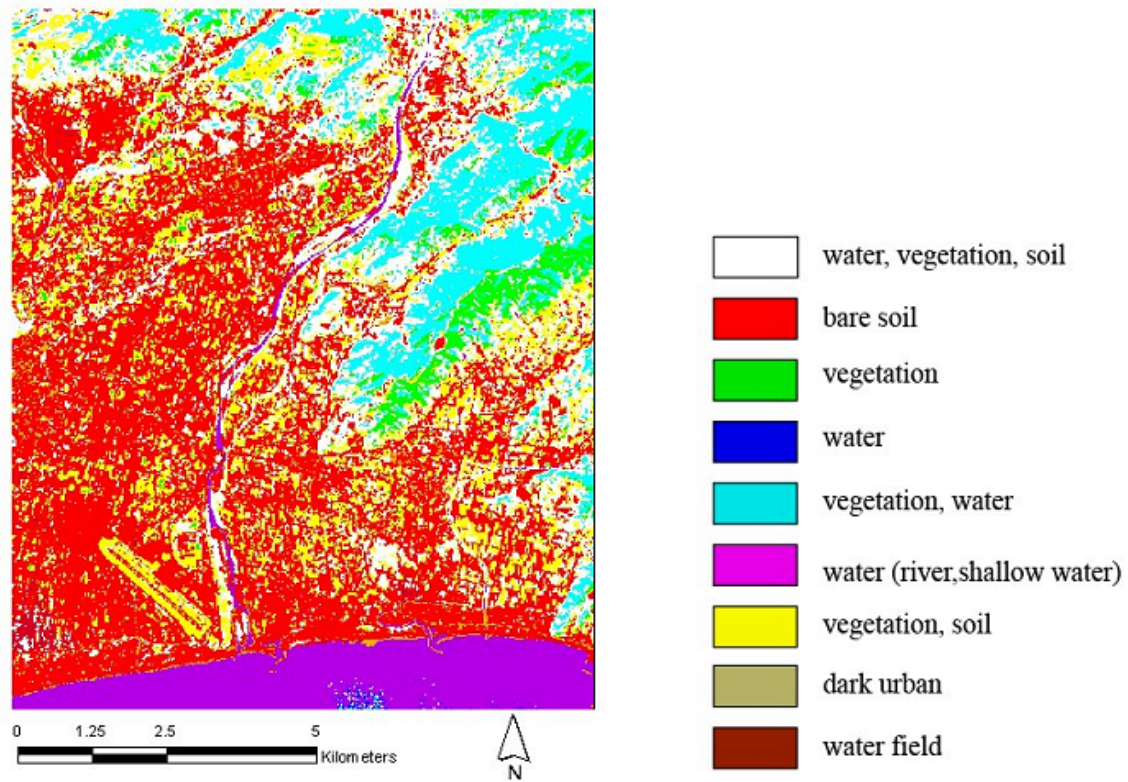


Figure 6.22: Water field in the classification result of the October scene could be separated from dark urban

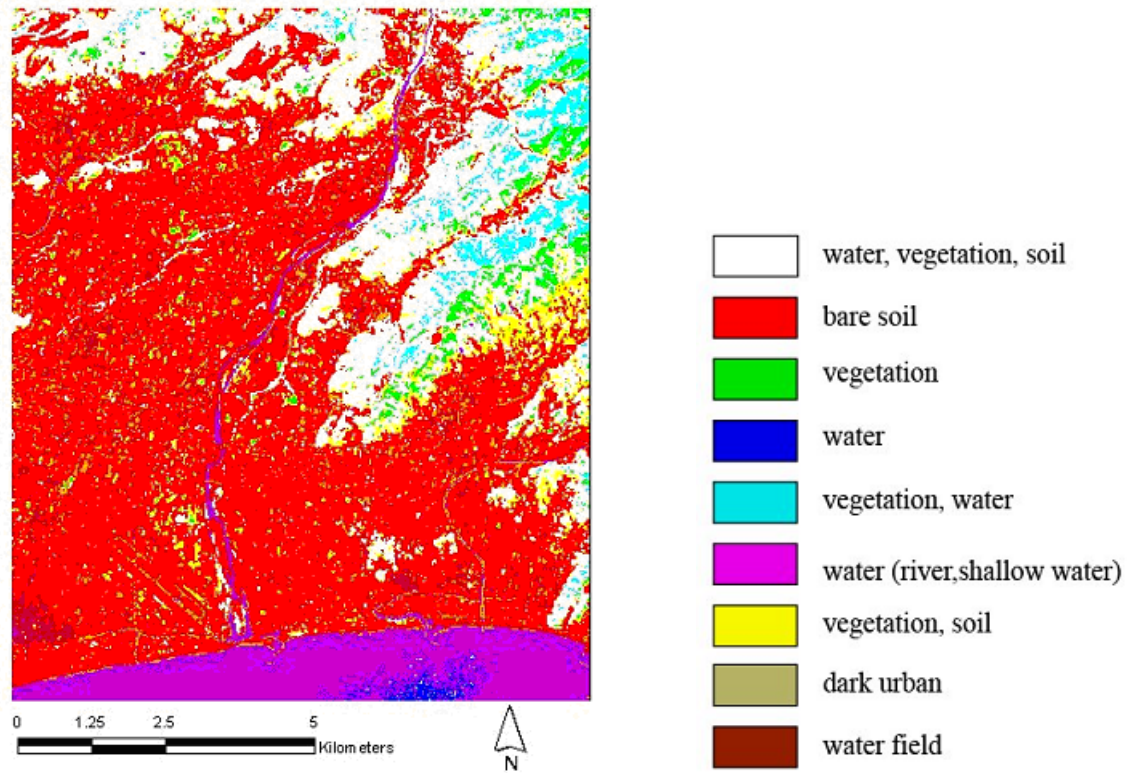


Figure 6.23: Water field in the classification result of the January scene could be separated from dark urban

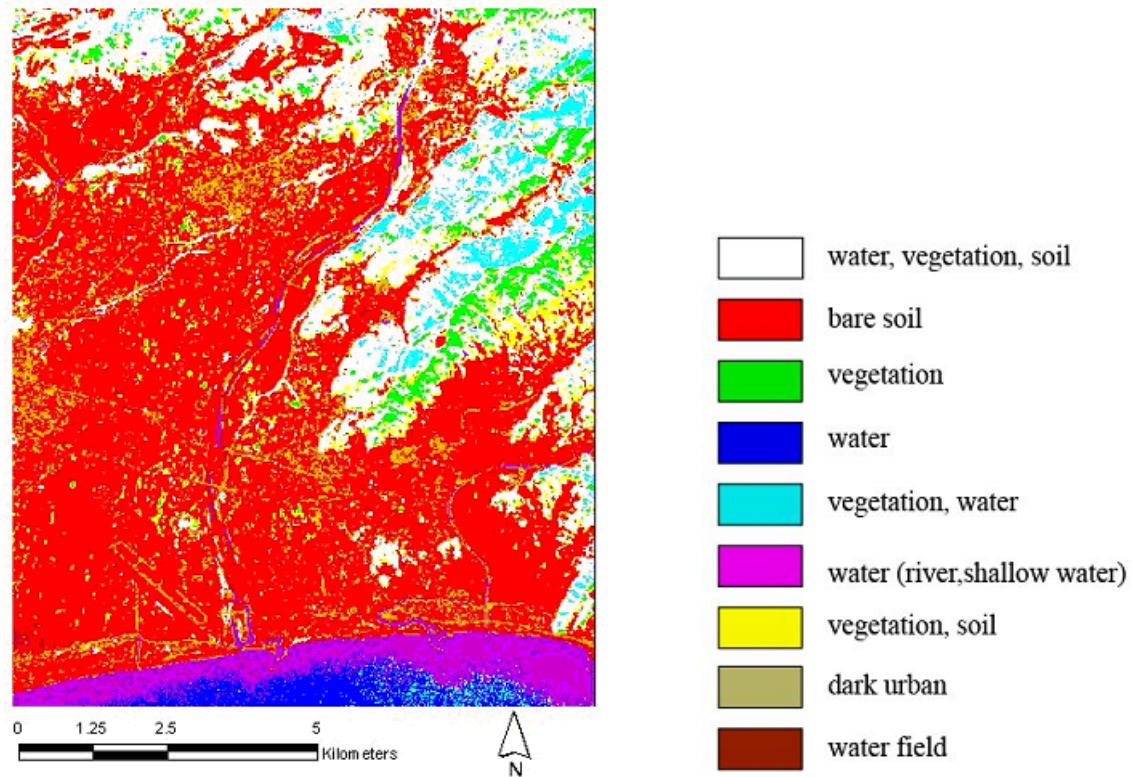


Figure 6.24: Water field in the classification result of the March scene could be separated from dark urban

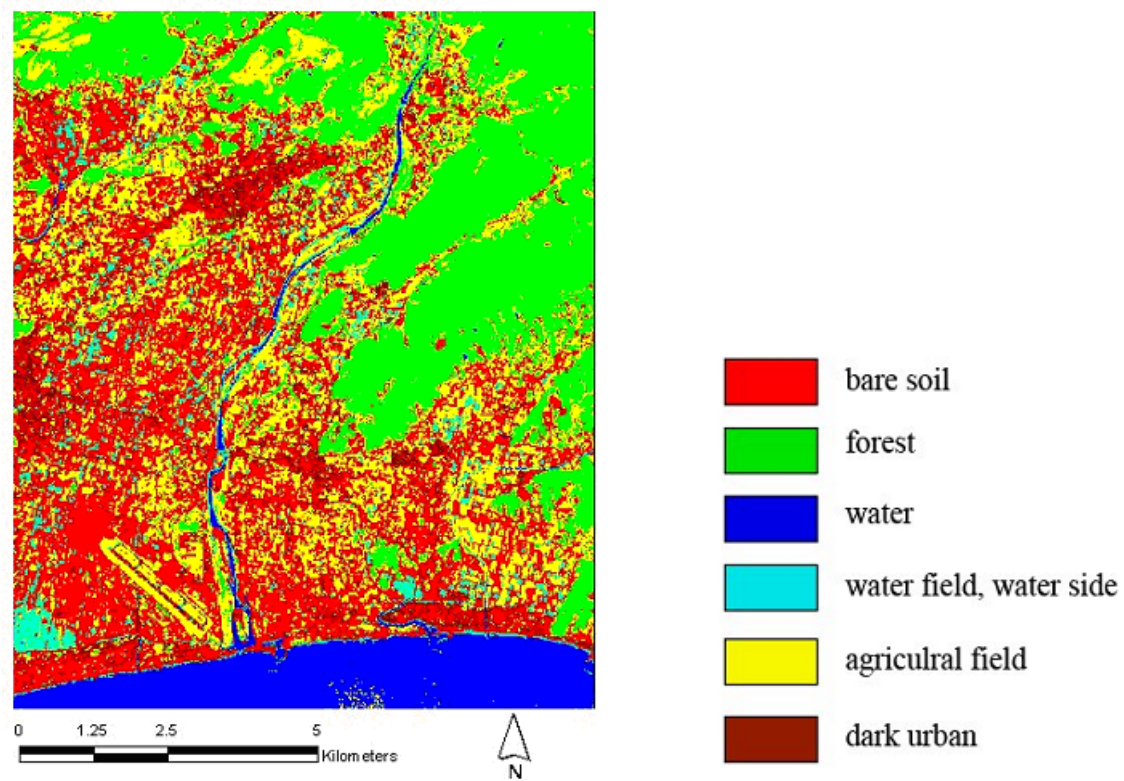


Figure 6.25: The final result of the classification using 68 phenological rules

Table 6.3: 68 phenological rules for the final landcover classification

Rule	1030	103	308	class
1	V_G	V_G	V_G	forest
2	V_G	V_G	water_field	water_field
3	V_G	V_G	urban_G	agricultural_field
4	V_G	V_G	water	water
5	V_G	water_field	V_G	water_field
6	V_G	water_field	water_field	water_field
7	V_G	water_field	urban_G	water_field
8	V_G	water_field	water	water_field
9	V_G	urban_G	V_G	agricultural_field
10	V_G	urban_G	water_field	water_field
11	V_G	urban_G	urban_G	agricultural_field
12	V_G	urban_G	water	water
13	V_G	water	V_G	agricultural_field
14	V_G	water	water_field	agricultural_field
15	V_G	water	urban_G	agricultural_field
16	V_G	water	water	agricultural_field
17	water_field	V_G	V_G	water_field
18	water_field	V_G	water_field	water_field
19	water_field	V_G	urban_G	water_field
20	water_field	V_G	water	water_field
21	water_field	water_field	V_G	water_field
22	water_field	water_field	water_field	water_field
23	water_field	water_field	urban_G	water_field
24	water_field	water_field	water	water_field
25	water_field	urban_G	V_G	water_field
26	water_field	urban_G	water_field	water_field
27	water_field	urban_G	urban_G	water_field
28	water_field	urban_G	water	water_field
29	water_field	water	V_G	water_field
30	water_field	water	water_field	water_field
31	water_field	water	urban_G	water_field
32	water_field	water	water	water_field
33	bare soil	V_G	V_G	agricultural_field
34	bare soil	V_G	water_field	bare soil
35	bare soil	V_G	urban_G	bare soil

36	bare soil	V_G	water	water
37	bare soil	water_field	V_G	water_field
38	bare soil	water_field	water_field	water_field
39	bare soil	water_field	urban_G	water_field
40	bare soil	water_field	water	water_field
41	bare soil	urban_G	V_G	agricultural_field
42	bare soil	urban_G	water_field	water_field
43	bare soil	urban_G	urban_G	bare soil
44	bare soil	urban_G	water	water
45	bare soil	water	V_G	agricultural_field
46	bare soil	water	water_field	water_field
47	bare soil	water	urban_G	bare soil
48	bare soil	water	water	water
49	bare soil	dark_urban	V_G	dark_urban
50	bare soil	dark_urban	water_field	dark_urban
51	bare soil	dark_urban	urban_G	dark_urban
52	bare soil	dark_urban	water	water
53	water	V_G	V_G	agricultural_field
54	water	V_G	water_field	water_field
55	water	V_G	urban_G	bare soil
56	water	V_G	water	water
57	water	water_field	V_G	water_field
58	water	water_field	water_field	water_field
59	water	water_field	urban_G	water
60	water	water_field	water	water
61	water	urban_G	V_G	bare soil
62	water	urban_G	water_field	water
63	water	urban_G	urban_G	water
64	water	urban_G	water	water
65	water	water	V_G	bare soil
66	water	water	water_field	water
67	water	water	urban_G	water
68	water	water	water	water

In the final result of the classification, bare soil class represents bare soil, bright urban area, non agricultural fields and man made objects; forest represents the mountainous area, vegetated hill and forest; water represents rivers and the sea; [water filed, water side] class represents water field, river sides and sea shores; agricultural field represents agricultural fields and grass fields; dark urban class represents dark man -made objects.

The evaluation of the landuse classification could not be carried out due to the lack of time

series data, however although spectral unmixing equations of the October scene used for the linear mixture analyses of the ASTER scenes, abstract landcovers such like water, vegetation and soil could be successfully classified.

Chapter 7

CONCLUSIONS AND DISCUSSIONS

7.1 The errors in change detection due to the pointing direction shift should be considered for the accurate change detection

The accurate transformations were obtained, then pointing direction shift (x:1m, y:7m) between the two ASTER images acquired in October 2001 and January 2002 could be calculated using the transformations. The pointing direction shift were larger than transformations' RMSE (less than 2m), this means that the errors in change detection due to pointing direction shift can influence the result of change detection more than the "misregistration". Gong (1992), Townsahend (1992), and Stow (1999) considered the errors in change detection after registration, while this study considered the errors in change detection before and after registration.

7.2 Resampling method using geometrically fixed grid was developed to reduce the errors in change detection due to the pointing direction shift of remotely sensed time series data.

The comparison between incompletely overlaid areas is a fatal problem in the change detection using pixel by pixel comparison. The proposed method enables the comparison between the same areas of time series data, and can reduces errors generated in pixel based calculation. In the simulation, at most 50% of change detection error due to pointing direction shift could be reduced, and the result of case study showed that the pixel by pixel comparison method have tendency to generate more changes than the proposed method. That how much of the error can be corrected depends on the amount of pointing direction shift. This method can be applied to

other calculations which need pixel based arithmetic calculation.

7.3 The adapted methodology of change detection was established

The proposed method for reducing the change detection error can not be implemented by only itself; the proposed method required the methodology which contains image normalization, linear mixture analysis, image transformation using the very high resolution data. Systematic process for accurate change detection was developed.

Many spatial data and statistical data have been derived from remotely sensed data, however this study showed that one of unknown errors can exist in the processing of remotely sensed data. This study alarms that careful attentions of remote sensing systems and data processing are required. The proposed method will play important role to produce accurate change detection results and to prevent errors from propagating in data processing.

7.4 Future works

The evaluation of the proposed method was carried out in the simulation due to lack of ground truth data. Although the proposed method can reduce the errors due to pointing direction shift theoretically, the other factors such like the accuracy of linear mixture analysis and image normalization can influence the accuracy of the proposed method in actual situations. The ground truth data will be used to evaluate the efficiency of the proposed method. Finally the effect of the proposed method to the total error in change detection will be investigated.

In this study, the pointing direction shift effects to change detection accuracy was investigated in the scope of 15m resolution; more various resolutions need to be investigated because the size of incompletely overlaid areas can be changed according to the resolution. MODIS can be a suitable data for the investigation because this data have multi-resolution (250m, 500m and 1000m) and various spectral bands (36 bands), moreover same date of ASTER and MODIS data are available because the two sensors are on board the TERRA space craft.

The nearest neighbor resampling method is commonly used for change detection because the resampling method does not modify the original DN value of satellite images, thus this study only considered the pixel by pixel comparison of time series data which are resampled by the nearest neighbor method. This study showed that although highly accurate geometrical transformation are carried out, the effect of pointing direction in change detection can not be handled because the limitation of The nearest neighbor resampling method. Bilinear or cubic convolution methods may be more reliable than the nearest neighbor method

method because the method can estimate the same location's DN or land cover value of time series data.

Bibliography

- [1] Civico, D.L.,1989, Topographic normalization of Landsat Thematic Mapper digital imagery, *Photogrammetric Engineering and Remote Sensing*, 55(9):1303-1328.
- [2] Dobson, J. E., R. L. Ferguson, D. W. Field, L. L. Wood, K. D. Haddad, H. Iredale., J. R. Jensen, V. Vklemas, R. J. Orth, and J. P. Thomas, 1995, NOAA Coastal Change Analysis Project (C-CAP): *Guidance for Regional Implementation, National Oceanic and Atmospheric Administration*, NMFS 123, 92p.
- [3] E.A. McGovern, N. M. Holden, S. M. Ward, and J. F. Collins, 2002, The radiometric normalization of multitemporal Thematic Mapper imagery of the midlands of Ireland-a case study, *International Journal of Remote Sensing*, 23, 751-766
- [4] Gong, P., Ledrew, E. F., and Miller, J. R., 1992, Registration-noise reduction in difference image for change detection. *International Journal of Remote Sensing*, 13, 773-779.
- [5] Gruen, A (1985). Adaptive least-squares correlation: powerful image matching technique. *South Africa Journal of Photogrammetry, Remote Sensing and Cartography*, 14(3), 175-187.
- [6] Harry N. Gross and John R. Schott, 1998, Application of spectral mixture analysis and image fusion techniques, *Remote Sensing Environment*, 63, 85-94.
- [7] Helava, U (1978). Digital correlation in photogrammetric instruments. *Photogrammetria*, 34, 19-41.
- [8] JEONG Jong Hyeok and Masataka TAKAGI, An Accuracy Adjustment by Fusion Method with GIS Data and Remote Sensing Data, *Proceedings of the Joint International Symposium on Geospatial Theory, Processing and Applications*, 2002.
- [9] JEONG Jong Hyeok and Masataka TAKAGI, Extraction of Bridge Positions from IKONOS Images for Accuracy Control of Bridge Database, *Proceedings of the 23rd Asian Conference on Remote Sensing, Kathmoandu*, No. 172, 2002.
- [10] JEONG Jong Hyeok and Masataka TAKAGI, A Classification Method Based on Mixed Pixel Analysis For Change Detection, *Proceedings of the 24rd Asian Conference on Remote Sensing*, Pusan, 2003.

- [11] JEONG Jong Hyock and Masataka TAKAGI, Accuracy Evaluation of Change Detection using ASTER and IKONOS Image, 日本写真測量学会平成 16 年度年次学術講演会発表論文集, pp.119-121, 2004.
- [12] Jong Hyeok JEONG and Masataka TAKAGI, Reducing Change Detection Errors due to Different Pointing Direction of Time Series Data, *Proceedings of the 25th Asian Conference on Remote Sensing*, Chiangmai THAILAND, pp.1551-1556, 2004.
- [13] Konecny, G., 2003, *Geoinformation*, Taylor & Francis, New Fetter Lane, London, pp 166.
- [14] Lillesand, T., Kiefer, R., 1994. *Remote Sensing and Image Interpretation*, 3rd Edition. John Wiley and Sons, New York, U.S.A.
- [15] Richards, J., 1993. *Remote Sensing and Digital Image Analysis: An Introduction*, 2nd Edition. Springer-Verlag, New York, U.S.A.
- [16] Settle, J. J. and Drake, N. A. 1993, Linear mixing and the estimation of ground cover proportions, *International Journal of Remote Sensing*, 14, 1159-1177
- [17] Schenk, A. F., 1999. *Digital Photogrammetry*, 1st Edition. Vol. I (in Japanese). Japan Association of Surveyors, Japan
- [18] Stefanie Tompkins, John F. Mustard, Carle M. pieters, 1997 and Donald W. Forsyth, Optimization of Endmembers for Spectral Mixture Analysis, *Remote Sensing Environment*, 59, 472-489.
- [19] Teillet, P.M, 1986, Image correction for radiometric effects in remote sensing, *Canadian Journal of Remote Sensing*, 7(12):1637-1651.
- [20] Townshend, J. R. G., Justice, C. O., Gurency, C. , and Mcmanus, J., 1992, The impact of misregistration on change detection. *IEEE Transactions on Geoscience and Remote Sensing*, 30, 1054-1060.
- [21] Yoshio Edemir Shimabukuro and James A. Smith, 1991, Least-square mixing models to generate fraction images derived from remote sensing multispectral data, *IEEE Transactions on Geoscience and Remote Sensing*, 29, 16-20.
- [22] Xiaojun Yang and C.P. Lo, 2000, Relative radiometric normalization performance for change detection from Multi-date satellite image, *Photogrammetric Engineering and Remote Sensing*, 66(9): 967-980.